Mid-IR frequency comb with sub-Hertz relative line width based on Raman soliton self-frequency shift

Dissertation
zur Erlangung des Doktorgrades
an der Fakultät für Mathematik, Informatik und Naturwissenschaften
Fachbereich Physik
der Universität Hamburg

vorgelegt von

Dominic Laumer

Hamburg

2023

Gutachter/innen der Dissertation:	Prof. Dr. Jochen Küpper Dr. Ingmar Hartl
Zusammensetzung der Prüfungskommission:	Prof. Dr. Jochen Küpper Dr. Ingmar Hartl Prof. Dr. Peter Schmelcher Prof. Dr. Tobias Herr Prof. Dr. Arwen Pearson
Vorsitzende/r der Prüfungskommission:	Prof. Dr. Peter Schmelcher
Datum der Disputation:	15.01.2024
Vorsitzender Fach-Promotionsausschuss:	Prof. Dr. Günther H. W. Sigl
Leiter des Fachbereichs PHYSIK:	Prof. Dr. Wolfgang J. Parak
Dekan der Fakultät MIN:	Prof. Dr.-Ing. Norbert Ritter

Abstract

Optical frequency combs in the mid-infrared spectral region became an invaluable tool for molecular spectroscopy. This spectral region is filled with highly specific vibrational transitions which allow for a precise identification of the composition of gas mixtures and fundamental research of phenomena in physics and chemistry with highest precision. Frequency combs in the mid-infrared are often generated via nonlinear frequency conversion of near-infrared lasers. In this work, two frequency components of the same Yb:fiber comb are converted to the mid-infrared at 4 µm via difference frequency generation (DFG) inside a nonlinear crystal. The long-wavelength component is generated from the shorter wavelength driving laser via Raman soliton self-frequency shift in a highly nonlinear fiber. In the past, not much attention has been paid to the coherence properties and optical line widths of similar DFG frequency combs. To study these properties, the generated mid-infrared light is interfered with a reference frequency comb of known properties. The phase noise of the generated heterodyne beat is characterized to determine the optical line width of the mid-infrared frequency comb. The results show sub-Hz relative line widths relative between the two combs. This method also allows to characterize optical sidebands generated by a dither-and-lock technique, which was used in a previous work for long-term stabilization of the source for minimal intensity noise. In this work, this stabilization mechanism is replaced with an interferometric method which does not require modulation. Paired with the low comb line width this allows for the use of the presented mid-infrared frequency comb for molecular spectroscopy at high resolution with high long-term stability.

Zusammenfassung

Optische Frequenzkämme im Spektralbereich des mittleren Infrarots sind zu einem wichtigen Werkzeug der molekularen Spektroskopie geworden. Jener Spektralbereich ist reich an hochspezifischen Vibrationsübergängen, die sowohl eine genaue Bestimmung der Zusammensetzung von Gasgemischen als auch die Erforschung von grundlegenden Phänomenen der Physik und Chemie mit höchster Präzision erlauben. Frequenzkämme im mittleren Infrarot werden für gewöhnlich durch nichtlineare Frequenzkonversionsprozesse von Lasern im nahen Infrarot erzeugt. Für diese Arbeit werden zwei Frequenzkomponenten des selben Yb:Faser-Frequenzkammes in einem nichtlinearen Kristall mittels Differenzfrequenzmischung (DFG) in den mittleren Infrarot bei 4 µm konvertiert. Dabei entsteht die langwellige Komponente mittels Raman-Soliton-Selbstfrequenzverschiebung in einer hochnichtlinearen Faser aus dem kurzwelligerem Licht des treibenden Lasersystems. Für ähnliche DFG-Frequenzkämme ist in der Vergangenheit wenig Augenmerk auf deren Kohärenzeigenschaften und optischen Linienbreiten gelegt worden. Um diese zu vermessen, wird das erzeugte Mitt-Infrarot-Licht mit einem Referenzfrequenzkamm mit bekannten Eigenschaften interferiert. Das Phasenrauschen der erzeugten heterodynen Schwebungsnoten wird charakterisiert, um die optische Linienbreite des Mitt-Infrarot-Kamms zu bestimmen. Die Ergebnisse zeigen Sub-Hz relative Linienbreiten zwischen den beiden Kämmen. Diese Methode erlaubt ebenfalls die Charakterisierung optischer Seitenbänder, die von einer Dither-and-Lock-Technik erzeugt wurden, die in einer Vorarbeit zur Langzeitstabilisierung der Quelle für minimales Intensitätsrauschen genutzt wurde. In dieser Arbeit wird jene Stabilisierungsmethode durch eine neue interferometrische Methode ersetzt, die ohne Modulation auskommt. Dies gepaart mit der geringen Kamm-Linienbreite erlaubt den Einsatz des präsentierten Mitt-Infrarot-Frequenzkamms für molekulare Spektroskopie mit hoher Auflösung und hoher Langzeitstabilität.

Contents

1 Introduction

The discovery of the optical frequency comb based on broadband mode-locked laser systems with high repetition rates of 10s of MHz to several GHz back in the 1990s paved the way to quickly measuring absolute optical frequencies by providing a direct link between the radio frequency (RF) frequency spectrum and the optical spectrum at multiple 10s to 100s of THz [1, 2]. The gap between these two spectral ranges can span many orders of magnitude. Before frequency combs, this led to the implementation of highly complicated harmonic frequency chains linking many different RF frequency standards and countinuous wave (CW) lasers, only to be able to measure the absolute frequency on a single optical transition at a time [3, 4]. A frequency comb on the other hand can be thought of as a multitude of many such phase-stable linked narrow-line CW lasers, or the frequency comb's *teeth*, with a well-defined spacing (the frequency comb's repetition rate, f_{Rep}) and offset (the carrier-envelope phase offset (CEO) frequency, f_{CEO}), only requiring a stabilization of these two parameters. Here, the repetition rate can be stabilized either directly or via a heterodyne beat f_{Beat} with a CW laser of known frequency and low optical line width, leading to the transfer of this line width to the optical frequency comb [5]. Using mode-locked lasers stabilized this way thus allows for spectroscopy on many different atomic or molecular transitions at the same time, obsoleting the need for complicated harmonic chains only a few years after their full implementation. In these experiments, the achievable resolution of the setup is only limited by the optical line width of the comb teeth, which is affected by the quality of the $f_{\mathrm{Beat,CEO}}$ stabilization mechanism and the lasers oscillator itself.

Both frequency and its inverse, the time, are the physical quantities measurable with the highest precision. Therefore, it is useful to transfer other quantities into these for their measurement [1]. By doing so, many different properties of the world around us become measurable with high precision when employing optical frequency combs [4, 6]. Relating length measurements with the speed of light for example allows for the implementation of highly precise light detection and ranging (LIDAR) devices using frequency combs [7, 8]. Other applications include the long-term measurement of fundamental natural constants to put limits on possible drifts of fundamental physical laws over time [9–11].

Optical frequency combs have been demonstrated for a wide range of the electromagnetic spectrum [4, 6]. One important spectral region is the mid-infrared (Mid-IR) between about 2 to 20 µm, where frequency combs can provide coherent light with significantly narrower optical line widths and higher brightness than classical thermal light sources. This region is full of characteristic vibrational transition of many different molecules, allowing researchers to quantify different molecular species in a mixture with ease for

different purposes in fundamental sciences, industry and health [12–17]. However, at these wavelengths, the development of suitable laser gain materials and saturable absorbers for the generation of mode-locked lasers is significantly behind the state of more common Near-infrared (Near-IR) laser systems between 0.8 to 2 µm [18]. While for example fully referenced Cr:ZnSe frequency combs with central wavelengths between 2.2 to 2.6 µm have been developed [19–22] and commercialized (IPG Photonics CLPF series), the very similar Fe:ZnSe crystal system lasing at 4.4 µm has so far been shown only by one group to be passively mode-lockable at all [23, 24].

To overcome this issue, nonlinear frequency conversion of widely available Near-IR frequency comb down into the Mid-IR is often used. The driving laser for these Mid-IR frequency combs are typically based on materials like Ti:sapphire, Yb:fiber, Er:fiber or Tm:fiber. Starting from these sources, nonlinear conversion is performed mainly with two different methods, optical parametric oscillation (OPO) (with microresonator combs as a special case) or difference frequency generation (DFG), each with their own unique set of features and challenges [2, 12]. OPOs consist of optical resonators similar to those found in lasers, with the gain medium replaced by a material exhibiting high nonlinear susceptibilities. This crystal is then pumped by the aforementioned Near-IR frequency comb laser to generate intermediate frequency *signal* and low frequency *idler* photons in the Mid-IR. Using such a resonator allows simultaneous parametric gain for multiple longitudinal modes of the resonator, allowing broadband pulses to be generated and circulate within the OPO. Relative to the driving comb this method allows for the generation of sub-Hz line widths in the Mid-IR region, meaning that the OPO itself does not introduce significant broadening of the comb lines after frequency conversion [25–30]. However, this method also requires careful dispersion management such that the generated pulses' shape stays stable for each roundtrip. In addition to this, the cavity length requires active synchronization to the OPO cavity length for the pulses to add up coherently with each input pump pulse, together with an excellent f_{CEO} control for the generated Mid-IR comb to provide these low line widths.

DFG setups on the other hand function by mixing two spectral regions of a single frequency comb in a nonlinear crystal. This approach does not require active synchronization of two cavities and generates a CEO-free comb [31]. The intricacies of this approach instead are shifted to generating the two frequency components allowing the DFG process at the target Mid-IR wavelengths and to establishing their temporal overlap inside the crystal. In one approach, the higher frequency *pump* photon for the process is generated via blue-shifting parts of the driving *seed* laser, which has been proven to generate combs with sub-Hz line widths relative to the driving laser, similar to OPOs [32–34]. However, the generated pump beam requires subsequent amplification to be able to drive the DFG process, complicating the setup.

By contrast, the lower frequency seed beam can be generated from the driving laser acting as the pump without requiring further amplification. To do so, Raman soliton self-frequency shift (SSFS) and spectral broadening in all-normal dispersion fibers are commonly used coherent processes [35, 36]. However, not much attention has been paid to optimizing the optical line width of this type of Mid-IR frequency combs, with this property either not being measured at all [37–41], resulting in measured optical line widths between 20 to 400 kHz or achieving no coherent signal at all [42–45].

In previous works by our group such a DFG setup has been implemented using Raman SSFS for seed pulse generation based on an Yb:fiber frequency comb [46, 47]. In this work, it was also discovered that this source exhibits a sudden drop in relative intensity noise (RIN) within a small region of the pump/seed delay close to maximal temporal overlap. Following this discovery a dither lock mechanism was implemented to suppress the RIN for long-term stable operation of the Mid-IR source. It was then used for absorption spectroscopy of both CO and NH_3 molecules at room-temperature and decreasing pressures [14, 47, 48]. However, data analysis showed an unexpected line broadening in the measured spectra [47].

During the course of this thesis, it was discovered that this line broadening ist most likely caused by the dither lock mechanism, which leads to modulation sidebands of the comb lines. In this work, this mechanism was replaced by a modulation-free method based on interferometry. With this method, we achieved the same long-term stable intensity noise suppression as the dither lock. The used setup and the results for this work are presented in Chapter 3, confirming that the new mechanism can fulfill all requirements for precision spectroscopy. As the next step,the optical line width of the Mid-IR frequency comb was measured by performing a heterodyne beat with a second infrared frequency comb of known low line width synchronized with the Mid-IR comb. The resulting measurements showing that the Mid-IR comb exhibits a sub-Hz line width relative to the reference comb are detailed in Chapter 4. These results confirm these low line widths for the first time for this type of Mid-IR frequency comb to the knowledge of the author. Additionally, the measurements confirm the sideband generation of the dither lock method with good conformance to a numerical model. The last Chapter 5 summarizes the entire thesis and gives an outlook into some planned spectroscopic experiments to apply the Mid-IR frequency comb.

In the next chapter, an introduction into the fundamental physics behind the frequency comb setup and the measurements presented in this work is given before going into details on the experiments in the following chapters.

2 Fundamentals of the Mid-IR frequency comb

The presented Mid-IR frequency comb in this thesis requires many different physical effects and mechanisms to function. Therefore, the aim of this chapter will be to explain those fundamentals in a way that allows the reader of this work to follow the experimental descriptions given in Chapters 3 and 4. To start, a short description of mode-locked lasers is given followed by explanations of different physical effects and electronic mechanisms. These are required for the stabilization of these lasers to work as frequency combs and their conversion into the Mid-IR spectral region. The chapter then goes into detail on the influence of both intensity and phase noise on the output of the frequency comb, especially with respect to its optical line width. This is followed by a numerical investigation of a modulation of the relative delay between two frequency components required for the Mid-IR conversion, showing the effect of this modulation on the comb structure. The chapter then ends with details on the spectral measurements on the Mid-IR frequency comb using a Fourier transform infrared (FTIR) spectrometer.

In this chapter, most information is gathered from different text books with overlapping contents, mostly from references [5, 49, 50]. Of these, reference [49] provides the reader with the most recent and comprehensive summary of the field of mode-locked laser and frequency comb technology, including an extensive discussion of the various noise properties of these devices. Additional sources to these references are noted when required.

2.1 Mode-locked lasers

A passively mode-locked laser resonator (or *oscillator*) as used in this work consists of four main components, namely a gain medium together with its pump, a saturable absorber and the optical resonator surrounding these parts. These components are shown in Figure 2.1. Here, an optical pump laser is used to pump the active gain medium inside the laser resonator to enable the lasing process, with a linear resonator being shown here. This resonator consists of one highly-reflective mirror and one partially reflective mirror for out-coupling of the laser light. The resonator is configured such that multiple longitudinal modes ν_n (with n as the modal index) are allowed to circulate at roundtrip times corresponding to their phase velocity v_p in the oscillator. Additionally, the gain medium exhibits a broad emission or gain gain bandwidth. To mode-lock the laser, an additional device called *saturable absorber* is integrated into the resonator. Its loss decreases for

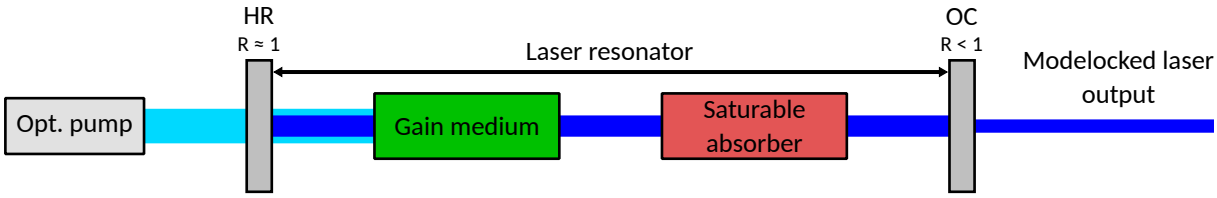

Figure 2.1: Sketch of a passively mode-locked laser. In addition to the usual gain medium the laser resonator contains a saturable absorber with decreased loss at higher intensities. This makes the laser favor a pulsed operation with a repetition rate corresponding to the pulses roundtrip time.

higher light intensities at the absorber, leading to the longitudinal modes starting to oscillate in locked relative phases. By constructively interfering these modes are then generating a higher-intensity pulse circulating in the resonator. Every roundtrip, a part of this pulse is coupled out of the resonator at the lasers repetition rate $f_{\mathrm{Rep}} = v_g/L$, with v_g being the group velocity of the pulse envelope travelling inside the resonator and L its optical roundtrip length. For the linear resonator depicted in Figure 2.1, the latter becomes twice the optical length of the resonator. This *mode-locking* leads to broadband pulses with an envelope defined by the oscillators gain and saturable absorption characteristics centered around a carrier frequency ν_c being emitted from the oscillator.

Using this mechanism, these pulses are emitted with equal energy and envelope in absence of fluctuations. However, due to dispersion, the pulses group velocity v_g is not necessarily equal to the phase velocity v_p at the carrier frequency ν_c. For this reason, the carriers oscillation does not usually reach its maximum electrical field at the same time the pulse envelope becomes maximal. Instead, a relative phase between this carrier oscillation and the pulse envelope ϕ is observed, called the carrier-envelope phase (CEP). Caused by the oscillators difference in v_g and v_p, this CEP changes between pulses by an ideally constant amount $\Delta\phi$ called the carrier-envelope phase offset (CEO). The effect of this CEO slip is shown in Figure 2.2. In this plot, the electric field of two pulse trains with different CEO $\Delta\phi$ (blue: $\Delta\phi = 0$, red: $\Delta\phi = \pi/2$) from otherwise equal oscillators are shown. For the first pulse at $t = 0$, the electric field of both pulses is equal, while after two pulses the field of the train with $\Delta\phi = \pi/2$ flipped signs with respect to the CEO-free train.

2.2 Optical frequency combs

Following this time domain picture of the pulse train from mode-locked oscillators, this section takes a look a the frequency domain picture of the mode-locked laser's pulse train. A sketch of this is shown in Figure 2.3. The spectrum of a pulse train of equally spaced pulses in time domain consists of narrow spectral comb lines spaced apart by the pulses repetition rate f_{Rep}. These comb lines arise due to the constructive interference from the

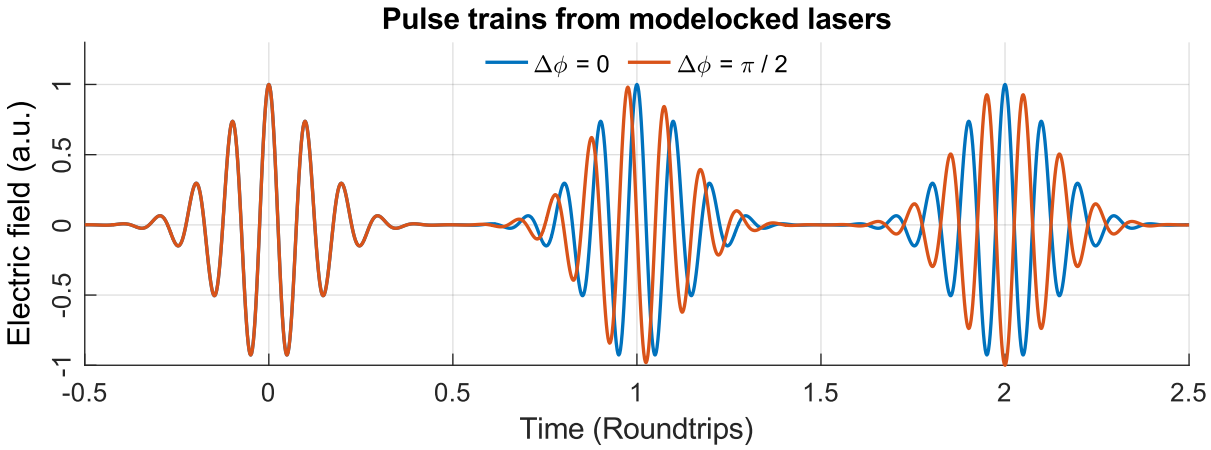

Figure 2.2: Pulse trains from ideal mode-locked lasers in the time domain. In the blue pulse train the carrier envelope phase is zero for all pulses. In the red train, the CEP shifts by a constant offset of $\Delta\phi = \pi/2$ between adjacent pulses, flipping the fields sign every second pulse.

laser pulses only at these well-defined frequencies. Their amplitudes follow an envelope defined by the optical spectrum of a single pulse. The absolute position of this comb-like structure (hence *optical frequency comb*) is offset from zero frequency by the CEO frequency

$$f_{\mathrm{CEO}} = f_{\mathrm{Rep}} \times \frac{\Delta\phi}{2\pi}, \tag{2.1}$$

and both frequencies together with a mode index n form the comb equation

$$\nu_n = f_{\mathrm{CEO}} + n \times f_{\mathrm{Rep}}, \tag{2.2}$$

defining the optical frequency of a comb mode ν_n as a function of two RF frequencies f_{CEO} and f_{Rep}. This results in the optical frequency comb providing a coherent link between the RF and the optical frequency domains. In case of the Yb:fiber laser described later in Chapter 3 with $f_{\mathrm{Rep}} \approx 150\,\mathrm{MHz}$ and a central wavelength of $\lambda = 1060\,\mathrm{nm}$, n becomes approximately 1.9×10^6 at this wavelength.

In a real laser system, both parameters f_{CEO} and f_{Rep} are fluctuating, leading to the frequency comb structure washing out in two different ways [5]. Such fluctuations can be thought of as breathing of the comb modes around a fixed point ν_{fix} which is unaffected [51]. For the CEO frequency f_{CEO}, this fixed frequency for its fluctuation is near the carrier frequency ν_c, approximately resulting in a frequency shift of the comb. For fluctuations of the comb's repetition rate f_{Rep} on the other hand, this fixed frequency is close to zero relative to the optical frequencies, leading to a breathing motion of the optical frequency comb. This case has a significant impact on the comb as fluctuations of f_{Rep} scale with the modal index n. Taking the n value for the Yb:fiber laser example above, a repetition rate change of only about 79 Hz already results in a shift of the corresponding comb line by about 150 MHz, or one repetition rate. This corresponds to a change in res-

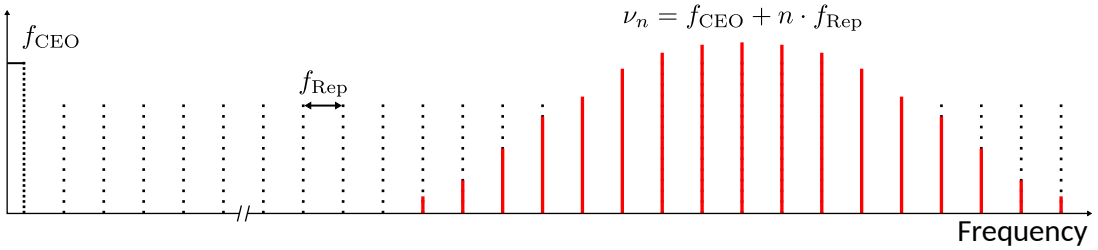

Figure 2.3: The frequency comb's spectrum is defined by the comb equation as a function of two radio frequencies. The repetition rate f_{Rep} governs the comb's spacing, while the carrier envelope offset frequency f_{CEO} offsets it from zero.

onator length on the order of the Yb:fiber lasers wavelength, which can be easily caused by random fluctuations or drifts. This necessitates the active stabilization of the frequency comb and the following sections are aiming to give an understanding of the required tasks for its realization. This involves both nonlinear optical effects for the measurement of the comb's constituting frequencies and electronics for their stabilization.

2.2.1 Nonlinear optical effects

In this section, a short introduction into nonlinear optics is given as the optical frequency combs in this work require both spectral broadening and harmonic generation for frequency stabilization. Both of these can only be described via nonlinear optical effects. In addition to this, the Mid-IR frequency comb is generated from the Near-IR radiation of an Yb:fiber laser, requiring additional nonlinear processes for frequency conversion. This section is based on the explanations given in reference [52].

The interaction of a complex light field $\tilde{E}(t) = E\exp(-i\omega t)+\text{c.c}$ and matter is characterized by the interplay of the electromagnetic light fields and the movement of the electrons inside atoms and molecules responding to these fields. As such, the lights electric field $\tilde{E}(t)$ induces a displacement of the electrons or a polarization $\tilde{P}(t)$ inside the materials it passes through. These electrons are subjected to binding potentials that at low field strengths and displacements can be approximated as a harmonic oscillator. As such, the potential exerts a linear force on the electrons depending on their displacement by the light field, and the materials polarization becomes

$$\tilde{P}(t) = \epsilon_0 \chi^{(1)} \tilde{E}(t), \tag{2.3}$$

with ϵ_0 the vacuum permittivity and $\chi^{(1)}$ the linear susceptibility of the material. This linear polarization leads to the linear refractive index n_0 via $n_0^2 = \epsilon = 1+\chi^{(1)}$. However, at the higher electromagnetic field strengths of pulsed laser systems, the electrons are displaced enough for the binding potential to become increasingly anharmonic and addi-

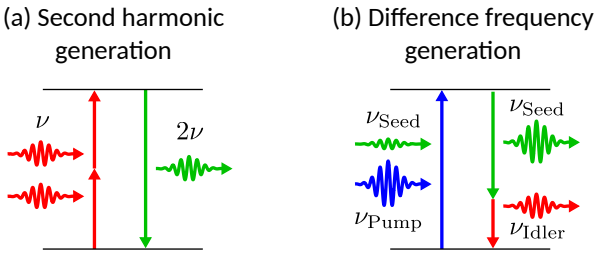

Figure 2.4: Two relevant $\chi^{(2)}$ nonlinear processes for spectral shifting. (a) Second-harmonic generation, doubling the frequency ν of incoming photons and converting two photons to one. (b) Difference frequency generation, generating a difference frequency *idler* photon from two incoming *seed* and *pump* photons.

tional polarization terms have to be considered. Thus, the polarization of the material becomes

$$\tilde{P}(t) \;=\; \epsilon_0 \times \sum_{n=1}^{\infty} \chi^{(n)} \tilde{E}^n(t) \;=\; \sum_{n=1}^{\infty} \tilde{P}^{(n)}(t) \;=\; \tilde{P}^{(1)}(t) + \tilde{P}^{\mathrm{NL}}(t). \tag{2.4}$$

Conversely, the nonlinear part of the induced polarization $\tilde{P}^{\mathrm{NL}}(t)$ interacts with the light field itself via the inhomogeneous wave equation

$$\nabla^2 \tilde{E}(t) - \frac{n^2}{c^2} \frac{\partial^2 \tilde{E}(t)}{\partial t^2} \;=\; \frac{1}{\epsilon_0 c^2} \frac{\partial^2 \tilde{P}^{\mathrm{NL}}(t)}{\partial t^2}. \tag{2.5}$$

The right-hand side of the equation can be interpreted as a measure of the acceleration of the charges within the nonlinear medium. As such, the electric field becomes driven by the nonlinear polarization $\tilde{P}^{\mathrm{NL}}(t)$ consistent with Larmor's theorem stating that accelerating charges results in electromagnetic radiation. This means that nonlinearities in the mediums response to light lead to new frequency components generated coherently inside the medium. This is the basis of nonlinear optics and different susceptibility orders $\chi^{(n)}$ have a different impact on the light's spectrum. In the following, these are denoted as the nth order nonlinearity, and in Figures 2.4 and 2.6 some effects arising from these are shown.

Second harmonic generation

As one example, irradiating a crystal with a high second-order nonlinearity $\chi^{(2)}$ generates a polarization

$$\tilde{P}^{(2)}(t) \;=\; 2\epsilon_0 \chi^{(2)} E E^* + \left(\epsilon_0 \chi^{(2)} E^2 e^{-i2\omega t} + \text{c.c.}\right) \tag{2.6}$$

inside the crystal. This polarization contains both a non-oscillating term (*optical rectification*, first term in Equation (2.6)) and a term oscillating at double the frequency of the input radiation, which is called second harmonic generation (SHG). This is shown in Figure 2.4(a), for this process two photons at the optical frequency ν are converted to

one photon at the doubled frequency 2ν for energy conservation. This process is commonly used throughout the setup at different points which is described later in Chapters 3 and 4.

Difference frequency generation

$\chi^{(2)}$ nonlinearities can also be used to mix the input of two different light fields at frequencies ω_1 and ω_2 (with $\omega_1 > \omega_2$). With their combined electric field

$$\tilde{E}(t) \;=\; E_1 e^{-i\omega_1 t} + E_2 e^{-i\omega_2 t} + \text{c.c.} \tag{2.7}$$

the nonlinear polarization $\tilde{P}^{(2)}(t)$ takes on the form

$$\begin{aligned}\tilde{P}^{(2)}(t) \;=\; 2\epsilon_0\chi^{(2)}\left[E_1E_1^* + E_2E_2^*\right] + \epsilon_0\chi^{(2)}\Big[&E_1^2e^{-i2\omega_1 t} + E_2^2e^{-i2\omega_2 t} \\ &+2E_1E_2e^{-i(\omega_1+\omega_2)t} + 2E_1E_2^*e^{-i(\omega_1-\omega_2)t} + \text{c.c.}\Big].\end{aligned} \tag{2.8}$$

Here, the last two terms produce additional frequency components at the input frequencies sum $\omega_1 + \omega_2$ (sum frequency generation (SFG)) and their difference $\omega_1 - \omega_2$ (difference frequency generation (DFG)). In this work, the latter effect is used to mix two Near-IR pulses down to the Mid-IR frequency range, and this situation is shown in Figure 2.4(b). Here, one high-energy *pump* photon at frequency $\nu_{\text{Pump}} \mathrel{\widehat{=}} \omega_1/(2\pi)$ overlaps with a second *seed* photon at lower energy $\nu_{\text{Seed}} \mathrel{\widehat{=}} \omega_2/(2\pi)$ inside the nonlinear medium. The energy of the pump photon is split in two, with one at the same frequency ν_{seed} as the input seed photon (amplifying the seed beam) and one *idler* photon at a new frequency

$$\nu_{\text{Idler}} \;=\; \nu_{\text{Pump}} - \nu_{\text{Seed}} \tag{2.9}$$

in the Mid-IR range.

Phase matching and quasi-phase matching of nonlinear processes

In the descriptions of both SHG and DFG only the time dependence has been considered for the electrical fields. For a full description of the process also the spatial dimension of these processes is required, necessitating the description of the electrical field of the frequency component j as travelling waves of the form

$$\tilde{E}_j(z,t) \;=\; Ee^{-ik_j z}e^{-i\omega_j t} + \text{c.c} \tag{2.10}$$

with the propagation direction z and the corresponding wave number k_j [52]. This wave number $k_j \;=\; 2\pi n(\lambda_j)/\lambda_j$ itself is a function of the wavelength λ_j and the nonlinear

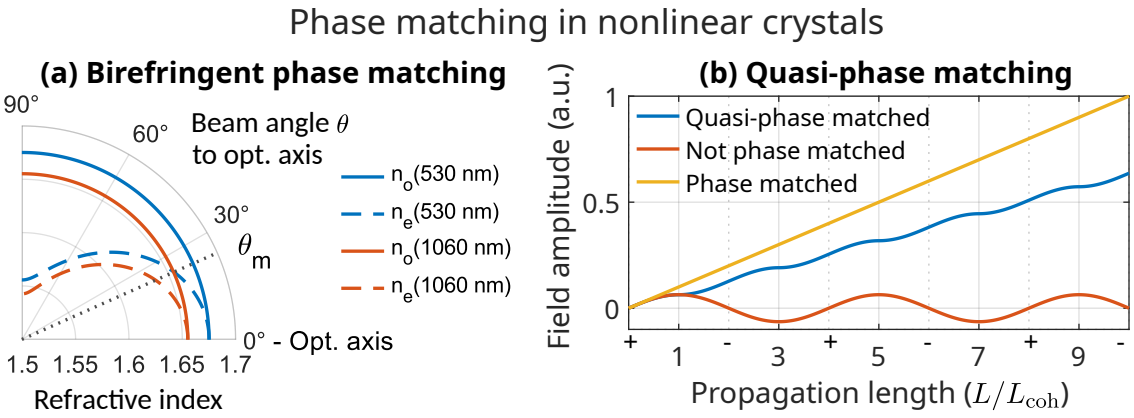

Figure 2.5: (a) Tilting a uniaxial crystal such as BBO at an angle θ between its optical axis ($n_e(\theta) = n_o$) and the lights propagation direction results in a phase matched SHG process. A dotted line shows the phase matching angle θ_m with matching refractive indices of in- and output. Limiting the shown refractive indices results in strong distortion of the index ellipsis. (b) Quasi-phase matching due to periodical poling of one axis in a nonlinear crystal (blue curve) compared with perfect phase matching (yellow) and no phase matching at all (red). Small signs along the propagation length denote the crystals poling orientation.

mediums refractive index $n(\lambda_j)$ at this wavelength. The nonlinear processes happen at every point in the nonlinear medium by the interaction of the light with the charges in the area. As such, the generated light interferes with itself and the generation of new frequency components becomes dependent on the phase mismatch Δk of the input and output frequencies of the process. For DFG, this mismatch is given as

$$\Delta k = k_{\text{Pump}} - k_{\text{Seed}} - k_{\text{Idler}}. \tag{2.11}$$

Due to dispersion, this Δk is typically non-zero leading to an early onset of back conversion from the idler to both pump and seed after the non-linear coherence length $L_{\text{coh}} = \pi/|\Delta k|$, limiting the efficiency of the DFG process [49]. At $\Delta k = 0$, this back conversion would only take place after the pump beam has been depleted signficantly after conversion to both idler and seed beams. This effect can be mitigated using birefringent crystals where the refractive index depends on the lights polarization and propagation directions with respect to the crystals orientation. This allows for phase matching of nonlinear processes in cases where the newly generated frequencies are polarized differently than at least one input frequency component. In the uniaxial case (covering e.g. β-barium borate (β-BaB_2O_4) (BBO)), the lights two linear polarization states experience two different refractive indices (*ordinary* n_o and *extraordinary* $n_e(\theta)$), where n_o is a constant and $n_e(\theta)$ is an ellipsis depending on the angle θ between the lights propagation direction and the optical axis where $n_e(0°) = n_o$. In Figure 2.5(a), the ordinary and extraordinary refractive indices of a SHG process in BBO from 1060 nm to 530 nm are shown as functions of the angle θ for both wavelengths (with $n_{o,e}$ taken from [53]). Here, using $\theta = \theta_m \approx 24°$

(the *phase matching angle* for this process) results in the fundamentals n_o and the second harmonics $n_e(\theta_m)$ becoming equal, leading to fulfillment of the phase matching condition $\Delta k = 0$ and therefore a high conversion efficiency..

However, using birefringence for phase matching is not possible at all times, as for big frequency differences (such as from the Near-IR to the Mid-IR) the phase mismatch might not be compensatable by this effect alone. In these cases, a different property of the crystal can aid phase matching, as its effective nonlinear coupling d_{eff} can also depend on the crystal axes orientation, leading to quasi-phase matching (QPM). Inverting one axis can lead to a sign change in d_{eff}, and inversion of this poling at periodic distances $\Lambda/2$ just before the start of back conversion allows for compensation of a non-zero phase mismatch Δk. This leads to a modified phase mismatch Δk_Q of the DFG process,

$$\Delta k_Q \;=\; k_{\text{Pump}} - k_{\text{Seed}} - k_{\text{Idler}} - 2\pi/\Lambda. \tag{2.12}$$

The crystals optimal poling period is given by $\Lambda = 2L_{\text{coh}} = 2\pi/|k_{\text{Pump}} - k_{\text{Seed}} - k_{\text{Idler}}|$. The process of QPM is visualized in Figure 2.5(b), comparing the generation of a new frequency in a QPM process in blue with perfect phase matching with linear gain (yellow curve) and no phase matching at all (red) oscillating around zero field strength. While the overall gain in QPM is not as high as with perfect phase matching, such a process still exhibits a close-to-linear increase in amplitude with the propagation length inside the periodically poled crystal. Additionally, its poling period and other parameters influencing the birefringence such as its temperature can be employed for tunability of the source.

Self-phase modulation

In addition to these second-order nonlinearities, $\chi^{(3)}$ processes are useful for frequency comb generation, for example to broaden the initial spectrum of the pulses to an octave of optical bandwidth. This is required for the f-$2f$ interferometer used to measure and stabilize f_{CEO} as shown in Section 2.2.2. For instantaneous processes, their polarization $\tilde{P}^{(3)}(t)$ takes the form

$$\tilde{P}^{(3)}(t) \;=\; \epsilon_0 \chi^{(3)} \tilde{E}^3(t), \tag{2.13}$$

which combined with an input field $\tilde{E}(t) = E(t)\cos(\omega t)$ becomes

$$\tilde{P}^{(3)}(t) \;=\; \frac{1}{4}\epsilon_0 \chi^{(3)} E^3(t)\cos(3\omega t) + \frac{3}{4}\epsilon_0 \chi^{(3)} E^3(t)\cos(\omega t). \tag{2.14}$$

The first term corresponds to a third-harmonic generation, analogue to the SHG case above. The second one is interesting, as it contains the original electric field $\tilde{E}(t)$ similar to the linear polarization in Equation (2.3), but scaled with the square of its amplitude

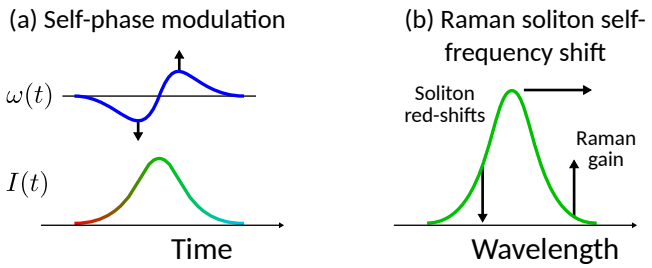

Figure 2.6: Two $\chi^{(3)}$ nonlinear processes used for spectral broadening. (a) Self-phase modulation. The intensity-dependent refractive index introduces a pulse chirp, leading to spectral broadening. (b) Raman soliton self-frequency shift (SSFS) in highly nonlinear fibers (HNLFs). In the presence of both third-order nonlinearities and Raman amplification, the long-wavelength side of soliton pulses is amplified at the expense of the short wavelengths leading to a red-shift.

$E^2(t)$ which is proportional to its intensity $I(t)$. In other words, in the presence of $\chi^{(3)}$ nonlinearities, the materials refractive index n essentially becomes

$$n(t) \;=\; n_0 + n_2 \times I(t) \tag{2.15}$$

with n_0 as the linear refractive index and n_2 as an intensity-dependent refractive index, also known as the Kerr effect.

For laser pulses this means that the central, high intensity peak of the pulse acquires an additional nonlinear phase

$$\Phi_{\mathrm{NL}}(t) \;=\; -n_2 I(t)\omega L/c \tag{2.16}$$

proportional to $I(t)$ and the propagation length L through the $\chi^{(3)}$ nonlinearity. The time-derivative of this phase is the acquired frequency deviation due to the Kerr effect

$$\delta\omega(t) \;=\; \frac{d}{dt}\Phi_{\mathrm{NL}}(t), \tag{2.17}$$

which means that the pulses become chirped and their spectrum is broadened to both higher and lower frequencies while the pulses time envelope stays unchanged. This process called self-phase modulation (SPM) is shown in Figure 2.6(a). This process contributes to the generation of supercontinua in optical fibers, which is used to generate an octave-wide spectrum for the measurement and stabilization of f_{CEO}. However, many other higher-order effects contribute to supercontinuum generation, including self-steepening which delays the central part of the pulse relative to its wings due to the same Kerr effect, Raman SSFS and high-order soliton fission among many others. As such, SPM only serves as one example by which an optical spectrum can be broadened via an instantaneous third-order nonlinearity. For a full review on supercontinuum generation, see reference [54].

SPM also enables another interesting aspect of light propagation in optical fibers. There, the chirp induced by the fiber's dispersion can counteract the chirp induced by SPM. In

this case, pulses propagate along these fibers keeping its shape in both time and spectral domain. Such pulses are called fundamental solitons. Higher order solitons can be generated by increasing the optical power coupled into the fiber, leading to periodic changes of the soliton in both time and spectrum. At very high intensities with corresponding high soliton orders such as those occurring in the highly nonlinear fibers (HNLFs) used in Chapters 3 and 4, additional effects become involved. These can result in the soliton breaking up into multiple fundamental ones at different wavelengths [54].

Raman soliton self-frequency shift

In addition to these polarization effects stemming from the interaction of the electrons movement and the light, the light can interact with the phonons, vibrational modes and other density fluctuations of the molecules and atoms inside the optical medium. These *Raman scattering* interactions can move electrons between different energy levels in the material via higher intermediate energy levels, leading to excitations followed by a radiative decay. These scattering effects are slightly delayed compared to the instantaneous electron reactions of previously described nonlinear effects and can lead to a frequency shift of the scattered light. In thermal equilibrium, lower atomic or molecular energy levels are populated more than higher levels and as such the excitation to higher levels is favored, leading to a decrease in frequency in the scattered light (*Stokes* components of Raman scattering). Depending on the type of vibration the light is interacting with, these shifts have different orders of magnitude. For the interaction with optical phonons, called *Raman* scattering, these induced shifts have the highest value of about $467\,\mathrm{cm}^{-1}$ for SiO_2 fibers [52]. There, for an initial wavelength of 1060 nm the Stokes wavelength is generated around 1115 nm. At low intensities and optical bandwidths, these scattering processes occur spontaneously with linear gain and are mostly driven by random fluctuations and noise. Higher laser intensities however enable a targeted stimulation of this process with high efficiency and exponential gain at the Stokes wavelength. In the case of solitons with high intensity and sufficient bandwidth traveling along HNLFs, this process can serve to transfer energy from the higher frequency flank continuously to the lower frequencies. This leads to a continuous and coherent red-shift of the solitons over the length of the fiber [35, 55, 56]. This Raman SSFS is shown in Figure 2.6(b) and it is used in this work to generate a red-shifted copy of the Yb:fiber laser pulse to serve as the seed for the DFG process.

2.2.2 Frequency comb stabilization

As mentioned at the end of the introduction of this section, a realized optical frequency comb requires both the measurement of its constituting frequencies f_{Rep} and f_{CEO} and

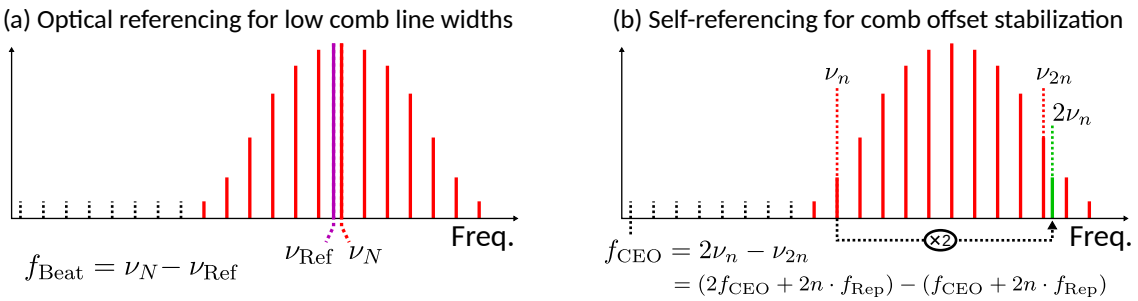

Figure 2.7: (a) By interfering a highly-stable reference laser at frequency ν_{Ref} with a nearby comb mode ν_N, a beat frequency f_{Beat} is measured and stabilized via the combs' cavity length to transfer the low optical line width of the reference to the frequency comb. (b) Idea behind the measurement of the f_{CEO} carrier-envelope-offset frequency. The optical frequency comb is broadened to an octave-wide spectrum. Lower-frequency comb modes are then frequency-doubled to interfere with fundamental comb lines at higher frequencies. The resulting beat notes can be detected and used for stabilization of f_{CEO}.

their subsequent stabilization. This section serves to describe how these frequencies are measured, requiring nonlinear optics for f_{CEO}, and the electronic devices required for their stabilization. Of these two frequencies, the repetition rate f_{Rep} is easily accessible by directing the comb's output onto a photodiode and counting the pulses per time frame, and is stabilized by adjusting the cavity length accordingly as explained in the last part of this section. However, as stated above, the optical comb modes are high-order multiples of this repetition rate with their comb index n possibly being on the order of millions. As such, the stabilized repetition rates residual phase noise is multiplied by n^2 for each comb mode [5]. For the given example of the Yb:fiber comb of $n = 1.9 \times 10^6$ this results in an increase of about 126 dB in phase noise, washing out the comb structure significantly. For this reason, it is beneficial to interfere a single comb mode ν_N with a highly stable CW reference laser at frequency ν_{Ref} with a known low line width ($\leq 1\,\text{kHz}$) and stabilize the resulting beat note f_{Beat}

$$f_{\text{Beat}} = \nu_N - \nu_{\text{Ref}} = f_{\text{CEO}} + N \times f_{\text{Rep}} - \nu_{\text{Ref}} \tag{2.18}$$

instead. This frequency is of the same order of magnitude as f_{Rep} and f_{CEO} and thus accessible using RF equipment, while the optical frequencies of are too high to be measurable directly. This way, the low line width from the reference laser transfers to the stabilized frequency comb's spectrum and the repetition rates phase noise decreases by n^2. Changes in

$$f_{\text{Rep}} = \frac{\nu_{\text{Ref}} + f_{\text{Beat}} - f_{\text{CEO}}}{N} \tag{2.19}$$

are then dominated by slow drifts of the reference lasers frequency which can be corrected for by tuning its cavity parameters such as its length or temperature. This optical referencing scheme is shown in Figure 2.7(a).

Self-referencing the comb for offset stabilization

The f_{CEO} frequency is not accessible easily, as a photodiode is only able to measure the intensity of the light. The CEP however is invisible to the detector as the electric field oscillates too fast, making a direct measurement of f_{CEO} impossible. However, by harmonic shifting of the frequency comb and overlapping both the fundamental and its mth harmonic on such a photodiode, it becomes possible to measure their beat frequency $(m-1) \times f_{\mathrm{CEO}}$. This mechanism is called *self-referencing* as this beat is generated from the output of the frequency comb itself. In this work, an f-$2f$ interferometer beating the comb with its own SHG is set up for this purpose. Its principle is shown in Figure 2.7(b). Before the f-$2f$ interferometer, the comb's spectrum is broadened to more than an octave of bandwidth via supercontinuum generation [54]. Following this, comb modes ν_n on the low frequency edge of the spectrum are frequency-doubled and interfered with modes ν_{2n} on the high frequencies on a photodiode. Its output contains the difference frequency of these $2\nu_n$ and ν_{2n} modes, which is exactly f_{CEO},

$$2\nu_n - \nu_{2n} \;=\; (2f_{\mathrm{CEO}} + 2n \times f_{\mathrm{Rep}}) - (f_{\mathrm{CEO}} + 2n \times f_{\mathrm{Rep}}) \;=\; f_{\mathrm{CEO}}, \tag{2.20}$$

which can then be filtered out and measured for stabilization.

As f_{CEO} is caused the difference in phase and group velocities of the pulses in the oscillator, suitable control parameters need to impact this difference. The energy of the pulses in the oscillator cavity can be used for its control, as the Kerr effect (also responsible for SPM) leads to higher energy pulses experiencing a higher nonlinear refractive index according to Equation (2.15), in turn decreasing their group velocity. This is very simplified however and a lot more effects than the Kerr effect do play a role in the dynamics of the frequency comb. For a comprehensive theoretical description of these dynamics in fiber lasers as used in this work, see reference [57]. The pulse energy of the frequency comb can be manipulated either directly via loss modulation in the cavity itself or indirectly via the modulation of the oscillators pump power [57]. Using the latter leads to a finite fixed-point frequency for the f_{CEO} manipulation near the oscillators carrier frequency, resulting in some coupling of the lasers repetition rate and its CEO [51]. This method is used for the fast f_{CEO} feedback loop in the Yb:fiber comb driving the Mid-IR source (Chapter 3), while the Tm:fiber comb (Chapter 4) uses this method for its slow feedback loop and direct cavity loss modulation for the fast loop. Additionally, dispersive elements can be tuned as well, for example fiber Bragg gratings via their temperature, which is used in the Yb:fiber comb for slow f_{CEO} feedback control.

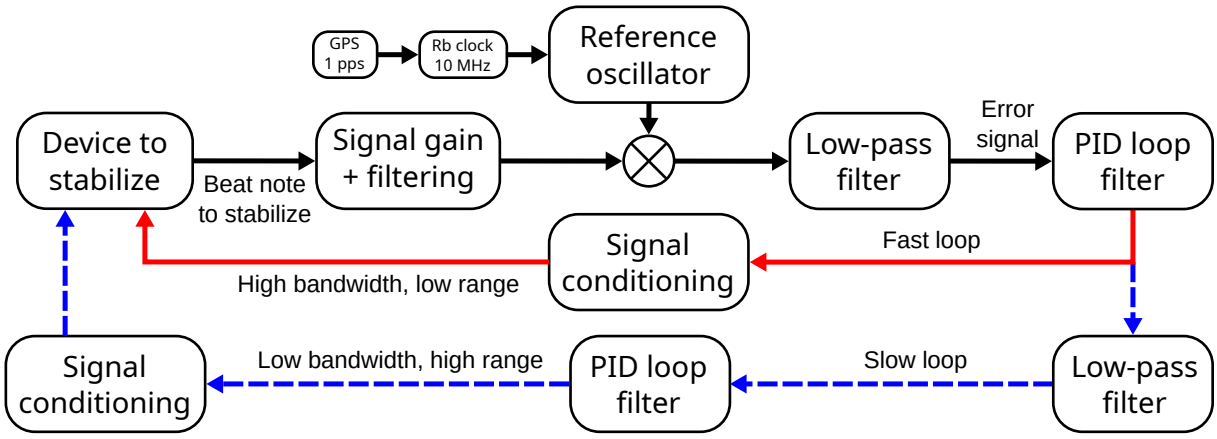

Figure 2.8: General design for the PLL used to lock the comb frequencies. The device to lock generates an RF signal which is measured, conditioned and then compared to a reference oscillator. A PID controller then generates a correction signal for the device to stabilize, which is fed into a fast actuator with low dynamic range. This signal is also low-pass filtered and input to a second PID controller to drive a second, slow actuator with higher dynamic range.

Electronic feedback control implementation

The last sections describe the measurement of both defining frequencies of the frequency comb via (nonlinear) optical setups. In addition to their measurement however, a stabilized frequency comb also requires active feedback, for which a phase-locked loop (PLL) is used. In Figure 2.8 the general setup used in this work is shown. These loops work by first measuring, filtering and amplifying the frequency to stabilize (such as f_{CEO}), followed by a phase detector which measures the phase of this frequency relative to a stable RF reference oscillator. Its low-pass filtered output is proportional to the relative phase mismatch of both frequencies and is used as the error signal for a proportional-integral-derivative (PID) loop filter generating the required correction signal. This signal is then amplified and applied to the frequency comb's control parameters to synchronize the frequency-to-stabilize with the reference and lock their phases together. In the experiment, this direct output of the PID filter is used to drive actuators with high bandwidths (from direct current (DC) up to 100 kHz) for short-term stabilization. However, these devices such as small piezo ceramics for end-mirror movement or pump current modulation usually provide only a rather small actuation range of a few 10 to 100 Hz of f_{Rep} or f_{CEO} changes. Slow drifts can cause larger errors, and to compensate those, a second actuator is used alongside this fast one, which is slower but provides a high enough range to correct for these drifts [51]. This slow actuator is driven by a second PID filter which uses the correction output of the first one as its error signal input. In Figure 2.8, the fast stabilization loop is shown in red solid lines, while the slow drift correction uses blue dashed lines. In the entire setup with two frequency combs running, five of these PLLs are implemented. In order to keep their reference oscillators synchronized without drifting

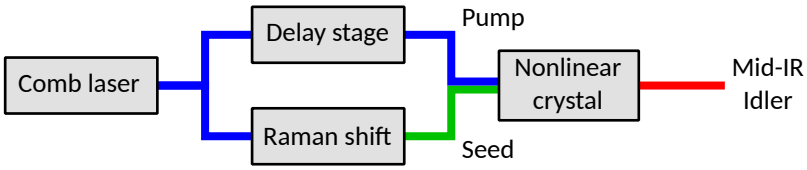

Figure 2.9: Simplified sketch of the Mid-IR sources setup. The output of the comb is split in two, with the pump routed via a delay stage, and the seed undergoing Raman shift. Pump and seed are overlapped in a nonlinear crystal to generate the difference-frequency idler in the Mid-IR.

apart and to reference them to the International System of Units/Système International (SI) standard, they also are phase-locked to a common 10 MHz Rb clock disciplined to the clocks aboard the Global Positioning System (GPS) satellites. This provides the combs with highly stable references to the SI standard with an absolute accuracy of better than 1×10^{-12} over a day of measurements [58, 59].

2.2.3 The Mid-IR frequency comb

In order to generate the Mid-IR frequency comb for spectroscopic applications, the different effects and mechanisms described in the last sections need to be combined. A simplified sketch of this source is shown in Figure 2.9. The output of a Near-IR frequency comb is first split in two parts to serve as pump and seed for the DFG process. The pump is being routed via a delay stage for temporal overlapping with the seed. The seed is experiencing Raman SSFS to generate seed solitons at suitable wavelengths to be able to generate the target Mid-IR wavelengths. Both beams are then recombined in a nonlinear crystal, where they are mixed resulting in the Mid-IR idler output. Using Equations (2.2) and (2.9), the frequency comb for this radiation

$$\begin{aligned}\nu_{\mathrm{Idler}} &= \nu_{\mathrm{Pump}} - \nu_{\mathrm{Seed}} = (f_{\mathrm{CEO}} + n_{\mathrm{Pump}} \times f_{\mathrm{Rep}}) - (f_{\mathrm{CEO}} + n_{\mathrm{Seed}} \times f_{\mathrm{Rep}}) \\ &= (n_{\mathrm{Pump}} - n_{\mathrm{Seed}}) \times f_{\mathrm{Rep}} \\ &= n_{\mathrm{Idler}} \times f_{\mathrm{Rep}}, \end{aligned} \tag{2.21}$$

with comb modal indices for pump and seed $n_{\mathrm{Pump}} > n_{\mathrm{Seed}}$ and the idlers comb modal index $n_{\mathrm{Idler}} = n_{\mathrm{Pump}} - n_{\mathrm{Seed}}$, is only defined by its repetition rate f_{Rep}, becoming CEO-free [31]. The laser is optically referenced by stabilizing a beat frequency f_{Beat} between the reference lasers frequency ν_{Ref} and the closest comb mode ν_N at index N. f_{Rep} thus can be expressed by f_{Beat}, N and the Near-IR comb's offset frequency f_{CEO} via Equation (2.19), and Equation (2.21) becomes

$$\nu_{\mathrm{Idler}} = \frac{n_{\mathrm{Idler}}}{N} \left(\nu_{\mathrm{Ref}} + f_{\mathrm{Beat}} - f_{\mathrm{CEO}}\right), \tag{2.22}$$

which means that both f_{CEO} and f_{Beat} have a significant influence on the DFG comb's structure, even though they are much smaller than the reference lasers optical frequency ν_{Ref}. The Mid-IR source in the experiment is driven by an Yb:fiber laser referenced to a reference laser at 1064 nm and regularly generates radiation at 4 µm. The ratio between these two wavelengths nearly equals the ratio between the corresponding comb indices n_{Idler}/N, so this ratio becomes about 1/4. Changes in f_{Beat} and f_{CEO} of about 4 Hz thus both result in changes of about 1 Hz in the Mid-IR comb line frequencies. This means that for a well-defined Mid-IR frequency comb, all contributing frequencies f_{CEO}, f_{Beat} and ν_{Ref} (which is used to define f_{Rep} in the end) need to be stabilized.

2.3 Optical line shape and noise in the Mid-IR frequency comb

The Mid-IR frequency comb is affected by its environment and physics itself. Vibrations of the laser table acting on the cavity mirrors for example can lead to differences in the laser oscillators cavity length and oscillator temperature fluctuations can affect its dispersion profile. These and other effects lead to noise in both its repetition rate f_{Rep} and its CEO frequency f_{CEO}, both leading noise in the optical frequency of the comb lines. The comb's frequency noise $\delta\omega(t)$ also results in noise of the optical phase $\phi(t)$ of the pulses via $\Delta\omega(t) = d/dt\phi(t)$, and via relating phase changes of 2π to one period T also in timing noise. Other effects like a fluctuating pump current caused by bad filtering in its power supply in both oscillator and pump current can lead to a fluctuating pulse energy from the laser, which is measured as intensity noise. In addition to that, the mere statistical nature of both photons and the generated electrons in a photodiode means that even with these technical noise sources suppressed to a theoretical minimum, some quantum noise affecting both the pulses intensity and their phase or frequency always persists.

These noise contributions result in the addition of noise sidebands to the frequency comb, possibly leading to line broadenings and a reduction in both resolution and sensitivity. These sidebands are measured as power spectral densities (PSDs) which are functions $S_x(f)$ of the offset frequency to the comb lines. Their measurement and an understanding of the possible noise sources thus becomes crucial to the optimization of the frequency comb and this section aims to develop a basic understanding of both intensity and phase noise and how the latter relates to the optical line width of the Mid-IR frequency comb. These sections closely follow [49]. In addition to this the influence of modulations of the pump/seed delay in the Mid-IR source on the comb line shape is explored. Such modulations were used to stabilize the source to a relative delay with suppressed intensity noise in previous works [14, 46, 47]. It is shown here however that they lead to the generation of

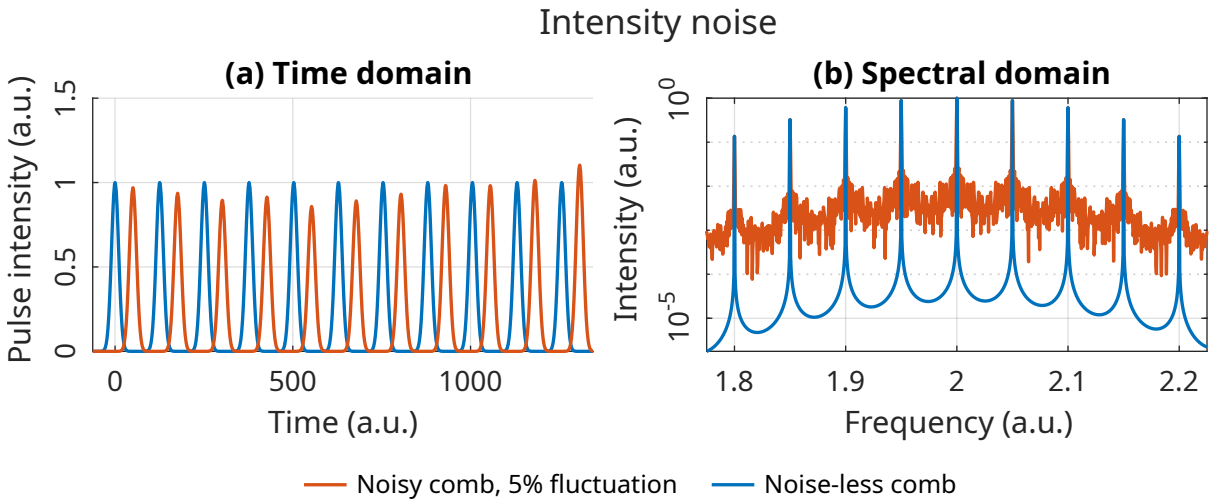

Figure 2.10: (a) Comparison of the pulse train from a mode-locked laser with no intensity noise of the generated pulses (blue pulses) with the pulse train of a laser system with pure intensity noise of 5 % strength (red pulses). (b) Optical spectrum of both combs plotted logarithmically, showing that the noise-less source provides a better spectral contrast than the noisy comb, allowing for a higher spectroscopic sensitivity.

additional sidebands to the spectrum, possibly negatively affecting the resolution of this and similar setups negatively [40, 41, 60–62]. The section then closes with some details on the Mid-IR detection in a FTIR which is also affected by the frequency comb's noise.

2.3.1 Relative intensity noise

One main characteristic of a mode-locked laser is the energy stability of its output pulses [63, 64]. As these devices are subjected to environmental influences, parameters like the pump strength of both its oscillator and subsequent amplifiers can change which can transfer to the energy of the generated pulses. In addition to that, the discrete nature of photons leads to their arrival at random time intervals, leading to a so-called shot noise background with a flat PSD depending only on the lights intensity. The effect of pure intensity noise is shown in Figure 2.10 in both time and spectral domain. In these plots, two laser systems are simulated. The blue curve shows a laser system whose pulse train is noise-less with equal pulse energies over the entire train. The red curve, slightly offset for clarity, shows the output of a second laser with normally distributed random-walk fluctuations with a standard deviation of 5 %. These result in well-visible changes in the pulses intensity in the time-domain picture (a). Subplot (b) shows the comb's optical spectrum. While the noise-free comb provides a high spectral contrast between comb lines, the noisy comb provides significantly less contrast due to the noise introducing sidebands to the comb lines. For spectroscopy this means that features need stronger absorption for them to be detectable with the noisier comb.

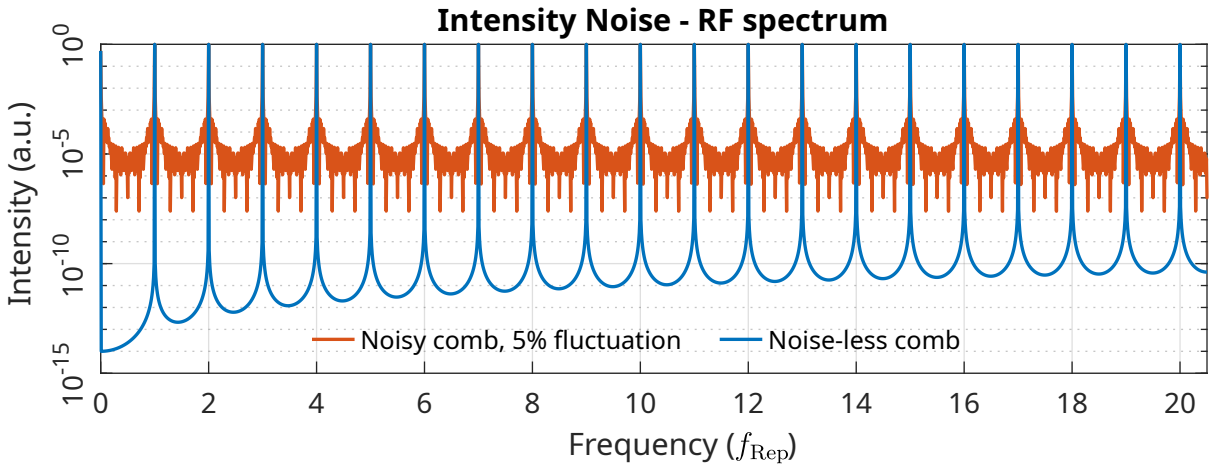

Figure 2.11: Simulated measurement of the combs' pulse train from Figure 2.10 with a photodiode and an RF analyzer. In blue, the noise-less comb is *measured*, the red curve shows the results for the comb with 5 % intensity fluctuations. This plot shows that the intensity noise is affecting all f_{Rep} harmonics equally.

The intensity noise of a mode-locked laser system is characterized via its PSD $S_I(f)$. This function of the sideband frequency shows the power of the noise sidebands relative to the average laser power. Measuring the RIN in a real laser system can be done using a photodiode to measure its power over time and a spectrum analyzer [65], as is simulated for the two combs in Figure 2.11(a). The measured RF signal consists of a DC signal around the base-band $f = 0$ together with peaks repeating at the repetition rate f_{Rep}. One characteristic for intensity noise is that it affects all harmonic peaks equally as Figure 2.11 shows clearly. Therefore it is sufficient that the measurement system provides a bandwidth of up to $f_{\mathrm{Rep}}/2$ to measure the intensity noise PSD $S_I(f)$. Normalizing $S_I(f)$ to the average power for the frequency comb results in the RIN $S_N(f)$ (with N indicating this normalization). By integrating this function between the reciprocal measurement duration $f_1 = 1/T_{\mathrm{meas}}$ and the measurement bandwidth $f_2 < f_{\mathrm{Rep}}/2$ the root-mean-square (RMS) intensity fluctuations within the given duration is calculated as

$$\sigma_N[f_1, f_2] = \sqrt{\frac{1}{\pi}\int_{f_1}^{f_2} S_N(f)\, df}. \tag{2.23}$$

This property is called RIN and is usually given as a percentage of the average laser power.

For the example of the random walk above, the PSD for one single walk and the corresponding integrated noise following Equation (2.23) is plotted in Figure 2.12, showing a simple decline in noise power with increased offset frequency. For this function, most noise is contributed by the lower frequencies. However, in a real laser system with different noise causes this plot shows more interesting features. At low offset frequencies, the noise is dominated by mechanical influences on the laser system such as sound waves

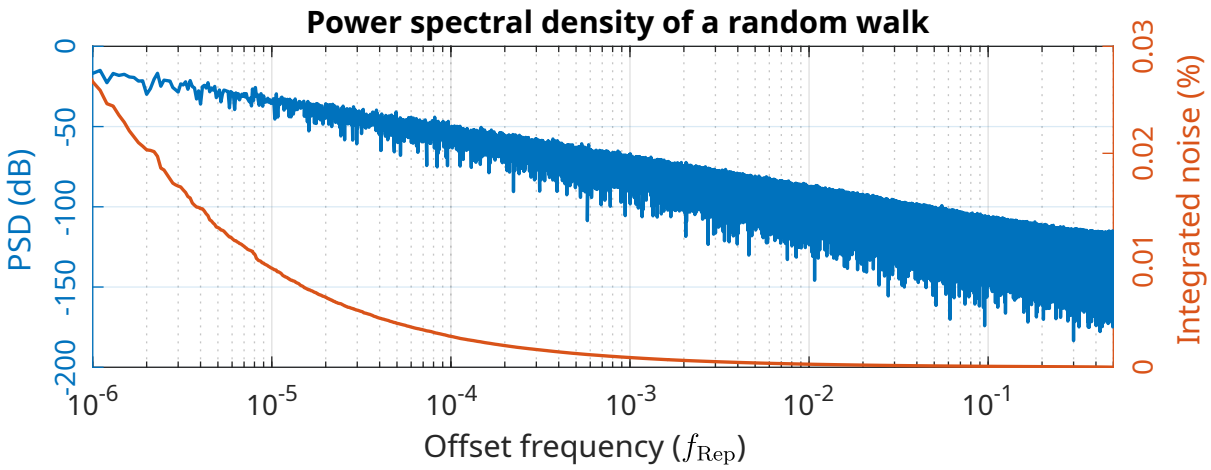

Figure 2.12: Simulated power spectral density (left axis) and integrated noise (right axis) of a random walk similar to the simulations in Figures 2.10 and 2.11.

and vibrations of the optics and devices, which overall exhibit a similar frequency characteristic. Towards higher frequencies, nonlinear effects caused by the gain medium and comb stabilization mechanics together with quantum noise play a role. In the frequency combs discussed in this work, stabilization mechanisms serve to suppress the noise within their locking bandwidth as characterized by servo bumps in the PSD. This leads to the mentioned nonlinear effects and resonances contributing the most to the integrated noise, while it becomes flat for lower frequencies, contrary to the integrated noise shown in Figure 2.12. At some point typically well below 10 MHz, the measured signal is dominated by the shot noise of the detection, caused by the statistical nature of photons. Additionally, resonances at certain sideband frequencies can occur relating to mechanical or other resonances in the laser system. Examples for real PSDs are shown later in Chapters 3 and 4 for the phase noises of both used frequency combs and their heterodyne beat.

2.3.2 Phase noise

For a mode-locked laser and optical frequency comb, another important characteristic in addition to its intensity noise is its phase noise quantifying fluctuations of the phase of its constituting frequencies. This quantity is related with both the comb's timing noise via relating a phase of 2π with one oscillator roundtrip $1/f_{\mathrm{Rep}}$ and its frequency noise as the phase noises time derivation. Caused by fluctuations of the cavity length for example due to vibrations of its end mirrors the pulses repetition rate fluctuates around the nominal f_{Rep} value. In addition to this, Equation (2.15) describes the nonlinearity of the refractive index due to the Kerr effect. This means that intensity noise also becomes a contributing factor to the phase noise of the laser, as higher intensities lead to higher refractive indices and thus a higher optical cavity length, decreasing f_{Rep}. Similarly, phase noise can also lead to intensity noise, as a lower repetition rate can lead to more energy stored in the

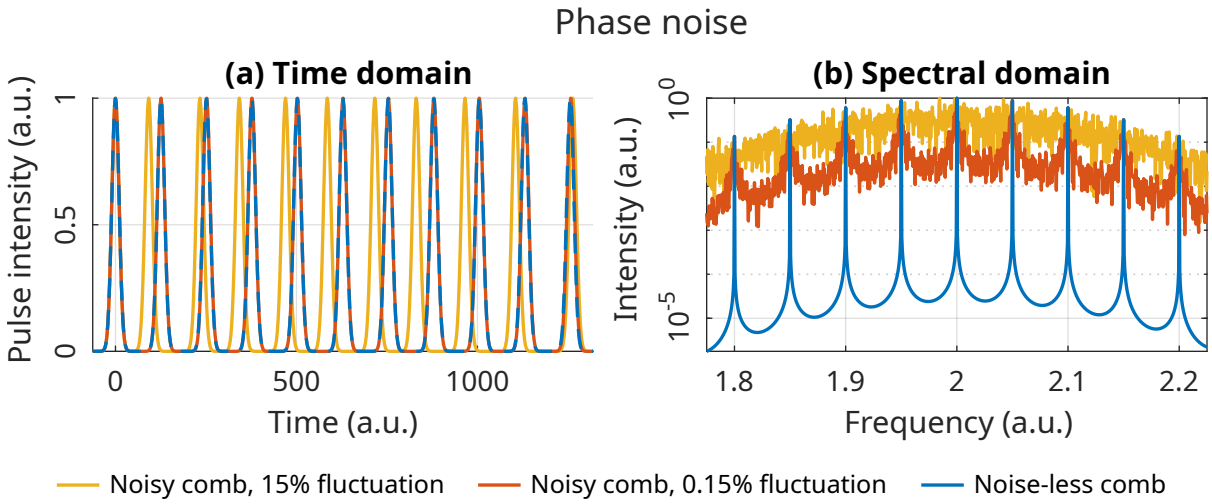

Figure 2.13: (a) Comparison of the output of mode-locked lasers in the time domain. The blue curve shows a laser with noise-less timing, the red curve shows fluctuations of the emitting time of the pulses of 0.15 % and the yellow curve shows such fluctuations with 15 % strength. (b) shows their optical spectrum on a logarithmic scale, similar to Figure 2.10, again showing the decreasing contrast with higher noise until the comb structure completely washes out.

medium before extraction by the next pulse and vice versa. Both intensity noise and phase noise of mode-locked laser systems are thus coupled with each other and one does not occur in isolation without the other occurring as well.

Here however, similar to the simulations done above for intensity noise (Figures 2.10 and 2.11), the phase noise is viewed in isolation. In Figure 2.13, three different frequency comb pulse trains are shown, with the time domain shown in (a) and the optical spectrum shown in (b). In blue, the same noise-less comb as above is shown. In red a comb with 0.15 % timing fluctuations is shown, which on the shown time scale is indistinguishable from the noise-less comb. The yellow curve shows a strongly fluctuating timing at 15 % strength. In the spectral domain, both noisy combs show significantly less spectral contrast between the comb peaks with them completely washing out for the yellow curve. It is notable that even the comb with 0.15 % fluctuation shows a significantly higher noise floor than the comb affected by intensity fluctuations of 5 % shown in Figure 2.10 which is a very high number compared to for example fluctuations of 0.1 % measured with the Yb:fiber laser shown in Chapter 3.

In terms of measurement, the phase noise is more difficult to acquire than the intensity noise, as it is inherently related to the f_{Rep} peaks in the RF spectra of the photodiodes output and is not part of the base band signal like the intensity noise is. In addition to this, a real measurement does not only contain phase noise as mentioned. To accurately measure it, the output of this photodiode is thus directed to a phase detector in which its phase is measured against a reference oscillator matching the carrier frequency $n \times f_{\mathrm{Rep}}$ at a phase offset $\theta = \pi/2$ using a PLL. The base band output of this phase detector is

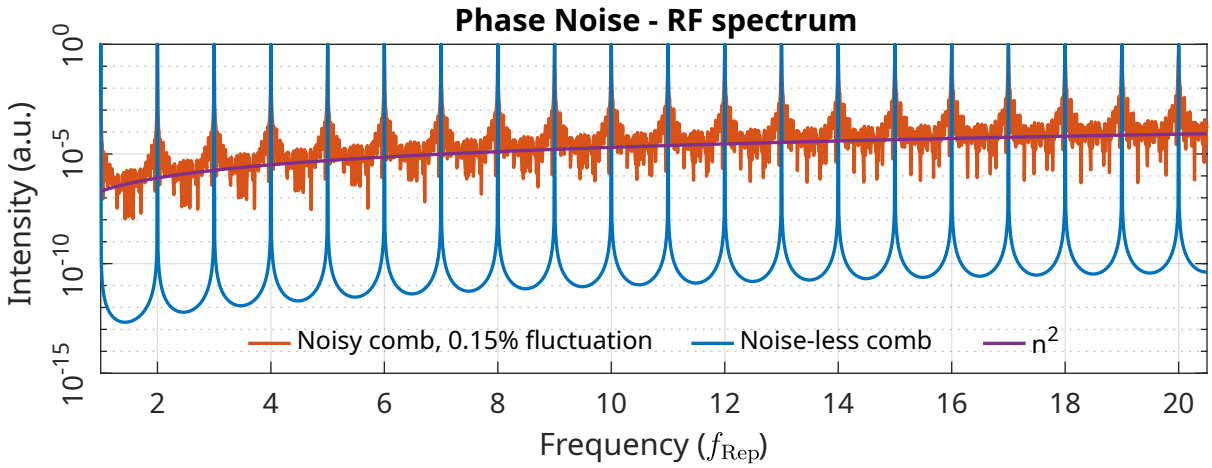

Figure 2.14: Simulated measurement of two pulse trains with a photodiode and an RF analyzer. In blue, a noise-less comb is *measured*, the red curve shows the results for a comb with 0.15 % in timing fluctuations. This plot shows that the phase noise affects higher f_{Rep} harmonics more, with the strength being proportional to n^2.

proportional to the phase deviations and can then be analyzed using an RF analyzer. This device returns a measure $S_\phi(f)$ as a one-sided PSD of these phase deviations as a function of th noise sidebands offset frequency $f > 0$ relative to the carrier oscillations power [65]. For simplicity, integrated measurement devices such as signal source analyzers (SSAs) contain the required electronics already to provide users with a quick way of measuring phase (and intensity) noises of electronic sources. In Figure 2.14, a measurement of the signal of two combs (in blue the noise-less comb and in red one with 0.15 % in timing fluctuations) coming from a photodiode is simulated, similar to the one in Figure 2.11 for the intensity noise. From this simulation it becomes apparent that the phase noise increases in strength with the square of the increasing harmonic order n^2 which is plotted in the figure together with the simulation. For this random-walk case, the simulated phase noise power spectral density $S_\phi(f)$ looks similar to the case of the random-walk intensity noise shown in Figure 2.12.

The normalized PSD $S_\phi(f > 0)$ is a measure for the symmetric sideband's intensity on both sides of the f_{Rep} harmonic that was detected using the SSA and is double the two-sided PSD $S_\phi^{\mathrm{two-sided}}(f)$ defined for $-\infty < f < \infty$. For this work, the single-sideband power spectral density (SSB PSD) $\mathcal{L}_\phi(f)$ measuring the power on only one side of the carrier is used, which is defined as $\mathcal{L}_\phi(f) = S_\phi(f)/2$ [66] or $\mathcal{L}(f) = S_\phi^{\mathrm{two-sided}}(f > 0)$ [63]. Analogue to the integrated RIN $\sigma_N[f_1, f_2]$, an integrated phase noise $\sigma_\phi[f_1, f_2]$

$$\sigma_\phi[f_1, f_2] = \sqrt{2 \int_{f_1}^{f_2} \mathcal{L}_\phi(f)\, df} \tag{2.24}$$

between the reciprocal measurement duration $f_1 = 1/T_{\text{meas}}$ and the measurement bandwidth $f_2 < f_{\text{Rep}}/2$ is defined. This integrated phase noise shows the RMS phase fluctuation of the measured carrier frequency during a measurement of duration T_{meas}. Using Equation (2.24), a common definition of the full-width at half-maximum (FWHM) line width $f_{3\,\text{dB}}$ of the considered oscillation is given as

$$1\,\text{rad} = \sqrt{2\int_{f_{3\,\text{dB}}}^{\infty} \mathcal{L}_\phi(f)\,df}, \tag{2.25}$$

as at an integrated phase noise of 1 rad, the total power is distributed equally between the carrier oscillation and its phase noise sidebands [66].

2.3.3 Optical line width

The optical spectrum of the frequency comb is connected to the frequencies to stabilize via the comb equation Equation (2.2) on page 7, defining the frequency of a comb tooth ν_n by both its repetition rate f_{Rep} and its CEP offset frequency f_{CEO}. As seen earlier, the two frequency combs used in this work are stabilized via beating a distinct comb tooth ν_N with a CW reference laser at frequency ν_{Ref} and stabilizing their beat frequency f_{Beat} instead of stabilizing f_{Rep} directly to lower the phase noise of the frequency comb. As such, f_{Rep} is expressible via Equation (2.19) on page 15. This then transfers to the Mid-IR optical frequency comb whose spectrum is defined by Equation (2.22) on page 18, leading to three different sources of phase noise which can degrade the output spectrum. Here, it is explored how the comb's repetition rate phase noise affects its optical spectrum.

The optical spectrum $S_E(\nu) = \left|\tilde{E}(\nu)\right|^2$ of the frequency comb (or optical frequency PSD) is defined by the Fourier transform of the electrical fields autocorrelation function $R_E(\tau)$

$$R_E(\tau) = \langle E^*(t)E(t+\tau)\rangle \tag{2.26}$$

via the Wiener-Khinchin theorem

$$S_E(\nu) = F\left\{R_E(\tau)\right\} = \int R_E(\tau)e^{-i2\pi\nu\tau}d\tau, \tag{2.27}$$

and vice-versa with an additional $1/(2\pi)$ factor for the inverse Fourier transform. For a single comb tooth ν_n, the electric field can be expressed as

$$E_n(t) = E_n \exp\left\{i\left[2\pi\nu_n t + \phi(t)\right]\right\}, \tag{2.28}$$

with the phase term $\phi(t)$ containing the phase noise leading to a frequency fluctuation $f_{\mathrm{Mod}}(t) = \dot{\phi}(t)/(2\pi)$. Calculating the autocorrelation function using this electric field leads to

$$R_{E_n}(\tau) = \left\langle E_n^* E_n e^{-i2\pi\nu_n t + i2\pi\nu_n(t+\tau)} \times e^{-i\phi(t)+i\phi(t+\tau)} \right\rangle = I_n e^{i2\pi\nu_n\tau} \left\langle e^{i\Delta\phi(t,\tau)} \right\rangle, \tag{2.29}$$

with the phase difference $\Delta\phi(t,\tau) = \phi(t+\tau) - \phi(\tau)$ as a function of the delay τ and I_n being constant, neglecting intensity noise. The exponential term containing the phase difference can be expressed differently via the phase noise autocorrelation function $R_\phi(\tau)$,

$$R_{E_n}(\tau) = I_n e^{i2\pi\nu_n\tau} \exp\left[R_\phi(\tau) - R_\phi(0)\right]. \tag{2.30}$$

This function $R_\phi(\tau)$ can be expressed via the one-sided phase noise PSD $S_\phi(f) = 2\mathcal{L}_\phi(f) = 2S_\phi^{\mathrm{two-sided}}(f)$,

$$R_\phi(\tau) = \int_0^\infty S_\phi(f)\cos(2\pi f\tau)df, \tag{2.31}$$

and with this and $1 - \cos(x) = 2\sin^2(x/2)$, the electrical fields autocorrelation $R_E(\tau)$ becomes

$$R_E(\tau) = I_n \exp(i2\pi\nu_n\tau) \exp\left[-4\int_0^\infty \mathcal{L}_\phi(f)\sin^2(\pi f\tau)df\right]. \tag{2.32}$$

This together with Equation (2.27) means that there is a direct link between the phase noises single-sideband power spectral density (SSB PSD) $\mathcal{L}_\phi(f)$ and the optical spectrum $S_E(\nu)$. A high phase noise thus leads to a broad optical spectrum of the corresponding comb line. As such, stabilization of both frequencies f_{Beat} and f_{CEO} is required for a low optical line width in the Mid-IR frequency comb, assuming ν_{Ref} does already provide a low line width.

2.3.4 Effects of pump/seed delay modulation

The Mid-IR comb in this work is generated by DFG between two laser pulses on non-common beam paths of the unshifted pump and the frequency-shifted seed, as shown later in Figure 3.7 on page 41. In the experiment, these beam paths are around 1.5 m long each and contain a multitude of different optics. Over long measurement durations, a stable temporal overlap of pulses from both paths becomes critical, as mirror vibrations or thermal fluctuations of the laboratory or laser table can effect the two beam paths in a different way. In addition to this, it was found that for this type of Mid-IR DFG source keeping the relative pump/seed delay Δt in a small range (≈ 20 fs) can lead to a strong suppression of RIN for the generated Mid-IR radiation [40, 46, 47, 67]. For stable RIN suppression, a piezo-electric delay stage with retro-reflecting mirrors was integrated into the setup for previous works [46, 47]. There, Δt was modulated or dithered with a small amplitude via this delay stage, leading to a modulation of the noise as a function of Δt.

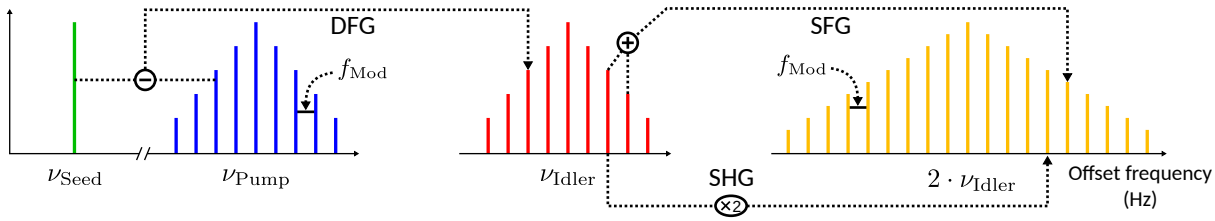

Figure 2.15: Sketch of the transfer of the modulation between the different components in the Mid-IR frequency comb from the pump radiation to the Mid-IR radiations SHG.

A lock-in amplifier was then used to detect this dithering and generate an output phase-shifted by 90°, effectively producing a first-order derivative of the modulation which was used as an error signal for a PID loop filter to drive the stage to the position of minimal noise.

Using this dither locking method works well for the task of RIN suppression and ensuring the long-term stability of the Mid-IR sources output over full spectroscopic measurements. However, as the mirrors enabling this method are constantly moving either towards or away from the light source, the Doppler effect takes place, shifting the frequency of the delayed pump beam by around 1 kHz per 0.5 mm/s of stage velocity [68]. At these velocities, the shift becomes comparable with the line width of the used Non-planar ring oscillator (NPRO) CW reference laser for the optical stabilization of f_{Rep} in the laser setup. In addition to this, a periodic modulation leads to a phase modulation of the pump beam of the frequency comb and subsequently to the generation of sidebands, analogue to the ones desired in electro-optical frequency combs [69], but detrimental in this case.

To understand how this modulation affects the output of the Mid-IR source, first it is discussed how the phase modulation transfers from the pump beam to the Mid-IR sources output. Following this, the actual modulation process is described mathematically. The pump beam is modulated via a small frequency f_{Mod} compared to the optical frequency of a comb tooth ν_{Pump}, adding sidebands $\nu_{\mathrm{Pump}} \pm n f_{\mathrm{Mod}}$, and the seed frequency ν_{Seed} remains unchanged. The nonlinear polarization for both the DFG and SFG processes is shown in Equation (2.8) on page 10. By identifying $\omega_1 \propto \nu_{\mathrm{Pump}} \pm n f_{\mathrm{Mod}}$ and $\omega_2 \propto \nu_{\mathrm{Seed}}$ in the DFG and SFG terms of this equation, it becomes apparent that both resulting output frequencies $\omega_1 \pm \omega_2$ contain these sidebands at the same width as the pump beams modulation. This process is shown in the first step of Figure 2.15.

In Chapter 4, these modulations of the Mid-IR frequency comb at about 4 µm are measured by a heterodyne beat of its SHG with a second optical frequency comb system lasing at about 2 µm. Including the f_{Mod} modulation in Equation (2.6) on page 9 and treating it analogue to the SFG/DFG case results in a doubled offset of the measured sidebands from $n f_{\mathrm{Mod}}$ to $2n f_{\mathrm{Mod}}$. However, as adjacent comb teeth can also interact nonlinearly with each other, SFG between them takes place, conserving the f_{Mod} spacing of the modulation in

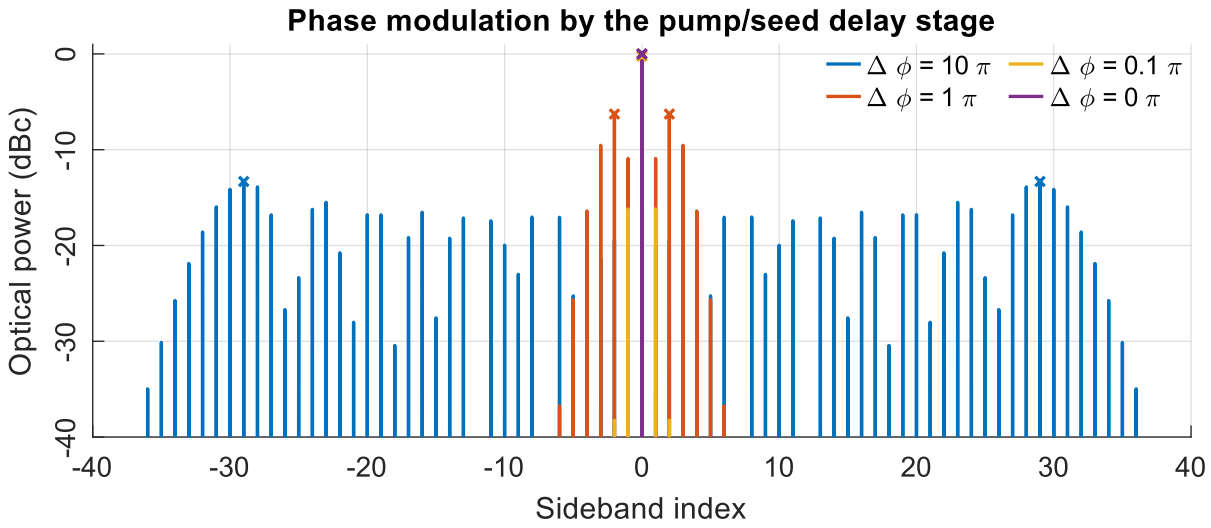

Figure 2.16: Simulation of Equation (2.34) for no modulation and three different $\Delta\phi$, showing how the phase modulation distributes the carrier power towards the modulation sidebands, generating new maxima away from the original carrier (marked with small crosses). The plot shows the logarithmic optical power relative to the unmodulated carrier.

the SHG. The result is a doubling of the modulations width and this process is shown in the second step of Figure 2.15.

Following this general understanding of how the modulation transfers from the pump beam to the Mid-IR output and subsequently its SHG for detection, the actual modulation is described. This section will follow reference [69] closely which provides a comprehensive overview over the generation of optical frequency combs using electro-optic modulators. As mentioned above the voltage-controlled/piezo-electric delay stage can be viewed as one such modulator, so using the phase modulation formalism in the provided reference should explain the findings sufficiently. For the dither locking method, the pump/seed delay stage is modulated using a sinusoidal voltage $U(t) = U_{\mathrm{Mod}} \sin(2\pi f_{\mathrm{Mod}} t)$, with the modulations amplitude U_{Mod} and frequency $f_{\mathrm{Mod}} \ll f_{\mathrm{Rep,Beat,CEO}}$. Applying this modulation to a single mode E_n of the frequency comb results in a modulation of its frequency due to the Doppler effect [68], and as such its electric field becomes

$$E_{n,\mathrm{Mod}} = E_{n,0} e^{i2\pi\nu_n t} e^{i\Delta\phi} = E_{n,0} e^{i2\pi\nu_n t} e^{iKU_{\mathrm{Mod}}\sin(2\pi f_{\mathrm{Mod}} t)}, \tag{2.33}$$

with the acquired phase $\Delta\phi$ and the modulation index K as an additional empirical variable depending on the used stage. The spectrum of this modulated electric field then becomes

$$\tilde{E}_{n,\mathrm{Mod}}(\nu) = E_{n,0} \sum_{n'=-\infty}^{\infty} J_{n'}(KU_{\mathrm{Mod}})\, \delta(\nu - \nu_n - n' f_{\mathrm{Mod}}) \tag{2.34}$$

(with $J_{n'}$ as the Bessel functions of the first kind), showing that the modulation results in the generation of comb-like sidebands spaced by the modulation frequency f_{Mod}. Their

amount and amplitude is governed by the modulated phase $\Delta\phi = KU_{\mathrm{Mod}}$. This sideband generation is simulated in Figure 2.16 for an unmodulated comb mode ($\Delta\phi = 0$) and three different modulation strengths $\Delta\phi = 0.1\pi, \pi$ and 10π. This shows that with increasing $\Delta\phi$ the power of the original comb mode is distributed more and more towards higher sideband indices, forming two maxima towards the edge of the spectrum due to the sinusoidal motion. In Figure 2.16 these maxima are marked with small crosses. Beyond these maxima, the sideband power drops quickly. The amount of sidebands N between these two maxima can be approximated by a linear function $N = 2\lfloor KU_{\mathrm{Mod}} \rfloor$.

Later in the experiment, this modulation takes place at a frequency of 160 Hz, which is less than the line width of the reference laser used for the optical referencing of the frequency comb in our experiment. This means that relative to this laser, the sideband generation is measurable, but in absolute terms the Mid-IR frequency comb becomes broadened. This broadening will affect spectroscopic measurements negatively. As an example, at a modulation strength of $\Delta\phi = 10\pi$, the two maxima are positioned around sideband indices of $n = \pm 30$, or offset frequencies of ± 5 kHz away from the original frequency comb modes. While the dither locking method works well in order to suppress the intensity noise of the Mid-IR source in the long term [46], the line broadening via sideband generation triggered the development of a modulation-free method [70]. This method is described in detail in Chapter 3.

2.3.5 Spectroscopy and Signal-to-noise ratio in the Mid-IR frequency comb

For spectroscopic measurements, the light of the Mid-IR frequency comb is transmitted through a sample cell filled either with a reference vacuum or the medium to analyze and then directed towards a home-built FTIR spectrometer for detection. Its function is outlined in a previous thesis written on this setup [47] and is based on measuring interferograms in a Michelson interferometer [71]. These interferograms are a measured autocorrelation of the electric field following Equation (2.26) on page 25, and following Equation (2.27) its Fourier transform is exactly the spectrum of the interfering light. In this section, the FTIR spectrometer's most important aspects, namely its resolution and the signal-to-noise ratios (SNRs) using this spectrometer are summarized.

Spectrometer resolution

The nominal resolution f_{Res} of the spectrometer is a function of the maximal optical path difference (OPD) Δl in the interferometer, with $f_{\mathrm{Res}} = c_0/\Delta l$. In addition to this, the finite length of the gathered interferograms can be viewed as a multiplication of an

infinite interferogram $I(\delta l)$ with the boxcar function $D(\delta l)$ which sets all interferogram values outside the finite measured range $\pm\Delta l$ to zero. This results in the measured spectra $S_{\mathrm{meas}}(\nu)$ being a convolution of two functions, namely the actual light spectrum $\tilde{S}(\nu)$ and the Fourier transform of the boxcar function

$$f(\tilde{\nu}) \;=\; 2\Delta l\,\mathrm{sinc}\,(2\pi\tilde{\nu}\Delta l)\,, \tag{2.35}$$

the instrument line shape (ILS) of the spectrometer. The actual spectrum $\tilde{S}(\nu)$ has to be acquired via deconvolution or *apodization* of the measured spectrum $S_{\mathrm{meas}}(\nu)$ with this or a suitable other function, introducing ambivalence [72, 73]. Two different ILSs following Equation (2.35) are shown in Figure 2.17(a). In blue, an ILS for a spectrometer resolution matching the comb's repetition rate, $f_{\mathrm{Res}} = f_{\mathrm{Rep}}$, is shown, for the curve in red they differ by 25 %. For matching Δl, the ILS becomes zero at offset frequencies matching harmonics of the repetition rate and maximal at zero offset. This means that for the frequency comb with its discrete spectrum only one single comb tooth contributes to measured spectra at the tooths position. By contrast, the ILS with mismatched Δl is finite at all f_{Rep} harmonics, resulting in contributions from multiple comb teeth for any data point in the spectrum. This is shown in the subplot (b), where the simulated measurement of a very narrow absorption feature for the two spectrometers is shown. For the resolution-matched ILS the feature is exactly reproduced, while for the mismatched ILS it is surrounded by strong ripples towards the wings of the spectrum, decreasing the effective resolution. As outlined in reference [47], this resolution matching can be used to achieve *sub-nominal* resolution in measured spectra by interleaving measurements taken at different $f_{\mathrm{Rep}} = f_{\mathrm{Res}}$ [72, 73].

Spectral signal-to-noise ratio

As the Mid-IR frequency comb is affected by both intensity and phase noise as discussed above, a measured FTIR interferogram contains noise caused by these effects. The noise of the produced absorption spectra can be characterized by the SNR, relating the strength of an absorption feature with the standard deviation of the noise of the feature-less area surrounding them. The SNR estimated in the following is equal to the SNR of theoretical absorption features within the spectra with 100 % absorption. Measuring multiple noisy spectra and averaging them increases the SNR for the full measurement set. With increasing ensemble size N, the SNR of the averaged spectrum increases as

$$SNR_N \;=\; \sqrt{N} \times SNR_1, \tag{2.36}$$

with SNR_1 as the average SNR of a single spectrum [74]. By measuring this average SNR_1 for both the dither lock pump/seed delay stabilization and the modulation-free

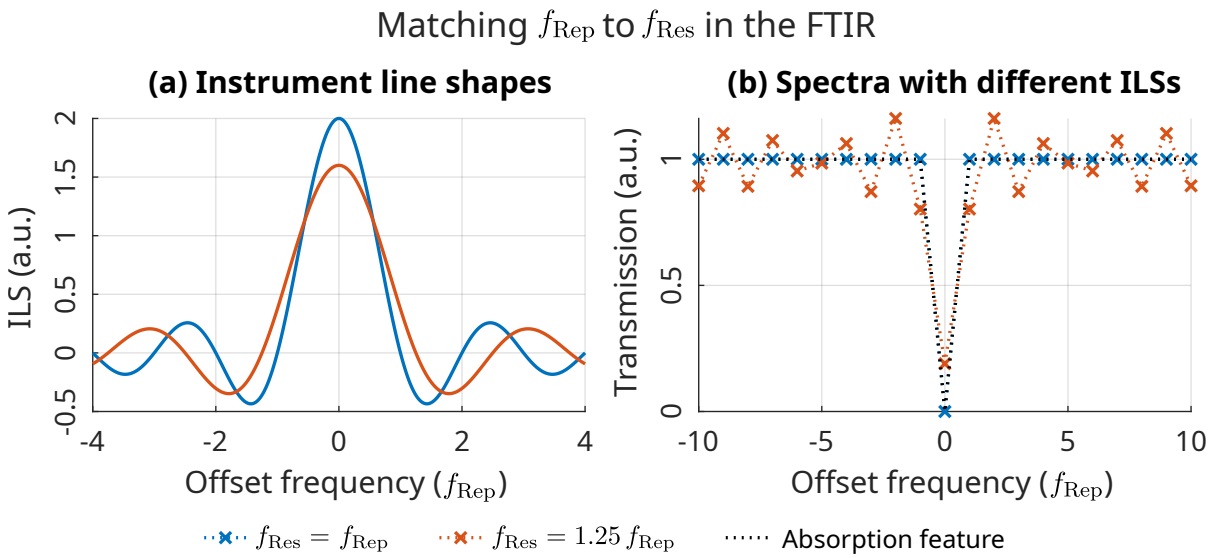

Figure 2.17: (a) Two calculated instrument line shapes following Equation (2.35) with different Δl, the one to match f_{Rep} becomes finite only for offset frequencies of zero. (b) Their influence on the measurement of a narrow absorption feature in black dotted line. The measurement with the ILS matching f_{Rep} reproduces this feature exactly, while the non-matching resolution shows ripples around it.

method shown later, it is possible to compare their long-term stability for spectroscopy. In reference [46] presenting the dither locking method, its long-term performance was characterized, showing a factor 1.7 improvement in spectral quality compared to an unlocked, free-running DFG setup. The same reference also outlines how this SNR is estimated and for comparability, the same calculations are used in this work. To estimate the SNR, an ensemble of different absorption-less spectra $S_n(\nu)$ of the Mid-IR frequency comb is measured with n as their running index. They are then divided into two subsets, $S_{n,\mathrm{even}}(\nu)$ and $S_{n,\mathrm{odd}}(\nu)$, contain the spectra of this ensemble with even/odd indices. These subsets are then averaged resulting in the average spectra $\overline{S}_{\mathrm{odd}}$ and $\overline{S}_{\mathrm{even}}$. From these average spectra, a quotient

$$Q = \frac{\overline{S}_{\mathrm{odd}}}{\overline{S}_{\mathrm{even}}} \tag{2.37}$$

is formed, which in the ideal case without noise and other drifts is exactly one. Within the FWHM of the spectra, the ratios standard deviation σ_Q is calculated, and the SNR becomes the reciprocal value of σ_Q,

$$SNR = \frac{1}{\sigma_Q}. \tag{2.38}$$

The SNR_1 factor from above can be understood as the average SNR calculated using two single spectra from the measurement ensemble.

To summarize this chapter, the main fundamental physics are presented which allow the generation and later detection of the Mid-IR frequency comb. These fundamentals start

with the generation of laser pulses in a mode-locked oscillator containing a saturable absorber, followed by a treatment of these pulses in both time and spectrum, which in turn leads to their description as an optical frequency comb as a function of two RF frequencies. However, these devices drift, leading to the comb structure washing out, therefore requiring measurement and stabilization of the constituting frequencies. Their measurement can involve different nonlinear optical effects based on the second-, third- or higher order nonlinear susceptibility of optical materials, and some of them relevant both for comb stabilization and later frequency conversion into the Mid-IR are detailed. Even after stabilization however some noise in both intensity and frequency or phase remains which is able to influence the spectrum of the comb. The effect of this noise on the comb is shown and for the phase noise it is explained how it relates to the optical line width of the frequency comb. Following this, the effect of modulation of the relative delay of the two frequency components involved in the DFG process for Mid-IR generation is calculated, resulting in the production of sidebands to the optical comb spectrum by these modulations. At the end of the chapter, then the detection of the Mid-IR comb is detailed in a FTIR spectrometer. Here, both the effective resolution of the spectrometer improved by the comb structure of the detected radiation and the SNR of the measured spectra is explained.

In the next chapter, the realized Mid-IR frequency comb spectroscopy setup from the source to its detection is shown. Additionally, a modulation-free RIN suppression method is presented and compared with a dither lock method implemented by previous works on the setup in a long-term spectroscopic setting.

3 Frequency comb laser and interferometrically stabilized Mid-IR source

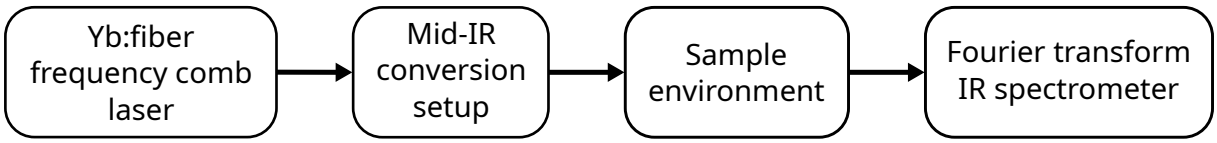

Figure 3.1: Schematic overview over the setup.

In this chapter, the Mid-IR frequency comb setup is described. First, a quick overview over the entire setup is given at the end of this introduction. This is followed by detailed descriptions and characterizations of the various elements the beam passes through on its way from generation to detection. One such element is a newly developed, interferometer-based technique to stabilize the Mid-IR source towards a point of minimal RIN in its output. The chapter will close with an in-depth characterization of this novel method. It will also be compared in terms of its long-term stability with the dither lock developed for previous works [46, 47], which as discussed in Section 2.3.4 introduces sidebands to the optical spectrum.

The Mid-IR comb setup is similar to the one described in [37] which was used in previous works as well in references [47, 75]. The first element is a comb-stabilized Yb:fiber laser. Using nonlinear processes, its output is then down-converted to provide coherent Mid-IR radiation following the principles described in Chapter 2. The generated radiation then passes through an (optional) sample into the FTIR spectrometer for detection. A simplified schematic of the Mid-IR frequency comb spectroscopy setup is shown in Figure 3.1.

3.1 Yb:fiber laser source

The starting point for all operation in this setup is a multi-branched Yb:fiber frequency comb laser centered at a wavelength of $\lambda_{\mathrm{Pump}} = 1060\,\mathrm{nm}$ with a repetition rate of $f_{\mathrm{Rep,1}} \approx 150\,\mathrm{MHz}$. Its optical setup is shown in Figure 3.2. At its main output branch, which drives the DFG stage, it provides pulses with an average power of 1.5 W and durations of 147 fs FWHM with flat spectral phase as measured and optimized with a frequency resolved optical gating (FROG) setup [76, 77]. The other two branches are

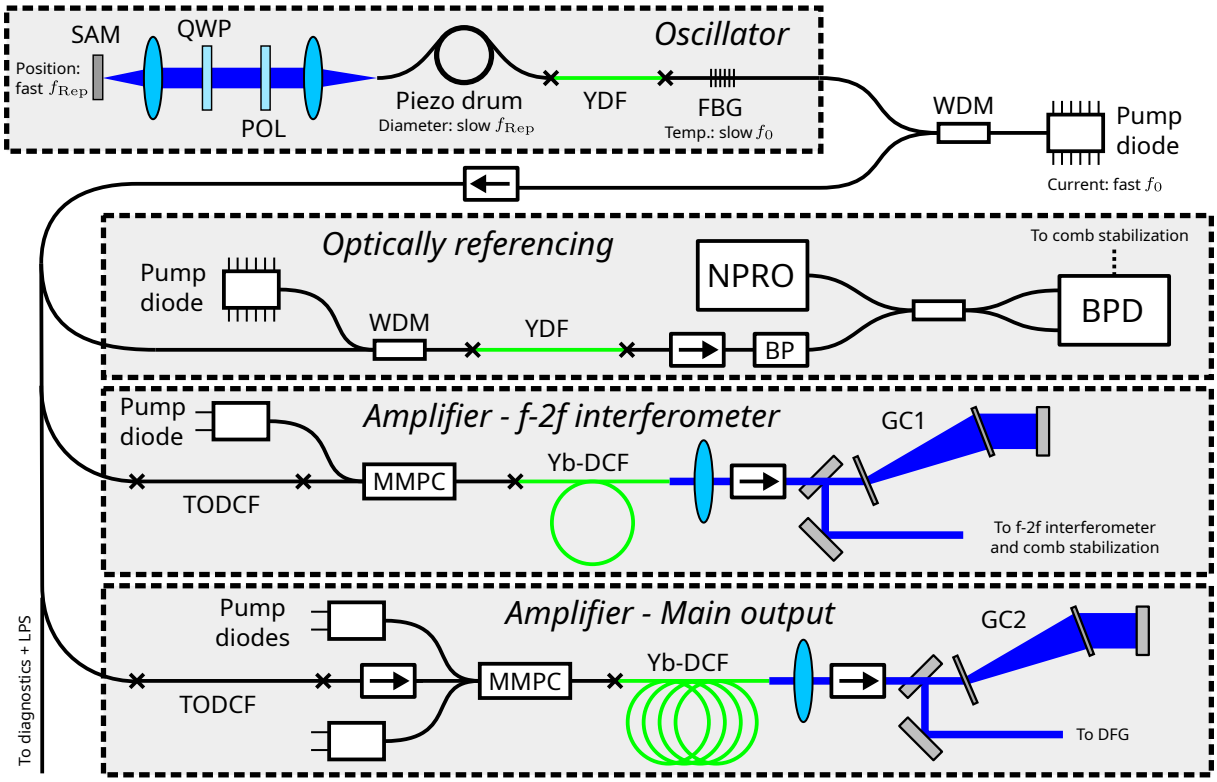

Figure 3.2: Overview over the laser setup. An oscillator with a linear cavity drives three amplifiers for different purposes. SAM: Saturable absorber mirror, QWP: Quarter wave plate, POL: Polarizer, YDF: Yb-doped fiber, FBG: Fiber Bragg grating, WDM: Wavelength division multiplexer, NPRO: Nd:YAG Nonplanar ring oscillator, BP: 1064 nm band-pass filter, BPD: Balanced photodiode TODCF: Third-order dispersion compensation fiber, MMPC: Multi-mode pump combiner, Yb-DCF: Yb-doped double cladding fiber, GC: Grating compressor, LPS: Laser protection system.

serving the comb stabilization mechanisms. One of these is used to interfere with a low-line width CW laser to stabilize the beat frequency $f_{\mathrm{Beat},1}$ between both lasers, while the other drives an f-$2f$ interferometer to measure and stabilize the comb's CEO frequency $f_{\mathrm{CEO},1}$. The comb's repetition rate $f_{\mathrm{Rep},1}$ is then stabilized via tuning the optical reference laser, following Equation (2.19) on page 15. The main parameters of the laser system are summarized in Table 3.1.

3.1.1 Laser setup

The laser itself consists of an oscillator whose output is split into three different amplifiers. One of these is providing the main output with the given output parameters, while the others serve to provide the optical signals used for the comb's frequency stabilization scheme. In addition to this, several diagnostics ports provide the opportunity to measure the oscillators output power and spectrum. Long-term and unsupervised operation is enabled by a fast photodiode connected to a laser protection system (LPS) based on a

Parameter	Value
Amplified spectrum	(1060 ± 30) nm
Output powers	1.5 W ± 0.1 %, Mid-IR branch 300 mW ± 0.1 %, f-2f branch
Pulse durations	147 fs, Mid-IR branch 120 fs, f-2f branch
Repetition rate	151.65 MHz
M^2 value	1.3

Table 3.1: Main parameters for the Yb:fiber laser driving the Mid-IR comb

field-programmable gate array (FPGA) and microcontrollers. This in-house developed LPS monitors the pulse train for irregularities and excess noise and shuts the amplifiers down in case of errors to protect the laser from damage during operation before it can occur.

Oscillator

The oscillator is based on a mode-locked linear cavity with both single-mode fiber and free-space parts and generates pulses with a repetition rate of $f_{\mathrm{Rep},1} = 151.65$ MHz. For mode-locking, a semiconductor saturable absorber mirror (SAM) is used which has a higher reflectivity for increased intensity, thus favoring pulsed operation. This SAM also serves as one of the two end mirrors of the cavity, the other being a fiber Bragg grating (FBG) in the fiber part of the oscillator. The active medium of the oscillator consists of a few cm of highly Yb-doped silica fiber [78]. It is pumped by a 976 nm pump diode with about 600 mW of output power, coupled in via a wavelength division multiplexer (WDM) after the FBG. A polarizer and a quarter-wave plate (QWP) in the free-space section together with a variable-pressure plate on the FBG control the output polarization.

For cavity length control the SAM is mounted on a small piezo ceramic, which itself is sitting on a lead-filled copper mount for acoustic dampening and enabling tuning by several Hz with bandwidths exceeding 100 kHz [79]. For slow, high-range cavity length control, parts of the oscillator fiber are spooled onto a piezo drum expanding with applied voltage. The CEO frequency $f_{\mathrm{CEO},1}$ is tuned via fast modulation of the oscillator pump diode's current and slow variation of the FBG's temperature. An optical isolator separates the oscillator from the amplifiers and protects it from back reflections.

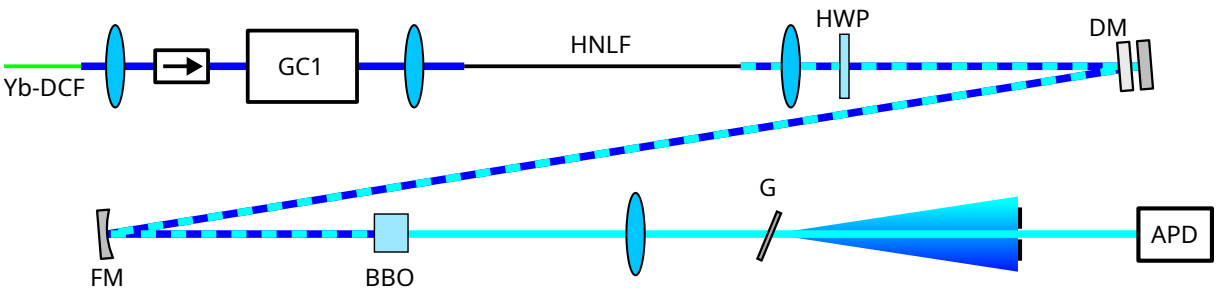

Figure 3.3: f-2f interferometer for $f_{\mathrm{CEO},1}$ stabilization of the frequency comb. The output of the amplifier is broadened to an octave-wide spectrum, followed by frequency-doubling the red-shifted spectrum to coincide with the blue-shifted part. After filtering out this overlapping spectrum, the $f_{\mathrm{CEO},1}$ frequency can be measured.

Optically referencing the frequency comb

After this isolator, the output of the oscillator is split into the different branches mentioned in the beginning of this section. The first amplified branch, labeled as "Optically referencing" inside Figure 3.2, provides light closely band-pass filtered around 1064 nm for performing a heterodyne beat with a Nd:YAG NPRO laser with 1 kHz of optical line width (Coherent Mephisto) [6, 51]. Both lasers are fiber-coupled to a 50:50 coupler serving as the beam splitter in an interferometer. The resulting beat frequency $f_{\mathrm{Beat},1}$ between both lasers is then detected with a fast balanced photodiode (BPD) for stabilization, see Section 3.1.2 for details.

Second amplifier and f-2f interferometer

The second branch is labeled with "Amplifier - f-2f interferometer" in Figure 3.2. The oscillator output first passes through a third-order dispersion compensation fiber (TODCF) and is then combined with the output of a single pump laser diode at 976 nm in a multimode pump combiner (MMPC). For increased environmental stability, the fibers after the TODCF are polarization-maintaining, while the sections before are implemented using single-mode fibers. After the MMPC, the laser light is amplified in a 2.5 m long Yb-doped double-cladding fiber (DCF) (Coherent Nufern PLMA-YDF-10/125-HI-8) to about 300 mW after compression. At the end of this fiber, the amplified light is coupled out and collimated with a lens with a focal length of $f = 15.29$ mm. It then passes an optical isolator for protection from back reflections into the amplifier. Finally, a grating compressor consisting of two 600 mm^{-1} gratings with 15 cm distance and a rooftop mirror compresses the laser pulses down to about 120 fs pulse duration.

The compressed pulses are then coupled into an f-2f interferometer for $f_{\mathrm{CEO},1}$ detection and subsequent stabilization [80]. This interferometer is shown schematically in Fig-

ure 3.3. In this interferometer, the light is coupled into a suspended core silica highly nonlinear fiber (HNLF) for octave-wide spectral broadening [81]. The long-wavelength part of the generated supercontinuum is then frequency-doubled in a BBO crystal to spectrally overlap with the short-wavelength spectrum. The light then passes a grating and is again fiber-coupled for spectral filtering before measurement with an avalanche photodiode (APD) to detect both the $f_{\mathrm{CEO},1}$ beat note and the repetition rate $f_{\mathrm{Rep},1}$. Its output is then split into the corresponding PLLs for stabilization as described in Section 3.1.2. As the HNLF is a dispersive medium, the temporal overlap between red- and blue-shifted parts of the spectrum needs to be re-established. This is done using a doubled mirror consisting of a dichroic mirror (DM) and a silver mirror. Here, the DM reflects the long-wavelength part of the spectrum while it transmits the shorter wavelengths. Tuning the distance between both mirrors then ensures temporal overlap. A half-wave plate (HWP) controlling the lights polarization is used after the HNLF in order to improve the $f_{\mathrm{CEO},1}$ beat notes signal.

Main amplifier driving the DFG source

The last amplifier branch, labeled "Amplifier - Main output" in Figure 3.2, provides light for the DFG source generating the Mid-IR radiation. It is very similar in design to the amplifier serving the f-$2f$ interferometer, using a longer Yb-DCF of around 3.5 m and a grating distance in the compressor of about 20 cm. An additional optical isolator before the MMPC improves the suppression of back reflections. This amplifiers average output power is about 1.5 W and its pulse duration is about 147 fs when optimized for the flattest spectral phase using FROG (Mesaphotonics FROGscan Ultra). The output spectrum is measured to be 1040 to 1070 nm with the same device. The FROG measurements are shown in Figure 3.4 with the time domain data shown in subplot (a) and the spectral domain shown in subplot (b).

3.1.2 Frequency comb locking electronics

The stabilization of the Yb:fiber laser driving the Mid-IR frequency comb has been described previously in references [47, 75] with no substantial changes for this work. A fundamental description of the basic principles for the stabilization of the frequency comb is given in Section 2.2.2. Here, the interplay of the three required frequency stabilization systems is explained by combining these explanations with the laser setup shown above in Section 3.1.1. This is followed by investigating their phase noise performance.

A simplified schematic of the stabilized laser system with the used phase-locked loops (PLLs) is shown in Figure 3.5. The Yb:fiber oscillator emits light which is amplified in

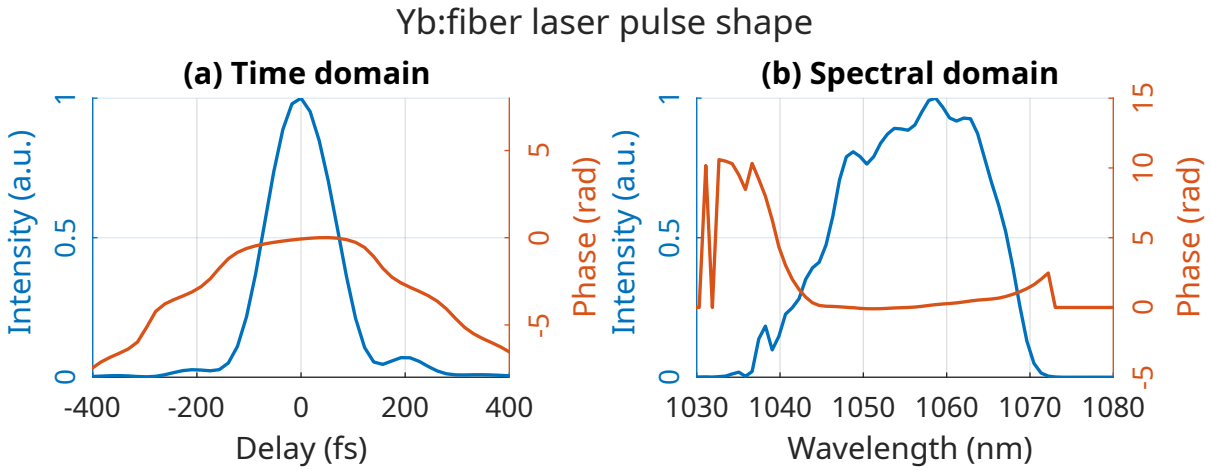

Figure 3.4: Laser pulses both in time (a) and spectral (b) domain as measured via a Mesaphotonics FROGscan Ultra device and with two different compressor settings either optimized for the shortest FWHM pulse durations or the flattest spectral phases.

different fiber amplifiers as shown above. One amplifier output is filtered and brought to interference with the NPRO reference laser, a BPD then measures their heterodyne beat frequency $f_{\mathrm{Beat},1}$. This frequency is used as an input for the first PLL, following the general setup shown in Figure 2.8 on page 17, to stabilize $f_{\mathrm{Beat},1}$ via a fast piezo cavity end mirror and a slower high-range piezo fiber drum.

A second amplifier is used to drive the f-$2f$ interferometer to generate output signals for both the CEO frequency $f_{\mathrm{CEO},1}$ and the comb's repetition rate $f_{\mathrm{Rep},1}$ which are fed into two distinct PLLs of similar design. The first controls the oscillators pump current (fast actuator) and the out-coupling FBG mirrors temperature (slow). The second loop controls the NPRO reference lasers cavity length via a fast piezo and a slow crystal temperature control.

All three described PLLs are based on in-house designed and built fast PID loop filters. The slow PID for the $f_{\mathrm{Beat},1}$ PLL is another in-house design, while the slow controls for both $f_{\mathrm{Rep},1}$ and $f_{\mathrm{CEO},1}$ use a commercial PID (Stanford Research Systems SIM960). A summary of all PLLs is given in Table 3.2.

Stabilized frequency	**Actuators**	**Set frequency (Hz)**
Carrier-envelope-offset frequency $f_{\mathrm{CEO},1}$	Fast: Oscillator pump Slow: FBG temperature	-122 000 000
Beat frequency with NPRO reference $f_{\mathrm{Beat},1}$	Fast: Piezo end mirror Slow: Piezo drum	-122 000 000
Comb repetition rate $f_{\mathrm{Rep},1}$	Fast: Piezo in NPRO cavity Slow: NPRO temperature	151 650 000

Table 3.2: Phase locked loops for the Mid-IR frequency comb

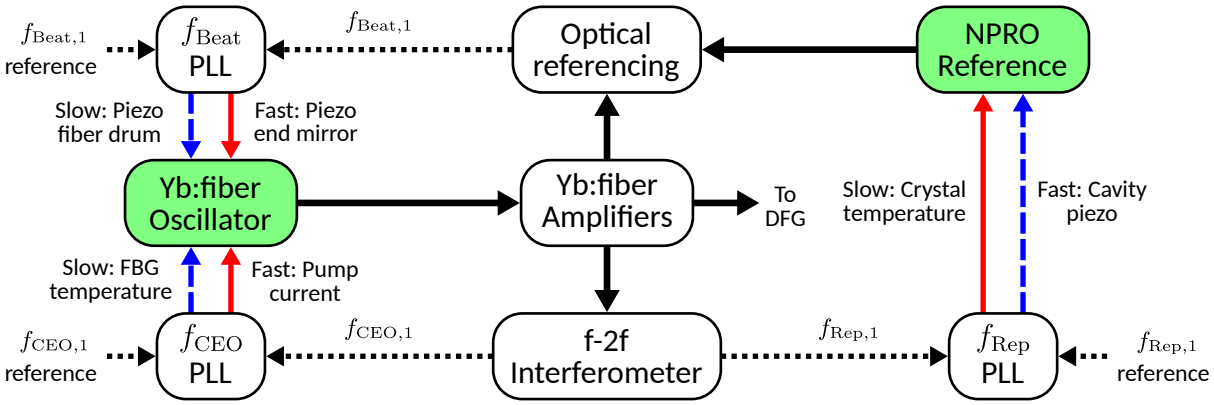

Figure 3.5: Setup schematic for the different intertwined phase-locked loop setups to stabilize the Yb:fiber frequency comb. Thick black lines are optical connections, thinner dotted lines show the measured frequencies and labeled solid-red/dashed-blue lines indicate fast and slow PLL outputs, respectively. The Yb:fiber oscillator and NPRO reference as the stabilized devices are highlighted in green.

Phase noise measurements

In this section, the phase noise of both $f_{\mathrm{Beat},1}$ and $f_{\mathrm{CEO},1}$ is characterized [65]. For this, the frequency to stabilize is coupled out from the PLL, amplified and then measured with a signal source analyzer (SSA) (Agilent E5052B) which is capable of characterizing a variety of properties of RF signals. In Figure 3.6, the measured phase noise for both $f_{\mathrm{Beat},1}$ (solid lines) and $f_{\mathrm{CEO},1}$ (dashed lines) is plotted as a function of the offset frequency, logarithmically from 1 Hz to 10 MHz. Both curves were correlated between four single measurements each. On the left axis, the measured single-sideband power spectral density (SSB PSD) relative to the frequencies carrier power is depicted. Both phase noise PSDs show a servo-bump around 30 kHz denoting the bandwidth of the fast PLLs. The right axis shows the integrated phase noise following Equation (2.24) on page 24 as a function of the offset frequency, starting from a maximum frequency of $f_2 = 10\,\mathrm{MHz}$. This value gives the phase noises total contribution (RMS) for measurement durations defined by the inverse of the lower frequency bound f_1 of the integration. For these measurements, the total integrated phase noise from 1 Hz to 10 MHz is 353.2 mrad for the heterodyne beat frequency $f_{\mathrm{Beat},1}$ and 335.52 mrad for the CEO frequency $f_{\mathrm{CEO},1}$, respectively. Both curves show no significant increase below the servo bumps' frequencies at 30 kHz.

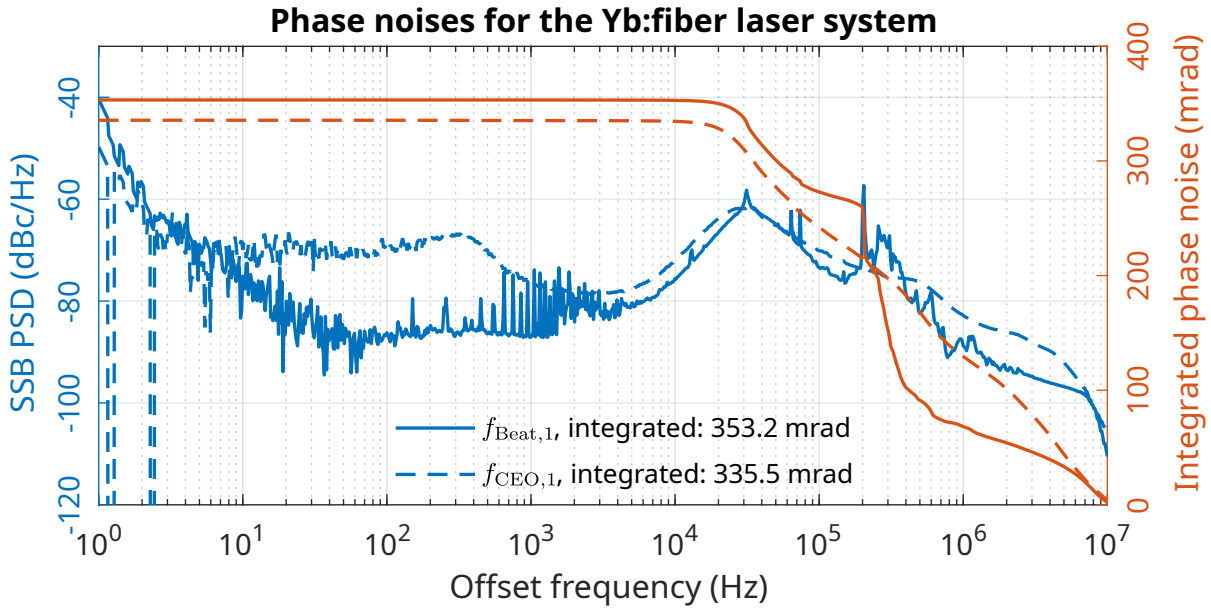

Figure 3.6: Plot of the phase noises for the $f_{\mathrm{CEO},1}$ and $f_{\mathrm{Beat},1}$ locking systems on the Yb:fiber laser, measured with an SSA. On the left axis (blue color) the measured single-sideband power spectral density is shown. The right axis shows the integrated phase noise from these PSDs. Both locks show a similar performance.

3.2 Mid-IR source

The setup converting the output of this Yb:fiber laser down into the Mid-IR spectrum was first described in [47] and has been extended and improved during the course of this work. It is shown in Figure 3.7 and it is based on the DFG of two collinear pump and seed pulses with the seed being spectrally shifted as discussed in Section 2.2.1. The pump beam is being routed via a piezo delay stage controllable via an electric voltage. The seed beam is first coupled into a HNLF for wavelength-tunable Raman soliton self-frequency shift (SSFS) down to suitable wavelengths of around 1.4 to 1.6 µm. This seed generation allows Mid-IR central wavelengths tunable between 3 to 5.2 µm [46]. Both beam paths are recombined and focused into a nonlinear crystal for the DFG process. The source parameters are summarized in Table 3.3.

Parameter	**Value**
Tunability	3 to 5.2 µm [46]
Spectral bandwidth	≈150 nm
Max. output power	20 mW at 3.84 µm and 1.5 W total input
M^2 value	<3.5
Beam diameter	≈3 mm

Table 3.3: Main parameters for the Mid-IR source

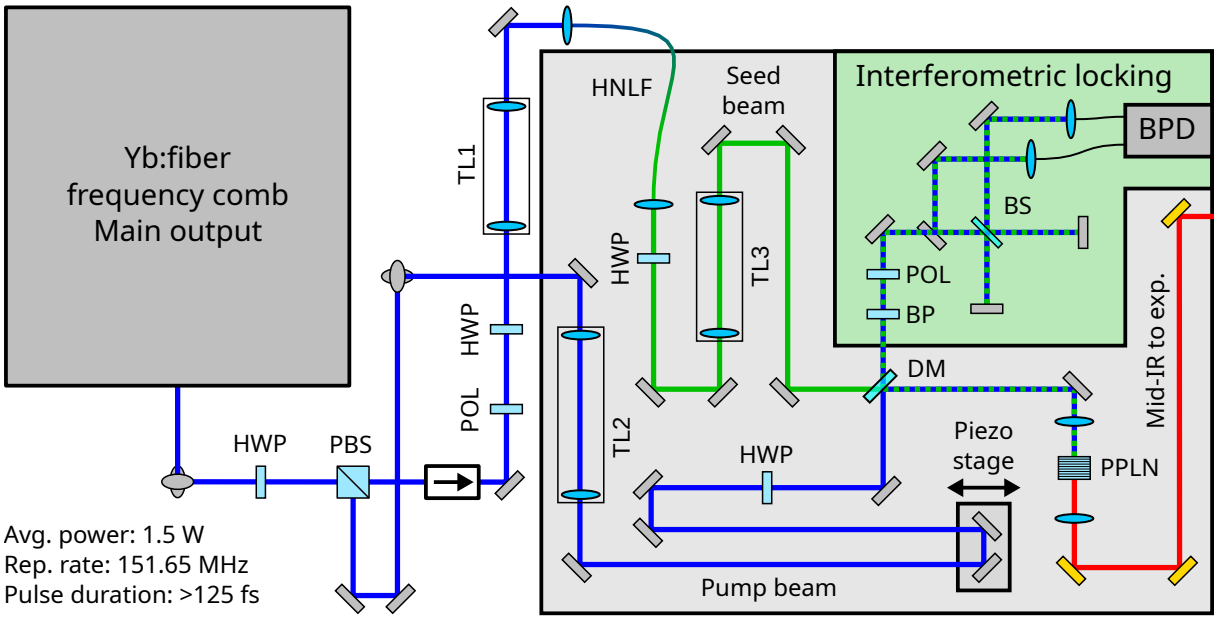

Figure 3.7: Detailed overview over the optical setup for the DFG source.

It was found previously that the output of the source shows a sudden drop in relative intensity noise (RIN) of about 30 dB in a 20 fs wide region around a pump/seed delay Δt close to perfect overlap of the two beams. For long-term stable RIN suppression, a dither locking method was implemented and used [46]. However, an unexpected broadening of measured absorption lines was found with setups using this method [40, 41, 47, 60], aided by the sideband generation discussed in Section 2.3.4. Here, a novel locking scheme is introduced which circumvents this by directly locking Δt to an interference fringe in the (residual) λ_{Pump} radiation in both beams.

3.2.1 Optical setup

A detailed overview over the Mid-IR source is shown in Figure 3.7. The output of the Yb:fiber laser (1.5 W average power, 147 fs pulse duration) is split in two parts, pump and seed, via a HWP followed by a polarizing beam splitter (PBS). This combination allows a continuous selection of the splitting ratio between both output beams by turning the HWP. The seed beam is sent through an optical isolator and a polarization filter, followed by another HWP. It is then coupled into a HNLF of the same type as in the f-2f interferometer described in Section 3.1.1 of 31 cm length. Before the HNLF, a lens telescope serves to match the output mode of the fiber amplifier to the mode of the HNLF. This HNLF is used for the Raman SSFS to generate the seed input for the DFG. Its output is then routed to the DM (transmitting the seed beam) used to recombine pump and seed.

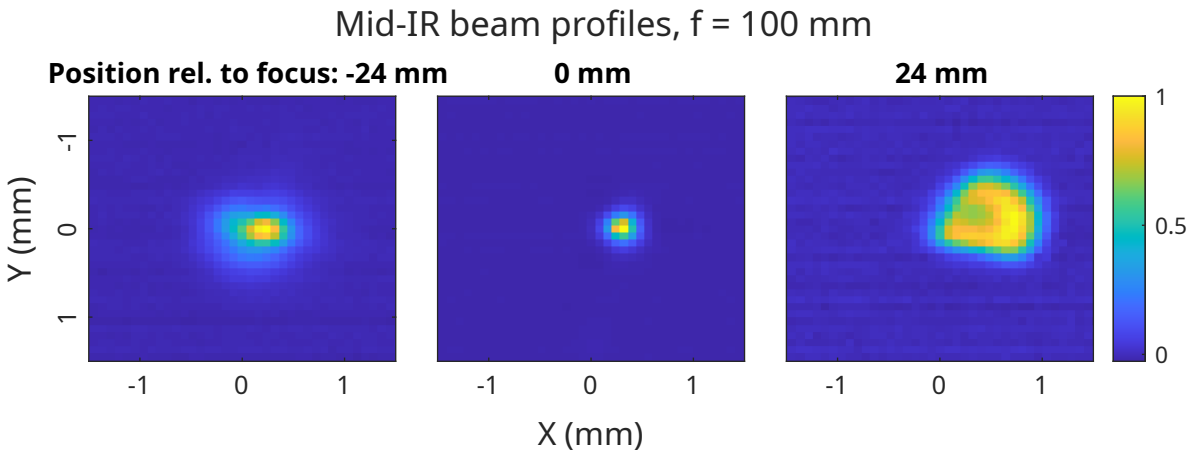

Figure 3.8: Beam profiles of the Mid-IR source as measured with an Ophir Optronics Pyrocam IIIHR and a $f = 100\,\text{mm}$ lens, showing a low-quality beam.

The pump beam is routed via a piezo-electric delay stage tuning Δt and then routed to the DM, where the majority is reflected to be collinear with the seed. Using a lens with $f = 50\,\text{mm}$, both beams are focused into a periodically poled magnesium-oxide doped lithium niobate (MgO:$LiNbO_3$) (PPLN) crystal with 16 discrete quasi-phase matching (QPM) grating periods (24.06 to 36.95 µm) inside a small oven, providing temperatures of up to 180 °C (Covesion MSHG3100-0.5-3 + PV10) to change the crystals phase matching conditions. The sources central wavelength can be tuned via changing both the grating period and the crystal temperature, followed by changing the incoupling ratio into the HNLF to shift the seed's central wavelength accordingly. These factors allow a tunability of the Mid-IR beam's central wavelength between 3 to 5.2 µm [46, 47]. Its tunability towards lower wavelengths is limited by the achievable Raman shift, while towards higher wavelengths the PPLN crystal becomes intransparent. In both arms, additional mode-matching telescopes before the DM ensure that both beams have the same focal position and size inside the PPLN crystal. Their polarization is matched with additional HWPs before the DM. The optical setup for the interferometric locking described later in Section 3.2.3 is shown as well inside the green box in Figure 3.7.

The generated Mid-IR radiation with up to 20 mW of optical power at 3.84 µm is collimated using a lens with $f = 25.4\,\text{mm}$, spectrally filtered using a Ge wedged window and then sent towards diagnostics or experiments. At an input power of 1.5 W, this output power amounts to an efficiency of about 1.3 %. For the beam, the M^2 value indicating its quality (with $M^2 = 1$ indicating a perfect Gaussian beam), has been measured to be quite high at $M^2 < 3.5$ with a movable beam profiler (Ophir Optronics Pyrocam IIIHR, pixel pitch 80 µm) and a lens with $f = 100\,\text{mm}$. The beam diameter before the lens is about 3 mm, after focusing the spot size is estimated to be about 200 µm which is only a few pixels on the detector. Some beam profiles around the focus measured with this setup are shown in Figure 3.8, clearly showing that the Mid-IR beam exhibits a strongly

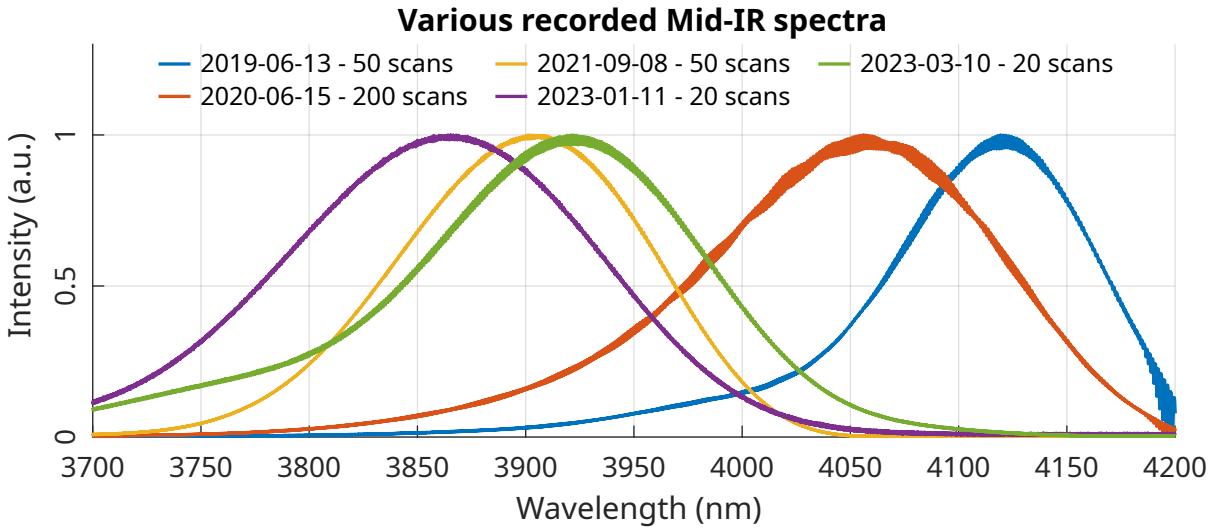

Figure 3.9: Some samples of averaged (number given in the legend) and normalized Mid-IR spectra recorded from the DFG source, showing their evolution over time.

distorted profile especially after the lenses focus. This necessitates spatial filtering by apertures before the FTIR spectrometer for measuring high quality Mid-IR spectra. This filtering on one hand reduces the available Mid-IR power significantly. On the other hand the spectrometer detectors are highly sensitive to the Mid-IR radiation and as such the spatial filtering removes the need for neutral density filters.

Some sampled Mid-IR spectra recorded over the course of this work are depicted in Figure 3.9. These spectra show how different source parameters influenced the appearance of these spectra. Earlier spectra for example were recorded in preparation for investigations on NH_3 described in references [14, 48] and are therefore centered around 4.1 µm. These spectra show strong modulations caused by plane-parallel Ge windows in the Mid-IR beam paths acting as *etalon* filters. Their period length of 4 cm is caused by the windows thickness of 5 mm and their refractive index of 4.02 [82]. In the given references, these were corrected numerically by fast Fourier transform (FFT) filtering. For later measurements, these windows were replaced by wedged windows with 0.5° wedge angle which do not show this effect. Thus, spectra recorded later around 3.9 µm in anticipation of the heterodyne beat experiments described in Chapter 4 are significantly less modulated.

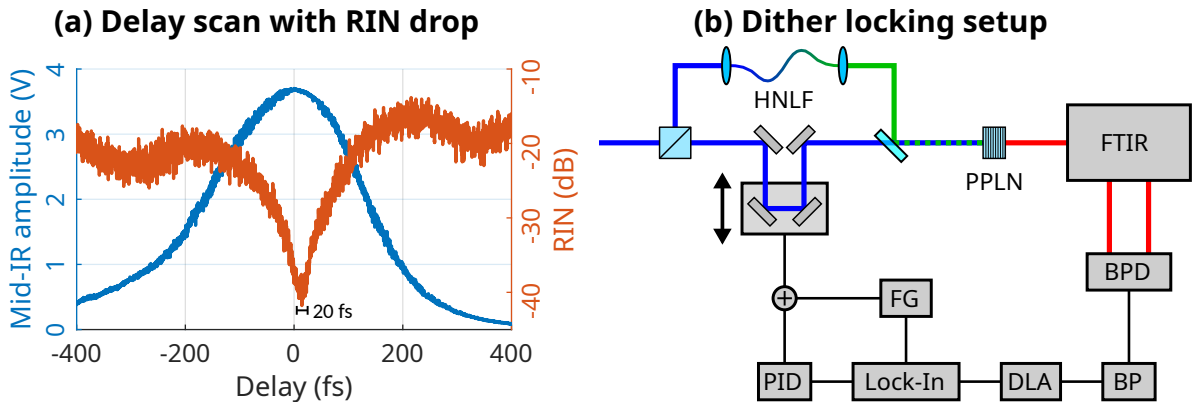

Figure 3.10: (a) Delay scan in the DFG source with both the Mid-IR output and its RIN visible. Near $\Delta t = 0$, a drop in RIN of above 20 dB is observed in a 20 fs wide region. (b) Dither locking mechanism to stabilize to this minimum. The pump/seed delay Δt is modulated by a small sinusoidal signal. Using the output from the FTIR's balanced photodiodes, the RIN is measured via a band-pass filter and a demodulating logarithmic amplifier. From this, a lock-in amplifier synchronized to the modulation generates an error signal for a PID controller. Its output is then added to the modulation input to drive the average stage position towards minimal output noise.

3.2.2 Intensity noise in the DFG stage

As stated in Section 2.3.1, real laser systems suffer from environmental influences such as vibrations or electronic noise in the driving sources, leading to intensity noise. For the Mid-IR frequency comb, a DFG stage serves to convert such a Near-IR laser into the Mid-IR via nonlinear effects. These effects can amplify intensity noise. As one example, the nonlinear polarization of the SHG process is described by Equation (2.6) on page 9 and proportional to the square of the input electrical field E. As such, a change in the electrical field E of only 0.1 % leads to a change in the nonlinear polarization of about 0.2 %, doubling the intensity noise in the output fields. In the DFG setup requiring both second- and third-order nonlinearities (the actual DFG process and Raman SSFS for the seeds spectral shifting), this aspect thus becomes highly important.

Previously it was found that the Mid-IR source exhibits a strong drop in RIN of 20 to 30 dB at small pump/seed delays Δt in a 20 fs wide region around $\Delta t = 0$ [46]. A delay scan showing this phenomenon with both Mid-IR power and its RIN is shown in Figure 3.10(a), using the same methods as in [46, 47]. In this plot, the Mid-IR RIN and power are measured using one of the BPDs of the FTIR setup used for spectroscopy, with the FTIRs delay stage being stationary. The average Mid-IR power is determined from the photodiodes signal via a low-pass filter at 10 Hz. For the noise signal, a band-pass filter selects the frequency range 1 to 30 kHz. A demodulating logarithmic amplifier (DLA) demodulates this filtered signal and amplifies it such that its output voltage is proportional to the logarithm of the noise integrated over the band-pass filters frequency

range. From this, the RIN as a function of Δt is calculated by dividing the Mid-IR power by this noise signal.

For long-term stable operation suitable for hour-long spectroscopic measurements near this noise minimum, a stabilization scheme based on dithering Δt constantly was implemented [46]. A basic schematic for this delay locking setup is shown in Figure 3.10(b). The pump/seed delay stage is modulated with a small sinusoidal signal with a frequency of $f_{\mathrm{Mod}} = 160\,\mathrm{Hz}$ and an amplitude of $U_{\mathrm{Mod}} = 0.05\,\mathrm{V}$ via a function generator. The Mid-IR noise is then measured as described above. The DLAs output is fed into a lock-in amplifier (Stanford Research Systems SR530) synchronized to the delay modulations function generator. This device multiplies its signal input with the reference oscillation from the function generator delayed by a set phase ϕ and integrates the result over time to produce a DC output signal [83]. Due to the integration, only frequency components in the signal near f_{Mod} are contributing to this output, enabling it to measure the Mid-IRs noise modulation even at low SNRs. With the lock-in amplifiers reference phase delay ϕ set to $\pi/2$, the output of the lock-in amplifier approximates the first derivative of the noise modulation with a zero-crossing between falling and rising slopes. Its output is used to provide a PID loop filter with an error signal input, and the PIDs output is summed with the modulation to drive the Δt delay stage to the position with the lowest Mid-IR RIN. Similar techniques based on the same principles are used for the implementation of optical PLLs to stabilize the optical frequency of lasers directly to external references such as other lasers or atomic resonances [84, 85].

3.2.3 Interferometric locking for noise suppression

As mentioned in the beginning of this section, different experiments reported an unexpected line broadening in the measured molecular spectra of several MHz. These experiments all employed a dither lock modulating the pump/seed delay Δt constantly [40, 41, 47, 60], which does generate sidebands as shown in Section 2.3.4. To eliminate these sidebands, a novel dither-free locking scheme was developed. This mechanism is schematically shown in Figure 3.11(a), and the full optical setup is included in Figure 3.7 on page 41 inside the green box. It is based on the interference of residual 1060 nm pump radiation on the so-far unused fourth port of the DM used to recombine pump and seed beams before the nonlinear crystal. While the mirror is highly reflective for the pump beam, a small amount of about 0.15 % is still transmitted. This amount enables interference with the residual non-broadened light in the seed beam after filtering in both polarization and spectrum. Using this method locks the OPD between both beam paths to a sub-wavelength range, which is much lower than the 20 fs of required precision to stay in the low-noise region shown in Figure 3.10(a). This method was first described

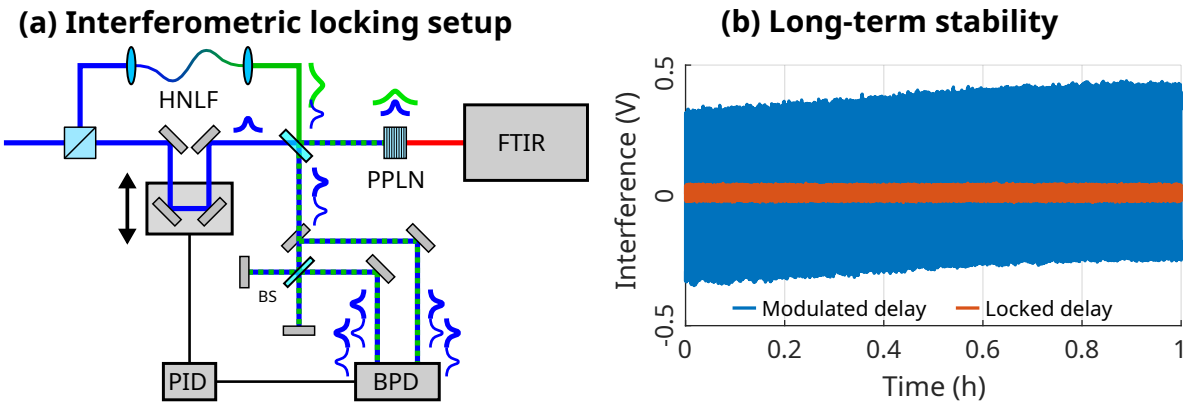

Figure 3.11: (a) Setup for the new interferometric locking method. Along the beampath, small pulse symbols show how the interferometer overlaps the 1060 nm pulses at the same time as the pump and seed in the PPLN crystal. (b) Two measurements showing the stability of the optical setup over an hour. In the blue plot, the pump/seed delay Δt was modulated with a 160 Hz sine wave of 1 V amplitude such that the interferences amplitude and centering are visible. Some drifting is visible here. In the red curve, the setup was locked, showing no slips occuring over the measurement duration.

in [70]. The next sections are following up on this publication with more details on the characterization of this setup in particular.

The HNLF induces group delay dispersion between the non-broadened light at the pump wavelength and the red-shifted solitons used to seed the DFG process. This causes a relative delay between both parts of the seed beam, which is shown along the way after the HNLF in Figure 3.11(a) using small pulse symbols, with the residual pump in thin blue lines, and the seed solitons in a thicker green. For high Mid-IR output, these solitons and the pump beam pulses shown in a thicker blue line need to fully overlap inside the PPLN. The delay between both parts of the seed beam thus also causes a relative delay between the two 1060 nm pulses. To correct this, a small Michelson-type interferometer is set up on the fourth port of the DM. This interferometer produces pulse copies on its output spaced such that their OPD counteracts the HNLF-induced delay to make them interfere on its output. Their interference is detected with the first input of a fiber-coupled BPD. The interferometer is slightly mis-aligned such that a mirror can pick-off the reflection from the interferometer and couple it into the BPDs second, negative input. This makes the detection insensitive to laser power fluctuations as they affect both inputs equally and cancel out. Its output is thus only sensitive to the change in OPD between both arms of the DFG setup and can be fed into a PID loop filter, driving the Δt delay stage directly.

In Figure 3.11(b), the stability of the interferometers output over an hour of time is shown, which is a typical duration for spectroscopic measurements. In this plot, both a strongly modulated pump/seed delay Δt (blue curve) and a locked Δt (red) are shown. For the modulated case, a frequency of 160 Hz with an amplitude of 1 V and an offset of

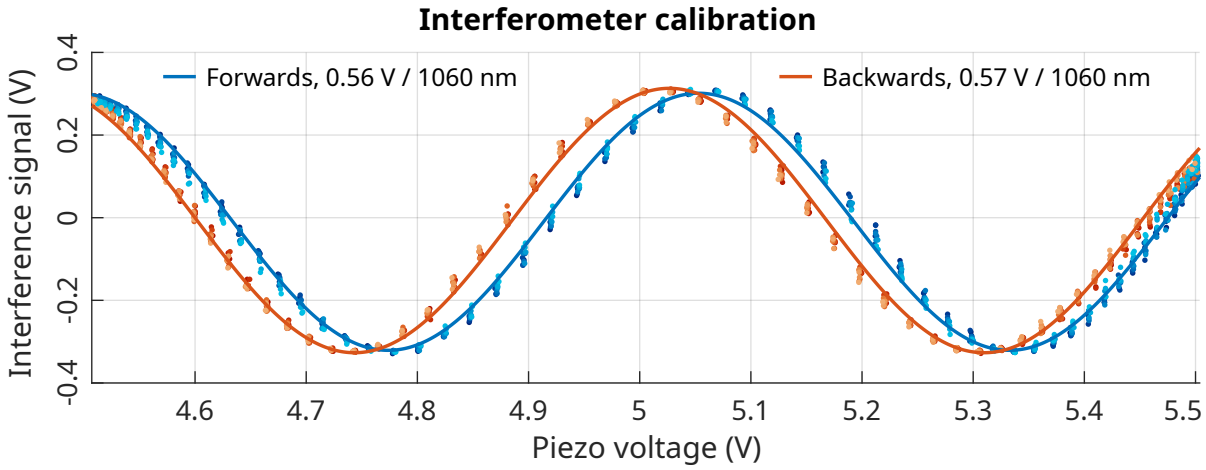

Figure 3.12: Calibration of the locking interferometer. The first 50 scans (both forwards and backwards) from the modulated data in Figure 3.11(b) were plotted as a function of the piezo voltage and fitted with a sine function to measure the average piezo voltage to move one light period λ_{Pump}, which is around 0.56 V in both cases. For both scan directions, a change in color saturation denotes different scans.

5 V was used to provide an initially well-centered interference signal with an amplitude of ±0.3 V. This setting is typically used for the alignment of the setup. Over time, a slight drift is visible due to optics settling down over the course of the measurement, following initial alignment of the setup to improve the signal's amplitude and centering around zero. Towards the end after around 0.8 h, the setup has stabilized. After this measurement the signal was re-centered and locked to measure the locked curve, showing a much smaller signal amplitude with no visible drifts or other changes. A small offset from zero in the locked interferometer signal is caused by the PID controller itself. It is important to note that no phase slips were observed in the locked signal. Also, the drift of the modulated signal is small enough for the locked signal to stay within its envelope for the entire 1 h of measurement duration. This means that the setup could have been locked for this time frame without fault. These results confirm that the method is able to keep the OPD highly stable for long-term operation.

Characterization of the locking setup

For the characterization of the setups exact long-term stability, the measured data from Figure 3.11(b) is examined in more detail. While these measurements were running, the piezo voltage was recorded at the same time as the interferometers output signal at a sample rate of 5 kHz. This allows to plot interference signal as a function of the piezo voltage and to calculate the required piezo voltage to travel one single pump wavelength of $\lambda_{\mathrm{Pump}} = 1060\,\mathrm{nm}$. This is shown for the modulated signal in Figure 3.12. In this plot, the first 50 delay scans of the measurement are shown. To correct for the apparent

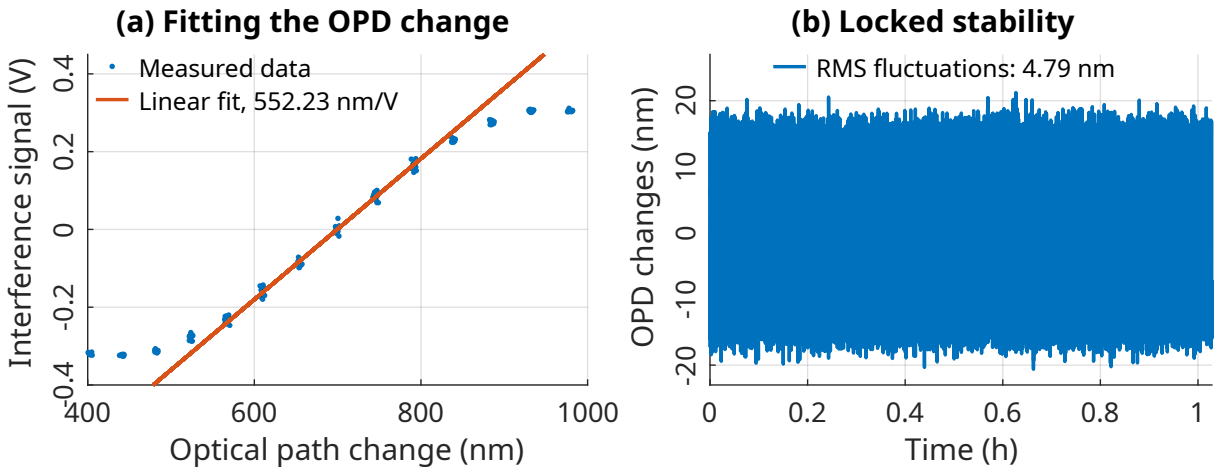

Figure 3.13: (a) The calibrated forward scans of the data from Figure 3.11(b) and Figure 3.12 are fitted as a linear function for smaller deviations from zero. The reciprocal value of its slope shows how much the OPD changes with small fluctuations in the interferometers output. In (b) this factor is applied to the locked data in Figure 3.11(b) to calculate the quality of the performed locking, whichs is better than 5 nm (RMS) over the chosen sample rate of 5 kHz for this measurement.

slip between both travel directions, the shown and fitted data is split between them. For the blue points, labeled "Forwards" in the plots legend, the piezo voltage increases with time, while for the data in red, labeled "Backwards", it decreases. The sinusoidal delay modulation is visible in the data via the changing density of the plot points towards the ends of the piezo voltage's range, and the different scans are indicated by a change in the corresponding data points brightness.

The data shows a sinusoidal motion which can be fitted as such with a function of the form

$$U_{\mathrm{Out}}(U_{\mathrm{Piezo}}) = U_{\mathrm{Ampl.}} \times \cos\left(\frac{2\pi \times U_{\mathrm{Piezo}}}{U_{\mathrm{Period}}} + \psi\right) + U_{\mathrm{Off.}}, \tag{3.1}$$

with $U_{\mathrm{Piezo/Out}}$ being the piezo input and interferometer output voltages, $U_{\mathrm{Ampl./Off.}}$ and ψ the oscillations amplitude, offset from zero and offset phase, respectively, and U_{Period} the wanted period length. Fitting the data with this function results in the required voltage $U_{\mathrm{Period}} \approx 0.56\,\mathrm{V}$ to travel one pump wavelength for both travel directions. This calibration factor allows to convert the piezo voltage on the x axis into the actual travel length, which was applied in Figure 3.13(a). Here, the calibrated x axis is set to zero for a piezo voltage of $U_{\mathrm{piezo}} = 4.5\,\mathrm{V}$ to the left of the plotted range. This graph shows the one full upwards slope of the data shown in Figure 3.12 for the backwards travel direction. The center part of this slope between 600 to 800 nm (or $\pm 0.2\,\mathrm{V}$ in terms of the interferometer output) signal is fitted with a linear curve. In this range, the measured data agrees well with the small-angle approximation $\sin(x) \approx x$. The reciprocal slope of the linear fit of around 552 nm/V represents the amount of travel per output voltage of the interferometer in this approximation.

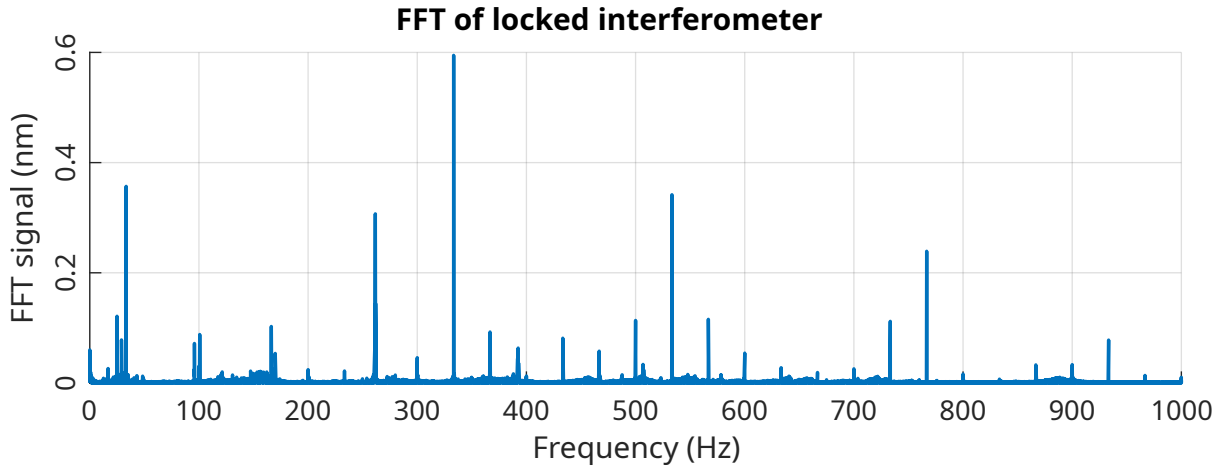

Figure 3.14: Fourier transform of the output of the locked interferometer as in Figures 3.11 to 3.13. The strongest noise spikes appear around 333, 33, 533, 261 and 767 Hz with smaller ones inbetween.

Multiplying this value with the interferometer output voltages in the locked measurement in Figure 3.11(b) results in the OPD stability of this setup. The data scaled using this factor is shown in Figure 3.13(b), which shows that the OPD is fluctuating at most by ±20 nm, or about 4.79 nm RMS within the 5 kHz sample rate for this experiment over its one-hour duration. This means that the lock stabilizes the OPD to less than $\lambda_{\mathrm{Pump}}/200$ of residual fluctuations. In terms of the relative delay $\Delta t_{\mathrm{RMS}} < 16$ as are measured, which is three orders of magnitude better than the required 20 fs. This should result in excellent noise suppression, which will be shown in Section 3.4.

Since the locked signal contains noise, another interesting aspect for characterization is its frequency composition. Thus, a FFT is performed on the locked signal from Figure 3.13(b), with the results of this operation shown in Figure 3.14. This shows that the noise signal mostly consists of discrete noise spikes at certain frequencies, of which the ones at 333, 33, 533, 261 and 767 Hz (ordered by their strength) are the most prominent. Later in Chapter 4, this measurement will be repeated to coincide with the phase noise measurements for the DFG source beaten with a second frequency comb at 2 µm, showing that some of these spikes appear in both types of measurements and thus are caused by mechanical resonances in the optical setup.

3.3 Fourier transform spectrometer for Mid-IR detection

The generated Mid-IR light passes through a sample environment filled with the material to investigate. Formerly, a room-temperature gas cell filled with CO and NH_3 at varying pressures and a well-known length was used to measure absorption line positions and intensities with high precision [14, 47, 48]. In [48], chapter 6, a possible improvement of

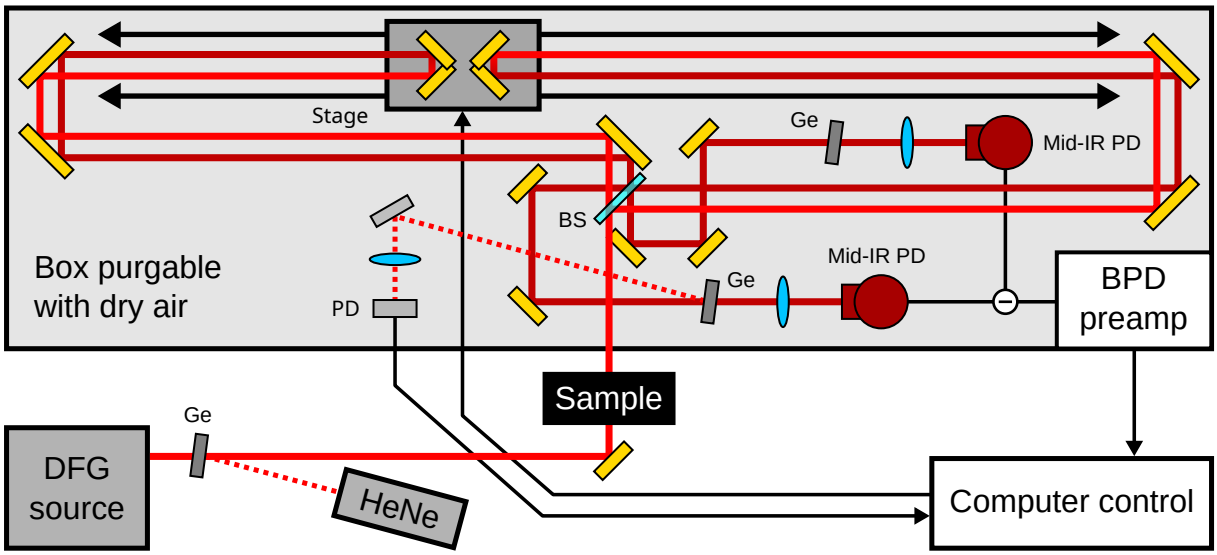

Figure 3.15: Optical setup for the home-built Fourier transform infrared spectrometer. The output of the Mid-IR source passes through a germanium wedge for overlapping with a frequency-stabilized HeNe laser. The two beams are coupled into a scanned Michelson-type interferometer. Its Mid-IR outputs are brought onto balanced photodetectors, while for the HeNe beam one single detector is used.

the cell design is proposed, implementing both a LN_2 cryostat and a significant increase in interaction length of the light with NH_3 molecules up to 10 m. This enables measurements at lower pressures and temperatures, resulting in less broadening effects and more molecules in their ground state.

To explore these interesting phenomena however, the transmitting light's spectrum has to be resolved at a high enough resolution. In this work this is achieved with a FTIR spectrometer consisting of a Michelson interferometer with a possible introduced OPD of up to $\Delta l = 4\,\mathrm{m}$, resulting in a nominal resolution of close to $f_{\mathrm{Res}} = c_0/\Delta l = 75\,\mathrm{MHz}$. As discussed in Section 2.3.5, the finite length of the interferograms results in a finite ILS described by Equation (2.35) on page 30, which leads to bleeding between adjacent data points. This lowers the FTIRs effective resolution and introduces some ambivalence in the measured spectra from the required deconvolution (or *apodization*) with a suitable ILS. In this setup, the spectrometer is run at a nominal resolution exactly matching the comb's repetition rate $f_{\mathrm{Res}} = f_{\mathrm{Rep},1} \approx 150\,\mathrm{MHz}$. This fully removes contributions from adjacent spectral data points and possibly allows for sub-nominal resolutions by measuring and interleaving series of spectra at different repetition rates and matching spectrometer resolutions. The spectrometer and its data evaluation process have been described in detail in reference [47] and were not changed in any significant way for this work.

3.3.1 Optical setup

The optical setup for the FTIR is shown in Figure 3.15. It is placed inside an enclosure designed to be purgeable with dry air to reduce absorption by atmospheric CO_2 and water vapour. The light entering this enclosure is provided by the DFG source described in Section 3.2. It is first filtered through a Ge wedged window (0.5°) to remove residual pump and seed radiation. This window is also used to overlap the Mid-IR beam collinearly with a frequency-stabilized HeNe laser (Sion Meßtechnik SL-04) at $\lambda_{\mathrm{Ref}} = 632.991\,234\,\mathrm{nm}$ with an absolute frequency stability of $\pm 1\,\mathrm{MHz/h}$ (or a relative stability of 2×10^{-9}). This HeNe laser is used both for the alignment of the FTIR as it is safely visible even through laser safety goggles and its calibration due to its well-known frequency. The combined beam then passes the sample environment and into the enclosure.

Inside the enclosure, the beam is split 50:50 into both arms of the interferometer. In both arms, gold mirrors are used to fold the beam and direct it towards the cubed retro-reflectors mounted on a 1 m long linear stage controlled by the data acquisition and control system (DAQ) (Aerotech ACT115DL) scanning at 125 mm/s for typical measurements. The used gold coating on the mirrors provides a broad reflection bandwidth from 600 nm (close to the HeNe calibration laser) up to the desired Mid-IR wavelengths and beyond. The moving retro-reflectors are used to introduce the OPD needed to reach the $f_{\mathrm{Rep},1}$-matched resolution of the FTIR. By moving both interferometer arms at the same time (one being shortened, one being lengthened), the OPD is changed four times the stage movement enabling a maximum possible nominal resolution of 75 MHz.

The reflected beam is shifted by 2.5 cm compared to the incoming beam to enable picking up both the transmission and the reflection of the returning beam on the beam splitter. Similar to the locking interferometer described in Section 3.2.3 on page 45 this enables balanced detection of both interferometer output beams after recombination for lower susceptibility to intensity fluctuations and thus increased SNR in the measured interferograms. On both outputs, the beams are first filtered again with Ge wedges to separate the calibration HeNe and Mid-IR beams. Lenses then focus each Mid-IR beam into a LN_2 cooled InSb photodetector (InfraRed Associates IS-0.5), which are connected antiparallel to form a BPD. The signal from this BPD is pre-amplified and filtered to provide the interferogram signal to one input channel of the data acquisition and control system (DAQ). The preamp also provides other filtered outputs to generate both Mid-IR power and noise signals as used in Section 3.2.2. The reflected calibration beam from one of the arms is focused into a Si APD (Thorlabs APD120A2). Here, no balanced detection is required as the noise is not critical. Its output is fed into the second channel of the DAQ.

3.3.2 Data acquisition and evaluation

The DAQ consists of a computer with a 2-channel AC-coupled high-speed analogue-to-digital conversion (ADC) card (National Instruments PCI-5922), which can provide up to 24 bit digital resolution at sample rates up to 500 kS/s. At lower resolutions down to 16 bit, up to 15 MS/s can be measured. For the Mid-IR comb experiments, the card runs at 5 MS/s with a resolution of 20 bit. The control software for this setup is written in LabVIEW. For a measurement, the DAQ commands the stage to perform a scan at 20 cm/s. While this is performed, the ADC card measures the two FTIR signals from the Mid-IR and HeNe beams. One such scan takes around 4 s, after which the data is transferred from the cards memory into the memory of the computer itself and then both shown in the LabVIEW program and (if requested) saved. The data for both interferograms is stored on a high-speed redundant array of independent disks (RAID) in a separate computer connected via 10 Gbit/s network to the DAQ computer in a compact binary format. This process is taking some additional seconds, and while it is running the stage moves to its initial position to wait for the next scan.

For the evaluation, the two interferograms per scan are read in on the RAID computer using a MATLAB script. As a first step, the positions of each zero-crossing in the HeNe interferogram is determined via linear interpolation between the two data points adjacent to these crossings. In a second step, the Mid-IR interferograms are resampled to fit this grid defined by the HeNe laser, also done via interpolation. The measured interferogram is intentionally too long to fit the $f_{\mathrm{Res}} = c_0/\Delta l \stackrel{!}{=} f_{\mathrm{Rep},1}$ condition, ensuring that it can always be cut to the correct length. As a next step thus some points at both ends of the resampled Mid-IR interferogram are removed until this condition is met as good as possible. The Mid-IR data processed in this way is then saved to a new file together with the resampled data from all the other scans for this series. A second MATLAB script reads in this file to perform both an FFT on each of them and an averaging of these spectra, followed by subsequent data evaluation, like absorption calculations or the comparison between both dither lock from Section 3.2.2 on page 44 and the interferometric lock from Section 3.2.3 on page 45 which is described in the next section. The spectra shown earlier in Figure 3.9 on page 43 were measured using this spectrometer and evaluated as described. More details on the evaluation process, especially the resampling, can be found in reference [47].

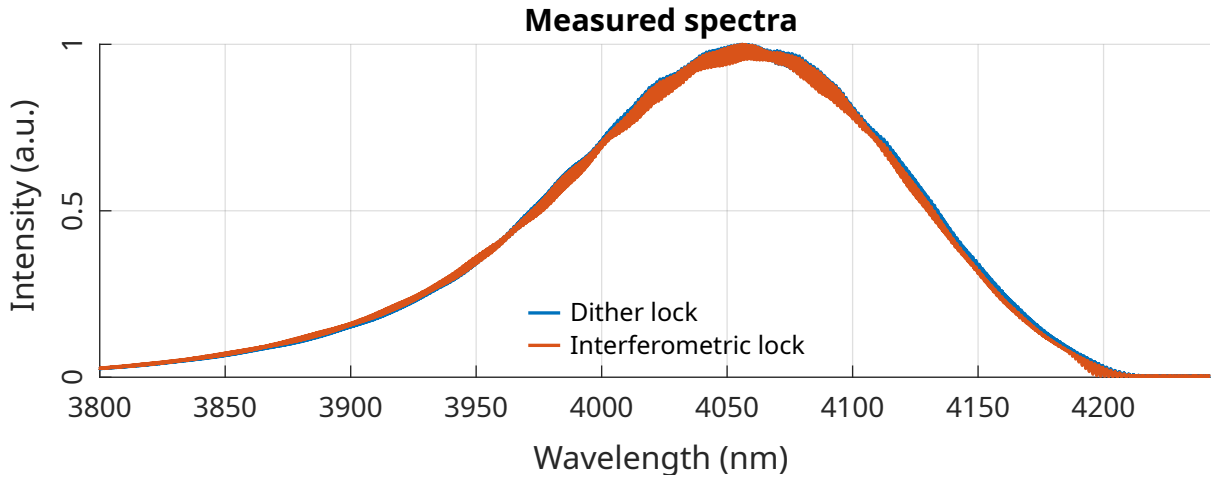

Figure 3.16: Measured Mid-IR spectra measured both with the dithered (blue) and interferometric locking (red) after integrating over 200 FTIR scans each, showing no major differences.

3.4 Comparison of dithered and interferometric locking

Using the FTIR spectrometer the long-term stability of the Mid-IR frequency comb can be characterized in a spectroscopic measurement setting, enabling a comparison between the different source stabilization methods. In addition to the these, the Mid-IR source can also run with no Δt stabilization at all, which as shown in reference [46] tends to drift away from the optimal operation point. This quickly results in worse spectral quality than with the dither lock engaged, which does improve over this free-running state by a factor of 1.7 in terms of the spectral SNR after averaging over 90 spectra. After measuring those spectra, the lock was disengaged to show a sudden drop in quality and thus the necessity of active stabilization.

In this work, the dither lock and the interferometric lock mechanisms are compared in a similar way. First, 200 spectra were measured for both systems running, which took around an hour each for both measurements. The average spectra for both series are shown in Figure 3.16, with the dither lock drawn in blue and the interferometric lock in red which they will be for the rest of the graphs in this section. It is obvious that both setups produce very similar spectra as no actual changes on the optical setups were made and the locking mechanism switch was purely electrical. Both spectra are also quite modulated as already mentioned in Section 3.2.1, caused by etalon filtering due to plane-parallel Ge windows.

For a quantitative comparison, the produced spectra for both pump/seed delay locking methods are analyzed in terms of their spectral SNR as introduced in Section 2.3.5. In Figure 3.17, the SNR is calculated for consecutive spectra inside the data sets. Here, the curves stay relatively similar to each other and are at a constant level, showing that

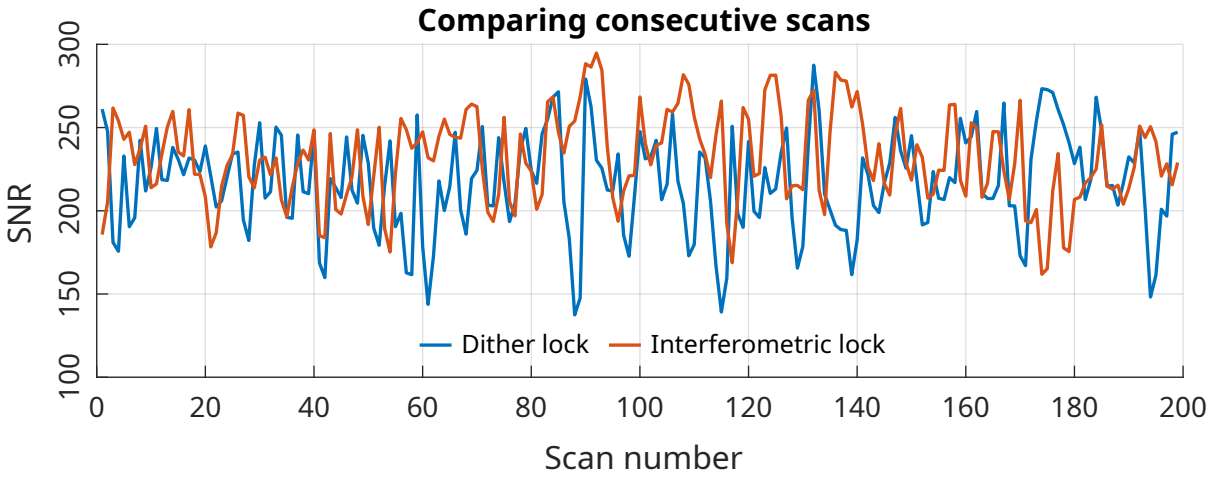

Figure 3.17: Calculated spectral SNR between consecutive spectra for both locking methods, showing that captured spectra are quite similar to their neighbours.

only small changes happen between adjacent scans for both methods. More interesting is the SNR calculation between one of the first scans to all subsequent scans which is shown in Figure 3.18. If starting with the very first scan as reference point, shown in (a), this plot shows that the dither lock starts off with a higher SNR between the compared spectra of above 250 in SNR than the interferometric lock which starts at 220. However, the spectra drift away from each other rather quickly for the dither lock down to 50 % of the initial value after only 50 scans while the interferometric lock stays above 90 % until around 150 scans when it drops quickly to 50 % of the initial SNR. Towards the end, the dither lock drifts back up. The chosen reference spectrum influences this data strongly. This is shown in Figure 3.18(b) which uses the fourth measured spectrum as the reference which produces better data for the interferometric lock and worse data for the dither lock than what is shown in (a). While it makes the most sense to do this drifting measurement against the very first spectrum, random fluctuations could cause it to be particularly different from the rest of the ensemble. For this reason, the drifts were given in relative numbers here.

For the final analysis of this chapter, the two datasets are divided along the spectra's indices as described in Section 2.3.5. This data is shown in Figure 3.19. Starting from the beginning of the data set, an increased number of spectra per subset is averaged for each point on the x axis to calculate the SNR between both subsets. For both stabilization methods, the SNR curves closely follow Equation (2.36) on page 30 describing the SNRs increase with the averaged ensemble size. For the dither lock, $SNR_{1,\mathrm{Dither}} \approx 211$ is measured, while the average single-spectrum SNR for the interferometric lock of $SNR_{1,\mathrm{Interf.}} \approx 226$ is about 7 % higher. This proves that the new interferometric lock presented in this work provides spectra of similar quality or slightly better than the dither lock that was previously used. This indicates that the modulation-

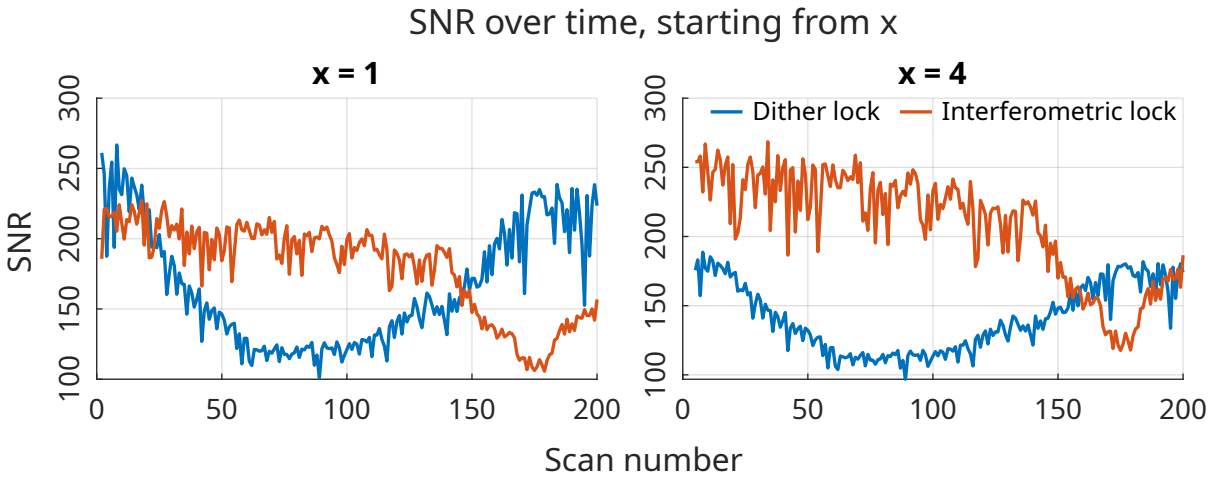

Figure 3.18: Calculated spectral SNR between early spectra (the very first (a) and the fourth (b) spectrum) and all following spectra for both locking methods, indicating drifting over the measurement. The interferometric lock keeps relatively stable up to about 150 spectra, while the dither lock quickly drifts away before coming back to the original state towards the end.

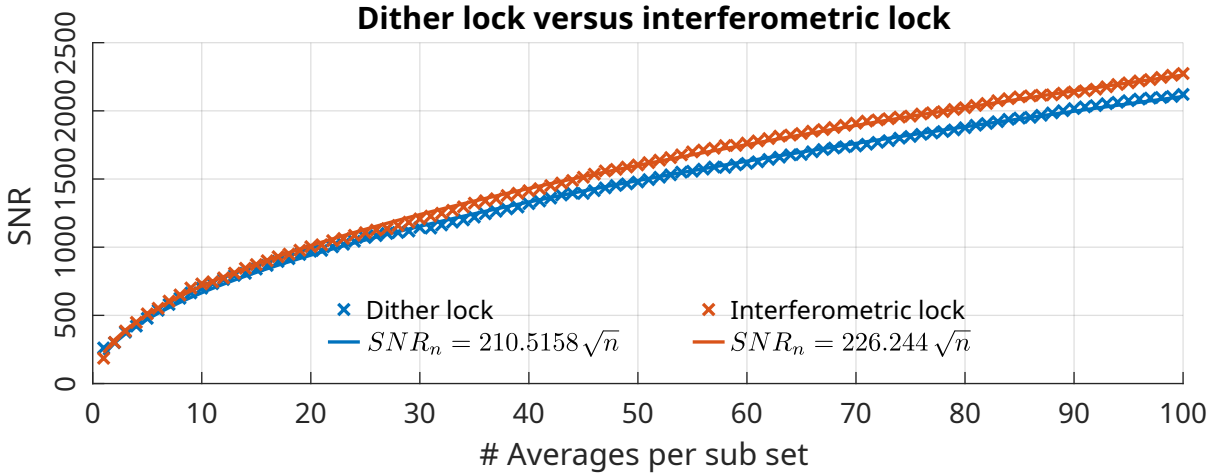

Figure 3.19: Calculated spectral SNR after averaging over the full dataset (see text for details). For both locks, the SNR as a function of the number of averages (per subset) can be approximated very well by $\sqrt{x}$ functions. Here, the interferometric lock had a small advantage of about 7 % over the dither lock.

free noise suppression works at least as well as the dither lock like the low residual OPD changes measured earlier in Section 3.2.3 suggested.

To summarize this chapter, the Mid-IR frequency comb's setup is presented as a source for coherent radiation in a spectral region between 3 to 5 µm with an output power of up to 20 mW. This source is based on splitting the output of a 1.5 W strong Near-IR frequency comb centered at 1060 nm in pump and seed beams with the seed experiencing Raman SSFS towards higher wavelengths, before recombination in a PPLN crystal for DFG. One property of the DFG setup is a strong RIN suppression inside a narrow region around perfect temporal overlap of both pump and seed beams. In previous works, this

overlap was stabilized using a dither lock which introduces sidebands as shown numerically in Section 2.3.4. In this work, this method was replaced with a new interferometric mechanism based on the interferometry of (residual) 1060 nm in pump and seed beams. This chapter shows that for this setup, the OPD between both beams can be stabilized to a sub-5 nm level (RMS). The two RIN suppression methods are then compared in a high-resolution FTIR spectroscopy setup, which is used here to measure the long-term stability of both methods in terms of their signal-to-noise performance. This experiment shows that the interferometric locking method provides equal or better RIN suppression and long-term performance as the dither lock.

In the next chapter, the coherence properties and optical line width of the generated Mid-IR frequency comb is investigated.

4 Mid-IR coherence investigations

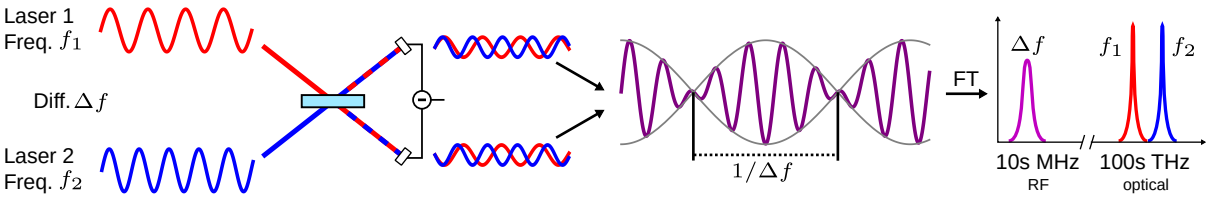

Figure 4.1: General principle for the coherence measurements of the Mid-IR comb. Two CW lasers with a frequency difference in the 10s of MHz range are interfering. The frequency difference causes the signal to alternate between constructive and destructive interference, measurable with RF measurement devices. This *beat* note can be used to determine the individual lasers line shapes.

In the last chapter the Mid-IR frequency comb source and its novel interferometric RIN suppression method were presented and characterized in terms of their long-term stability. It was shown that this method enables long-term RIN suppression on a similar level as the old dither locking method, while suppressing OPD fluctuations to a sub-5 nm level. In this chapter, the two methods are compared in terms of their influence on the Mid-IR comb's optical line shape, also including the free-running state of the setup. This is achieved via interferometry with a secondary frequency comb locked to the same low-line width reference laser to generate a heterodyne beat. This beat enables a line width measurement of the Mid-IR frequency comb relative to the used reference comb (and subsequently to their common optical reference) down to a sub-Hz level [86]. Furthermore, it is shown that the dither locking introduces optical sidebands to the Mid-IR frequency comb due to the required OPD modulation, which are non-existent with both the free-running state and the interferometric locking. These sidebands are shown to be consistent with the predictions in Section 2.3.4. Combined with the results from the last chapter, this shows the capability of the chosen comb generation and stabilization approach to be usable in a long-term stable high-resolution spectroscopy experiment.

4.1 Optical line width measurements with frequency combs

The principle for the Mid-IR comb's coherence investigation is shown in Figure 4.1. In this sketch, two narrow-line CW lasers with equal power and a small difference Δf in the 10s of MHz in their frequencies $f_{1,2}$ (optical frequencies in the 100s of THz) are brought to interference on a balanced photodiode (BPD). The frequency difference causes the combined light field to alternate between constructively and destructively interfering at

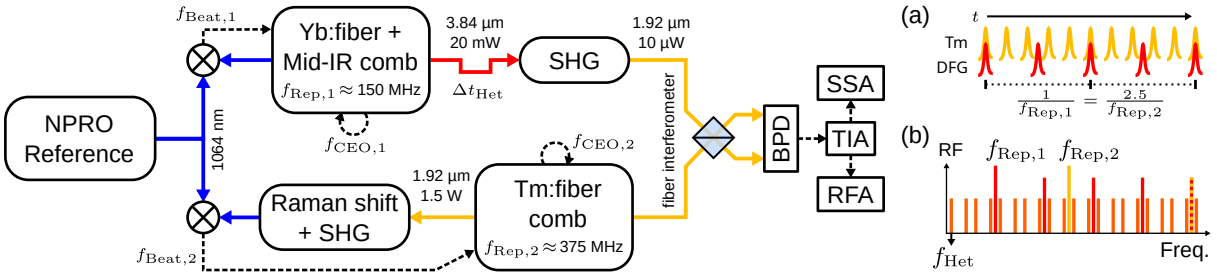

Figure 4.2: Experimental setup for the measurement of the Mid-IR comb's coherence by beating its SHG around 2 µm with a second Tm:fiber comb at the same wavelength. Both combs are locked to the same reference laser. Inset (a) shows the temporal overlap occuring between both combs after setting the relative delay Δt_{Het} and correct repetition rates $f_{\mathrm{Rep},2} = 2.5 f_{\mathrm{Rep},1}$. Inset (b) shows the resulting RF spectrum with the repetition rate peaks $n f_{\mathrm{Rep},1}$ and $n f_{\mathrm{Rep},2}$ together with the wanted beat notes at frequency f_{Het} (mirrored around $n f_{\mathrm{Rep},1}/2$).

the frequency $\Delta f = f_{\mathrm{Het}}$. This signal, the heterodyne beat note, can be detected by the BPD and suitable RF measurement equipment. Its line shape is the convolution of the two interfering lasers' line shapes. If one of them is known, the other can be determined via deconvolution of the beat note and the known laser's line shape.

A frequency comb can be thought of as a linear combination of many such CW lasers/comb modes oscillating in phase. As such, the interference of single comb modes produces beat notes in a similar manner, with multiple comb modes interfering simultaneously to produce a multitude of beat notes. These are separated by the greatest common denominator of their repetition rates $f_{\mathrm{Rep},1/2}$. Using the principle shown in Figure 4.1 thus allows to measure the optical line shape and the coherence properties of frequency combs. Here, a Tm:fiber frequency comb is used to characterize the Mid-IR frequency comb in this regard. This second laser system is situated next to the Mid-IR source with both systems sharing a laser table.

In Figure 4.2, the setup for the Mid-IR comb's coherence measurements is shown. It shows the Yb:fiber frequency comb together with the Mid-IR conversion setup on top and the Tm:fiber comb below. Both lasers are locked to the same NPRO CW reference laser at 1064 nm. In case of the Tm:fiber comb this requires additional Raman SSFS and subsequent SHG, detailed more in the next section. The Mid-IR frequency comb is set up such that its output spectrum is centered at 3.84 µm at output powers of 20 mW, twice the central wavelength of the Tm:fiber comb's oscillator spectrum at 1.92 µm. Using a zinc germanium phosphide ($ZnGeP_2$), (ZGP) crystal, about 10 µW of the Mid-IR comb's second harmonic at this target wavelength are generated and then coupled into a fiber interferometer to beat with the Tm:fiber frequency comb. The interferometers signal is detected with a simple home-built BPD using two anti-parallel fiber-coupled photodiodes (Hamamatsu G12182-003K) and analysed using either an RF analyzer (Agilent E4402B) or an SSA (Agilent E5052B) for phase noise measurements.

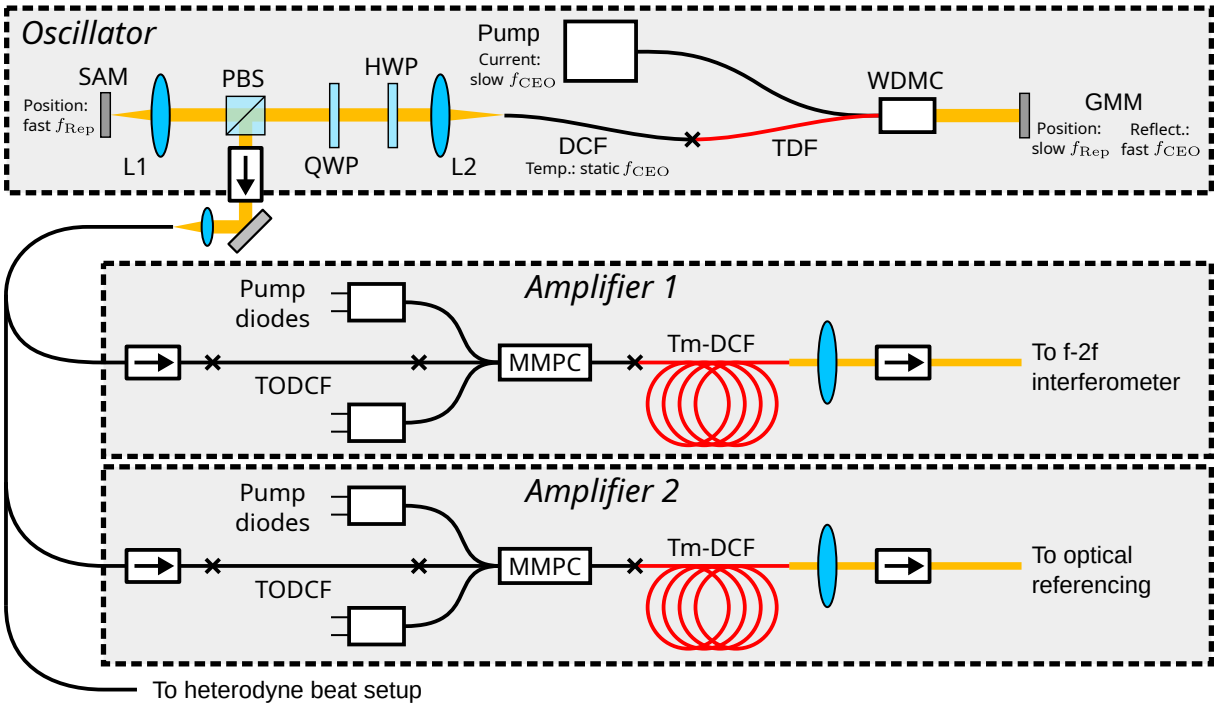

Figure 4.3: Setup for the Tm:fiber frequency comb. Similarly to the Yb:fiber comb described in Section 3.1, this laser consists of an oscillator with a linear cavity driving two amplifiers. The amplifiers output is already (mostly) compressed, so no further compressor is required. PBS: Polarizing beam splitter, DCF: (here) dispersion-compensating fiber, TDF: Thulium-doped fiber, WDMC: Wavelength division multiplexer and collimator, GMM: Graphene modulating mirror, Tm-DCF: Thulium-doped double cladding fiber, TODCF: Third-order dispersion compensation fiber, MMPC: Multimode pump combiner.

In Figure 4.2(a), the optical pulses of the two combs are shown schematically in the time domain. The Tm:fiber frequency comb's repetition rate is set to $f_{\mathrm{Rep},2} = 2.5 \times f_{\mathrm{Rep},1} = 379.125\,\mathrm{MHz}$ (with $f_{\mathrm{Rep},1} = 151.65\,\mathrm{MHz}$). This ratio between both repetition rates allows for interfering pulses every second pulse of the Mid-IR comb or every fifth pulse of the Tm:fiber comb. A manual delay stage on the Mid-IR comb's output is then used to set the temporal overlap $\Delta t_{\mathrm{Het}} = 0$ between both combs. With the temporal overlap established, distinct beat notes at frequencies $n \times f_{\mathrm{Rep},1}/2 \pm f_{\mathrm{Het}}$ emerge in the measured RF spectra, as sketched in Figure 4.2(b).

4.2 Tm:fiber comb laser used for reference

The setup of the Tm:fiber frequency comb (IMRA Tm-400-1.5, [87, 88]) is shown in Figure 4.3. It consists of an oscillator with a linear cavity pumped by up to 2 W of 1560 nm laser light and an output spectrum centered around 1.92 µm. This cavity consists of a fiber section containing the Tm-doped gain fiber and a dispersion compensating fiber, and a free-space section with polarization control and the SAM used to mode-lock the laser. For

out-coupling the laser light, a PBS is used in this section. Both cavity end mirrors are used for $f_{\mathrm{Rep},2}$ stabilization. The fast feedback is provided by a lead-filled copper mount holding the SAM similar to the one used in the Yb:fiber laser [79]. The slow feedback is provided with a piezo delay stage below the other end mirrors assembly. This end mirror is fitted with a graphene layer, providing fast feedback for $f_{\mathrm{CEO},2}$ via electro-optic modulation of its reflectivity. Slow feedback to $f_{\mathrm{CEO},2}$ is provided via pump current modulation of the oscillators pump. Additional tuning range is provided by a heating plate on the dispersion compensating fiber to move the beat notes into the locking electronics filter bandwidth if required.

After out-coupling from the oscillator, the light is coupled back into an optical fiber and split into different sections. Two amplifiers provide further amplification of the laser light up to 2 W each, with output pulse durations down to 100 fs in the case of the second amplifier. This is achieved by careful fiber dispersion management, not requiring an additional compressor setup like in the Yb:fiber laser. The amplifiers consist of TODCF of unknown length followed by the Tm-doped gain fiber. These are pumped by two 12 W pump diodes at a wavelength of 793 nm. Further outputs of the oscillator are split into various open ports and photodiodes for diagnostics. One such diagnostics port is used for the heterodyne beat experiment to measure the coherence of the Mid-IR frequency comb. The parameters of this laser system are summarized in Table 4.1.

Laser parameter	**Value**
Central wavelength	1920 nm (oscillator) 1950 nm (amplified)
Spectral bandwidth	<30 nm
Repetition rate	379.125 MHz
Output power	2 W on both amplifiers
Pulse duration	100 fs on amplifier 2

Table 4.1: Tm:fiber frequency comb parameters

4.2.1 Optically referencing the comb and frequency locking

For this work, the amplifiers in this laser system are both used to provide light for the comb's phase locking mechanisms. The optical setups for these are shown in Figure 4.4. In (a), the f-$2f$ interferometer driven by amplifier 1 is shown. In this setup, the amplified light is coupled into SMF-28 fiber of around 30 cm length to compress the pulses, before it is coupled to a HNLF for spectral broadening. In this fiber the octave-wide spectrum is generated by blue-shifting the input 1.95 µm from the amplifier down to about 1.1 µm in addition to Raman SSFS towards 2.2 µm where the fiber transmission starts to cut off. A PPLN crystal is used to frequency-double the red-shifted light to overlap with the

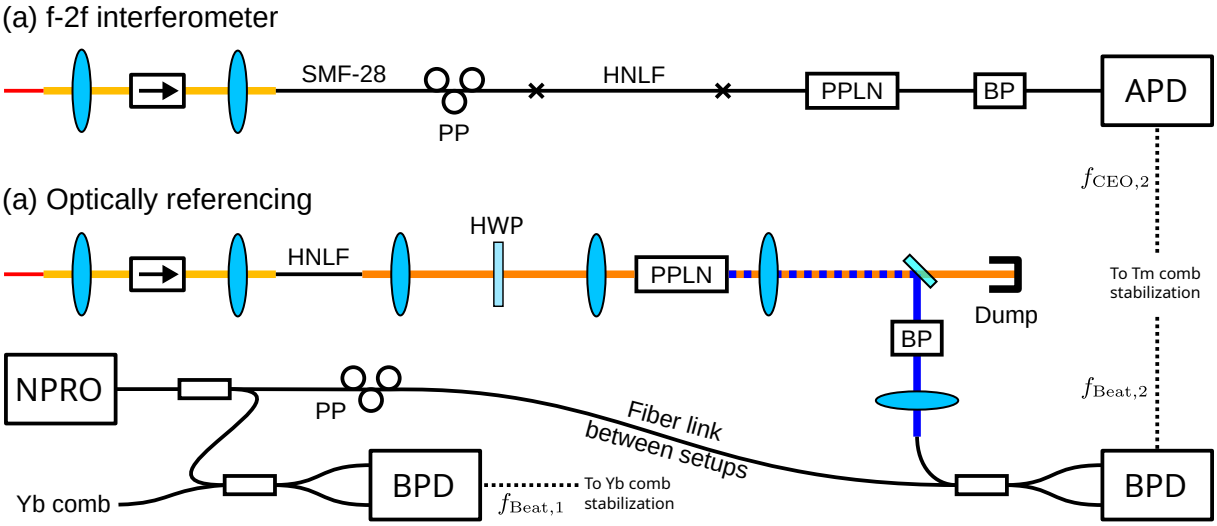

Figure 4.4: Used optical setups to measure both $f_{\mathrm{CEO},2}$ (self-referencing) and $f_{\mathrm{Beat},2}$ in the Tm:fiber frequency comb. In (a), the fiber-based f-$2f$ interferometer used for self-referencing is shown. In (b), the setup used to optically reference the comb is shown. The output from the second amplifier is red-shifted and subsequently frequency-doubled to lock the 1.95 µm Tm:fiber comb to the 1064 nm NPRO reference of the Yb:fiber comb.

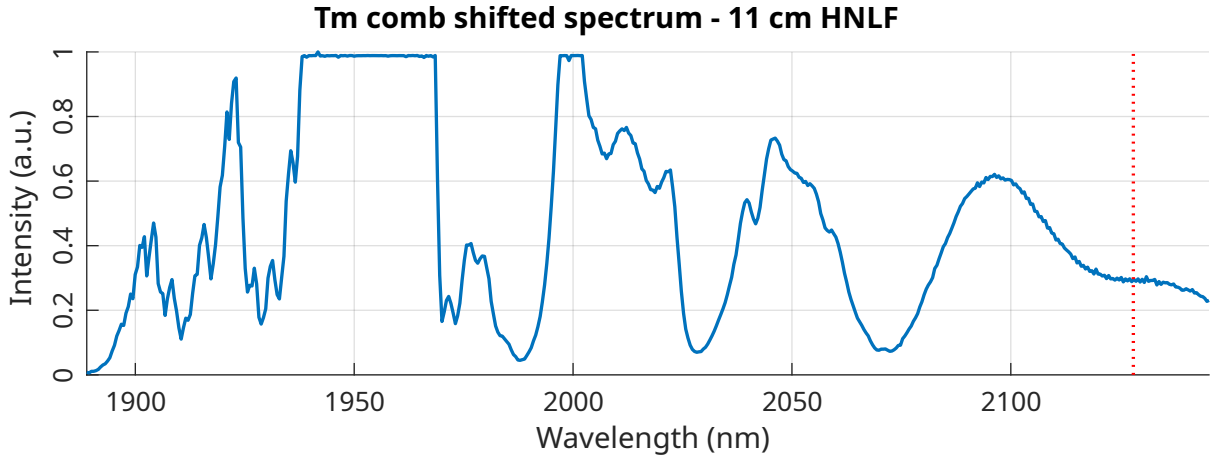

Figure 4.5: Spectral broadening with an optimized HNLF length of 11 cm, providing a usable soliton at 2128 cm when driven with the full 1.5 W of optical output power of amplifier 2.

1.1 µm radiation. This light is bandpass-filtered and directed onto an APD to detect the Tm:fiber frequency comb's $f_{\mathrm{CEO},2}$ offset frequency.

In Figure 4.4(b) the optical referencing of the Tm:fiber frequency comb is shown. Both it and the Yb:fiber comb driving the Mid-IR source are optically referenced to the same CW laser, enabling the measurement of relative line widths at a sub-Hz level [86]. Here, the 1064 nm NPRO for the optical referencing of the Yb:fiber frequency comb is also used for the Tm:fiber (Coherent Mephisto). As the NPRO reference is frequency-stabilized to stabilize the Mid-IR comb's repetition rate, the optical referencing also serves to stabilize the Tm:fiber frequency comb's repetition rate $f_{\mathrm{Rep},2}$ in the same manner. To do so, its

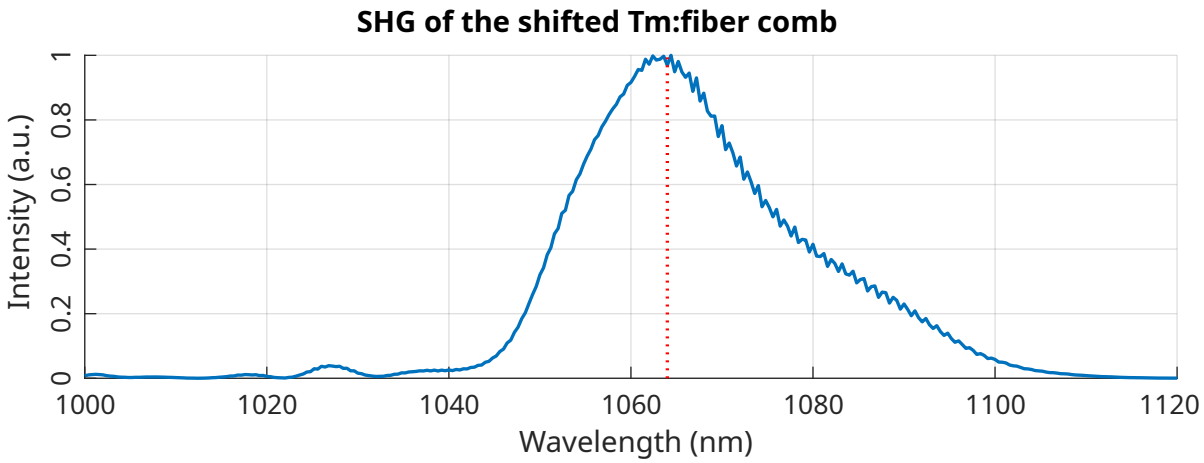

Figure 4.6: Optical spectrum of the SHG of the red-shifted Tm:fiber comb. For frequency-doubling, a PPLN with a period length of 31.59 µm at a temperature of 180 °C (Covesion MOPO1-1.0-1 + PV10) was used to generate a well-centered spectrum around 1064 nm for beating with the NPRO reference laser.

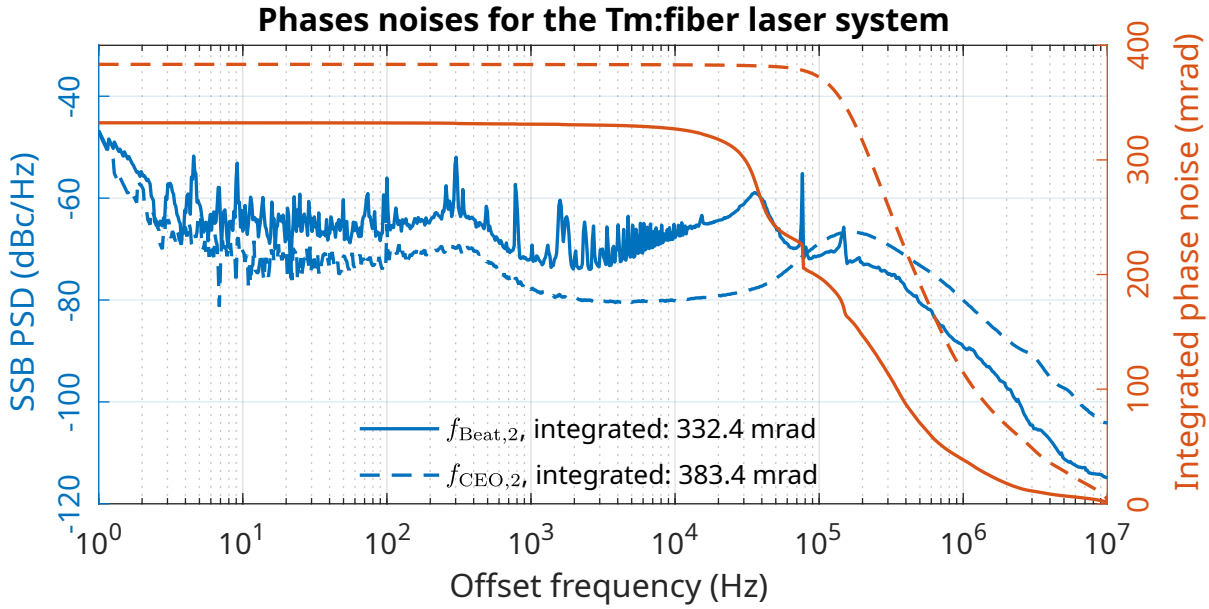

Figure 4.7: Plot of the phase noises for the $f_{\mathrm{CEO},2}$ and $f_{\mathrm{Beat},2}$ locking systems on the Tm:fiber laser, measured with an SSA, equivalent to Figure 3.6 which shows the same data for Yb:fiber laser driving the Mid-IR source. Here, the $f_{\mathrm{CEO},2}$ lock shows a slightly worse performance than the one for $f_{\mathrm{Beat},2}$.

second amplified output is spectrally broadened and shifted before beating with the NPRO reference. The output of the second amplifier is first coupled into a HNLF (Sumitomo HNDS1614A-10-4-3) via a very short piece of SMF-28 (<1 cm) to ease incoupling. The output spectrum at HNLF length of 11 cm is shown in Figure 4.5. In addition to this, Appendix A contains further spectra recorded at different HNLF lengths.

The spectrally red-shifted light is coupled out of the fiber, passing a HWP for polarization adjustments and then focused into a heated PPLN crystal (Covesion MOPO1-1.0-1 +

PV10, set to 180 °C with a period length of 31.59 µm) for SHG from 2128 nm to 1064 nm. In Figure 4.6, the spectrum of this second harmonic is shown to be well-centered around the target wavelength marked with a red dashed line. After additional bandpass filtering, this light is coupled into a fiber interferometer for beating with the NPRO which is transported via a several meter long fiber link to the Tm:fiber comb's setup.

The heterodyne beat $f_{\mathrm{Beat},2}$ of the NPRO and the frequency-doubled Tm:fiber comb is detected using a BPD. Both $f_{\mathrm{Beat},2}$ and $f_{\mathrm{CEO},2}$ are stabilized using locking electronics with designs and layouts very similar to the ones used in the Yb:fiber laser as shown in Section 3.1.2 on page 37. The phase noise power spectral densities for both stabilized beat notes can be seen in Figure 4.7. Here, the integrated phase noise from 1 Hz to 10 MHz is 332.4 mrad and 383.4 mrad for the $f_{\mathrm{Beat},2}$ and $f_{\mathrm{CEO},2}$ frequencies, respectively. The $f_{\mathrm{Beat},2}$ signal shows a servo bump around 40 kHz, similar to the phase noises for the Yb:fiber laser shown earlier in Figure 3.6 on page 40. For $f_{\mathrm{CEO},2}$, this servo bump is close to 200 kHz. In Table 4.2, the locking parameters for the Tm:fiber frequency comb are summarized.

Stabilized frequency	**Actuators**	**Set frequency (Hz)**
Carrier-envelope-offset frequency $f_{\mathrm{CEO},2}$	Fast: Graphene modulator mirror Slow: Oscillator current Static: fiber temperature	± 140 000 000 (typical)
Beat frequency with NPRO reference $f_{\mathrm{Beat},2}$	Fast: Piezo end mirror Slow: Graphene mirror	± 140 000 000 (typical)
Comb's repetition rate $f_{\mathrm{Rep},2}$	Via NPRO from Yb:fiber laser	379 125 000 (target value)

Table 4.2: Phase locked loops for the Tm:fiber frequency comb. The exact frequency values for f_{Beat} and f_{CEO} will be determined later in Section 4.3.2.

4.3 Establishing the heterodyne beat

For interference of the Mid-IR frequency comb and the Tm:fiber comb to occur, both sources have to overlap in both time and spectrum. In this section, the establishment of these overlaps is described.

4.3.1 Spectral overlap

The spectral overlap is established by first tuning the Mid-IR source such that its output is centered at twice the Tm:fiber frequency comb's central wavelength of 1.92 µm. The measured and optimized spectra are shown in Figure 4.8. First, the input power to

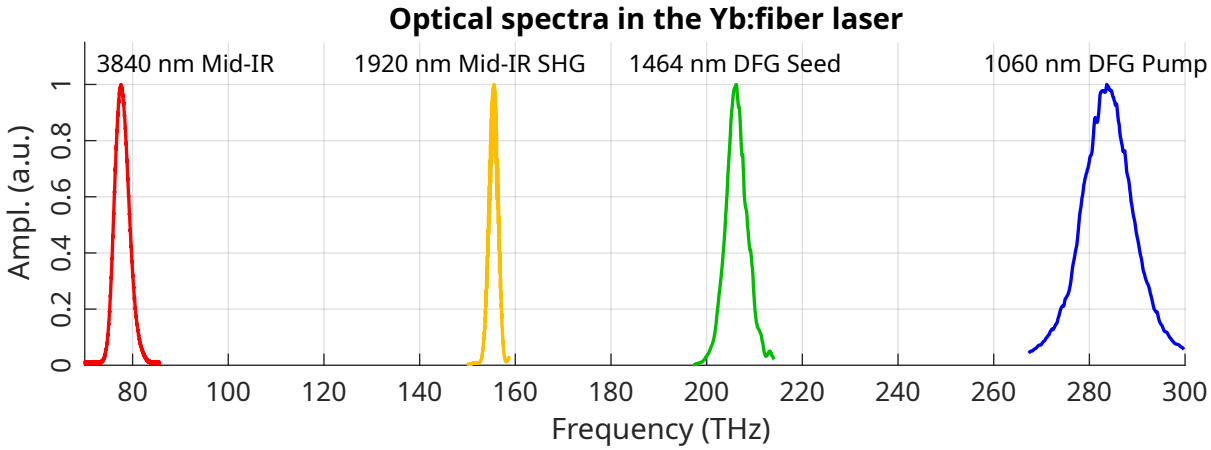

Figure 4.8: The different optical spectra in the Mid-IR frequency comb prior to beating with the Tm:fiber comb at 1.92 µm, all normalized to their respective maxima.

the HNLF generating the seed beam is tuned such that its central wavelength is about 1464 nm (measured with an Ando AQ6317B). Together with the pumps central wavelength of 1060 nm (measured with an OceanOptics STS-NIR) this ensures the required central Mid-IR wavelength of 3.84 µm is mathematically met according to Equation (2.9) on page 10. Following this, its generation is optimized by tuning the PPLN crystal where the DFG process takes place in both grating period and temperature and observing the output using the FTIR spectrometer described in Section 3.3 together with a power meter. Using 29.09 µm and 120 °C, respectively, this tuning resulted in Mid-IR outputs of up to 20 mW at the correct wavelengths.

Using a flip-mirror, the generated light is then diverted to the SHG. Here, a lens with $f = 40\,\text{mm}$ focuses the Mid-IR radiation into a 2.73 mm long ZGP crystal. In Section 3.2.1, the Mid-IR beam was focused to a spot size of about 200 µm as measured with a beam profiler (Ophir Optronics Pyrocam IIIHR) using a lens with $f = 100\,\text{mm}$. As the focal length of the lens for the SHG is about half of the lens used for the beam profiling, the spot size is estimated to be about $2r = 100\,\mu\text{m}$. Assuming the Mid-IR pulses are of the same duration as the pumping Yb:fiber laser of $\tau = 147\,\text{fs}$, the Mid-IR beams peak intensity at the ZGP crystal can be estimated to be about $I_0 = P_{\text{avg}}/(f_{\text{Rep},1}\tau\pi r^2) = 11.55\,\text{MW/cm}^2$ with $P_{\text{avg}} = 20\,\text{mW}$ the beams average power. A second lens with $f = 50\,\text{mm}$ is then used to collimate the generated light, which is coupled into a fiber interferometer together with the Tm:fiber comb to perform the heterodyne beat. The fiber is connected to a Near-IR spectrometer (OceanOptics NIRQuest 512, range of 1890 to 2145 nm) for detection. The crystal is cut at a phase matching angle of $\theta_m = 60.9°$. By tilting the crystal, its phase matching is adjusted for the SHGs output at the correct 1.92 µm, and beam angles are optimized for a maximum fiber-coupled output of the SHG of about 10 µW, an efficiency of about 0.05 % for this process. The spectrum of the resulting radiation and the spectrum of the Tm:fiber lasers oscillator are

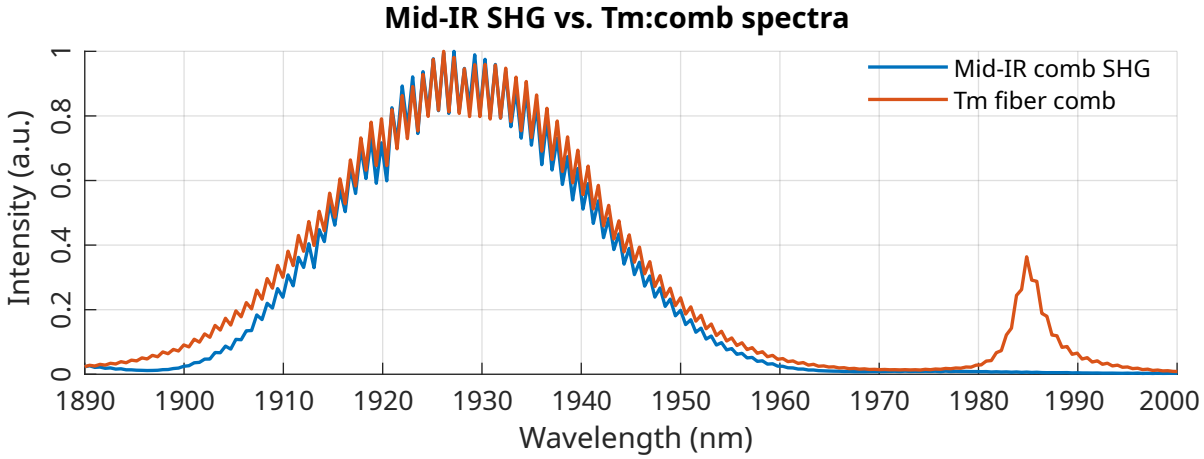

Figure 4.9: Overlapped spectra of both the Tm:fiber comb and the Mid-IR comb's SHG, showing near perfect overlap of both light sources apart from the Tm comb's oscillator sideband at 1985 nm.

shown in Figure 4.9 with very good overlap apart from a sideband at 1985 nm appearing in the oscillators' spectrum. The spectrometer is then replaced with the fiber interferometer to measure the heterodyne beat.

4.3.2 Establishing temporal overlap between both combs

While the spectral overlap was established quickly, a consistent temporal overlap is significantly more difficult to achieve. To help visualize how critical this overlap is, the duty cycle of the second harmonic of the Mid-IR is estimated. The Mid-IR source has a repetition rate of $f_{\mathrm{Rep},1} = 151.65\,\mathrm{MHz}$, or a period length of about 6.6 ns. The pulse duration from the Mid-IR source is much shorter than that. Here it is estimated to be of the same order of magnitude as the driving Yb:fiber laser pulse duration, which is about 100 fs. By dividing the latter by the first, the duty cycle of the laser is calculated to be about 1.5×10^{-5}. This means that the lasers repetition rates need to be set very precisely in order for the two lasers to match the 2.5 ratio of their repetition rate and stay synchronized long enough for the measurements to take place.

In addition to this, the NPRO is already tuned via feedback from the Yb:fiber frequency comb to stabilize its repetition rate $f_{\mathrm{Rep},1}$, thus the Tm:fiber comb has to be tuned via the $f_{\mathrm{Beat},1/2}$ and $f_{\mathrm{CEO},1/2}$ locked frequencies. The locking frequencies from the Yb:fiber laser influence the Tm:fiber laser as well, as they effectively result in a shift of the NPROs output frequency even without changing $f_{\mathrm{Rep},1}$. This situation is shown in Figure 4.10 which visualizes the two lasers comb equations. On top, the Yb:fiber frequency comb equation is visualized in red, with one comb mode-locked to the blue NPRO reference laser at frequency ν_{Ref}. On the bottom, the same is shown for the Tm:fiber comb in yellow. The aim is to find locking frequencies that ensure the condition $f_{\mathrm{Rep},2} = 2.5 \times$

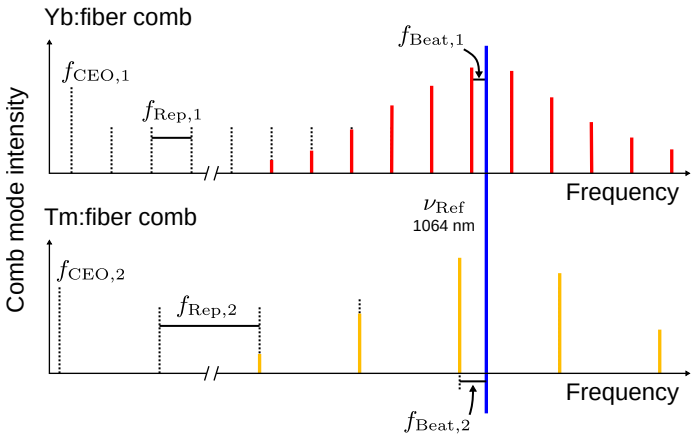

Figure 4.10: Visualization of the two comb equations for both the Yb:fiber and the Tm:fiber frequency combs beating with the CW reference laser at frequency ν_{Ref}, close to 1064 nm. The goal is to find a set of frequencies $f_{\mathrm{CEO},1/2}$ and $f_{\mathrm{Beat},1/2}$ ensuring $f_{\mathrm{Rep},2} = 2.5 \times f_{\mathrm{Rep},1}$.

$f_{\mathrm{Rep},1} = 379.125\,\mathrm{MHz}$ is met to ensure a stable temporal overlap between both frequency combs over the duration of the following measurements.

In order to achieve this goal, a simplified version of the heterodyne beat setup shown in Figure 4.2 is set up, which uses two known coherent outputs as the input for the fiber interferometer in order to ease finding the signal. This simplified setup is shown in Figure 4.11(a) and beats the 1064 nm outputs used for optically referencing the two lasers. Temporal overlap Δt_{Het} is established using a delay stage on one of the two lasers outputs. In both lasers, the optical referencing produces beat notes between the frequency combs and the NPRO reference with high SNRs above 30 dB. Therefore, a heterodyne beat between those should also produce a coherent signal.

The initial values for $f_{\mathrm{CEO},1} = f_{\mathrm{Beat},1} = -122\,\mathrm{MHz}$ for the Yb:fiber comb were chosen such that the Tm:fiber frequency comb's repetition rate $f_{\mathrm{Rep},2}$ was adjustable to the required $2.5 \times f_{\mathrm{Rep},1} = 379.125\,\mathrm{MHz}$ via its reference frequencies for $f_{\mathrm{Beat},2}$ and $f_{\mathrm{CEO},2}$ without moving them out of their RF filter bandwidth. Using switches on the locking electronics, the signs for $f_{\mathrm{Beat/CEO},2}$ were set such that an increase in their absolute values results in an increase in repetition rate, as such $\mathrm{sgn}\,(f_{\mathrm{CEO},2}) = -$ and $\mathrm{sgn}\,(f_{\mathrm{Beat},2}) = +$. Initial adjustment of their value to 144.808 MHz resulted in a repetition rate close to the correct value. By continually adjusting the frequencies down to a Hz-level and reestablishing $\Delta t_{\mathrm{Het}} = 0$ between both combs using the delay stage, they were optimized such that the overlap is kept stable long enough for the following measurements. In the end, using $f_{\mathrm{Beat},2} = 144.808\,257\,408\,\mathrm{MHz}$ and $f_{\mathrm{CEO},2} = 144.808\,372\,\mathrm{MHz}$ the temporal overlap was kept for over 1 min without a noticeable drop in SNR for the resulting beat notes. The resulting beat notes are shown in Figure 4.11(b), proving the high degree of mutual coherence between both frequency combs.

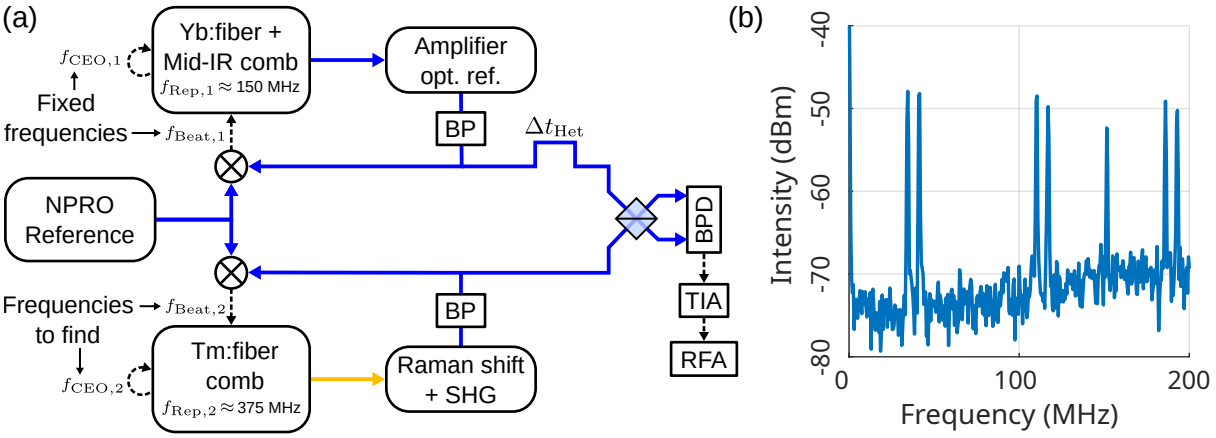

Figure 4.11: (a) Used setup for beating the two lasers bandpass-filtered 1064 nm signals, simplified compared to Figure 4.2 to ease finding the correct frequencies using known coherent outputs. These are used to optically reference the lasers to the NPRO. (b) Measurement of the beat notes between both combs (RBW 300 kHz), showing a high degree of mutual coherence for stable temporal overlap Δt_{Het}.

4.4 Coherence measurements

With both lasers successfully synchronized, the coherence of the DFG setup together with the influences of the different long-term stabilization methods can be studied in detail.

4.4.1 First measurements

Using the setup shown in Figure 4.2 first resulted in a signal with no clearly distinguishable coherent peaks. Instead, with $\Delta t_{\mathrm{Het}} = 0$ established, an increase in noise of about 30 dB at low frequencies was observed. This first result is shown in Figure 4.12. By beating the output of the HNLF producing the seed beam for the DFG process with a low-line width 1560 nm CW laser, it was found that this process was not optimized well. This resulted in beat notes with only 5 dB SNR. Further investigations using the FROG measurement device (Mesaphotonics FROGscan Ultra) revealed amplified pulses from the Yb:fiber comb with pulse durations longer than 160 fs FWHM and significant side pulses. As stated in reference [35], longer input pulse durations can result in decreased coherence in the supercontinuum processes which generate the seed beam. This lead to shortening both the Yb:fiber laser's TODCF from 183 to 86 cm and its compressor grating distance from 28.6 to 20.2 cm, resulting in a significant improvement of its pulse shape. The pulses before and after their optimization are shown in Figure 4.13, the data for the latter is the same data shown earlier in Figure 3.4 on page 38. Following this pulse optimization, the SNR of the beat notes between the seed beam and the CW laser improved to above 20 dB.

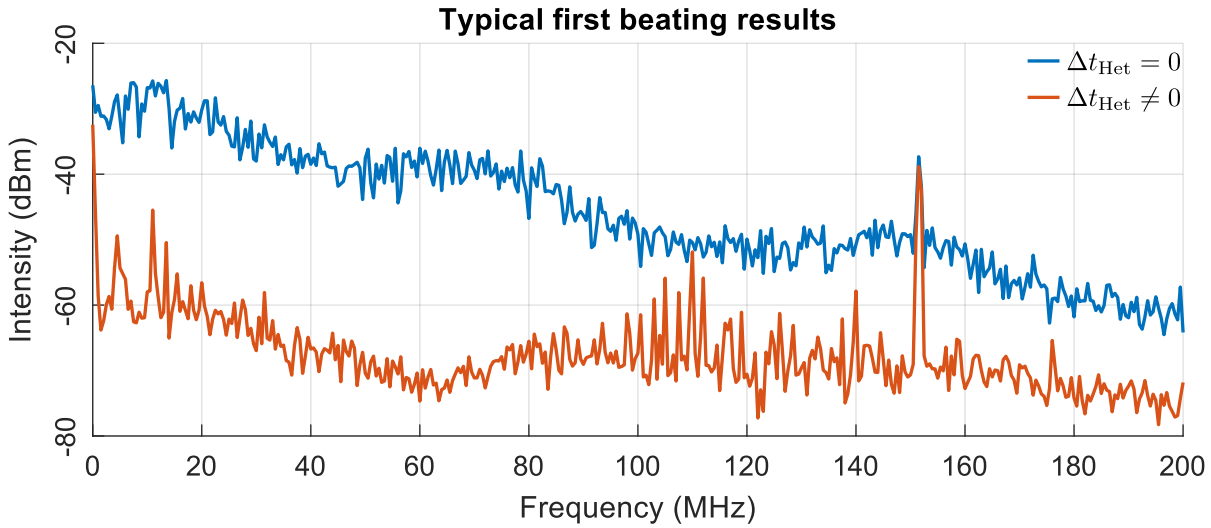

Figure 4.12: First signals for the heterodyne beat between the Mid-IR SHG and the Tm:fiber frequency comb. At $\Delta t_{\mathrm{Het}} = 0$ (in blue) an increased noise background compared to $\Delta t_{\mathrm{Het}} \neq 0$ (red) with no distinct beat notes was observed. The repetition rate peak for the Tm:fiber comb at 375 MHz was not recorded for these first scans. Measured at 300 kHz RBW.

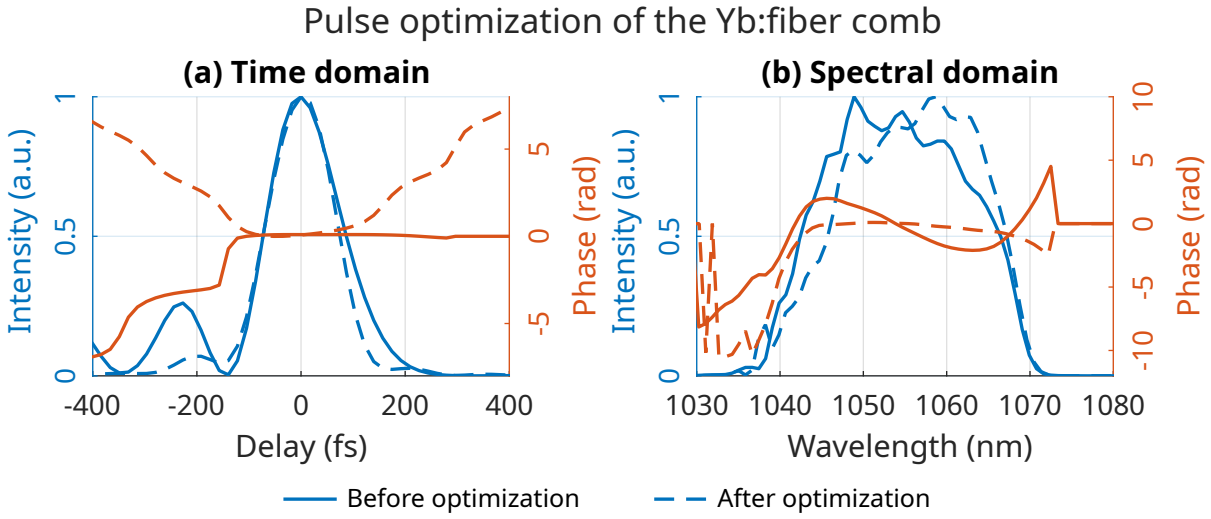

Figure 4.13: FROG traces (measured with a Mesaphotonics FROGscan Ultra) from the Yb:fiber frequency comb before and after the pulse optimization. The data for the latter is the same as in Figure 3.4 on page 38

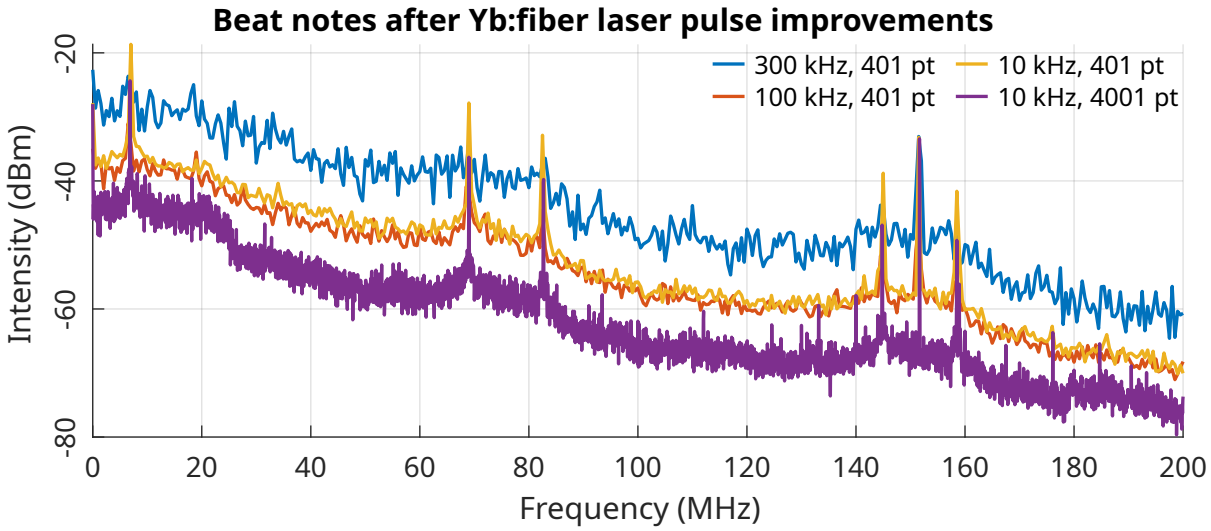

Figure 4.14: First measurements of the beat notes between the Mid-IR SHG and the Tm:fiber comb following the improvements on the Yb:fiber laser. At high RBWs of 300 kHz, beat notes were well hidden among the noise background. A decrease in resolution down to 10 kHz shows them clearly.

4.4.2 Beat notes after Yb:fiber laser pulse improvements

With the laser pulses optimized in this way, the coherent signal at 1.92 µm became clearer. In Figure 4.14, the first signals after this optimization are shown, with decreasing resolution bandwidth (RBW) and increasing amount of data points. While the first measurement at an RBW of 300 kHz only seems slightly clearer than the first signals between different scans of the RF analyzer, decreasing the RBW down to 10 kHz reveals clearly distinct signals at a frequency $f_{\mathrm{Het}} \approx 6.841\,\mathrm{MHz}$ repeatedly mirrored around $n/2f_{\mathrm{Rep},1} \approx 75\,\mathrm{MHz}$. These beat notes appear with an SNR of about 10 dB above the noise floor. In Figure 4.15, an additional measurement is shown also including the repetition rate peak for the Tm:fiber frequency comb, comparing the two temporal overlap situations $\Delta t_{\mathrm{Het}} = 0$ and $\Delta t_{\mathrm{Het}} \neq 0$, still showing an increase in low-frequency noise floor by around 20 dB at temporal overlap for the lowered 10 kHz in RBW. In Figure 4.16, a first comparison between a strongly modulated (3 V in dithering amplitude) and unmodulated pump/seed delay Δt in the DFG stage at similar spans and RBWs as the last curve in Figure 4.14 is shown. On this scale however, the modulated and unmodulated curves are indistinguishable.

4.4.3 Effects of pump/signal delay modulation on the Mid-IR beam

For a more detailed comparison between the pump/seed delay stabilization schemes, the scale is decreased in a systematic way around the central frequency $f_{\mathrm{Het}} \approx 6.841\,\mathrm{MHz}$. Starting at measurement spans of 200 kHz at an RBW of 1 kHz and down to a span

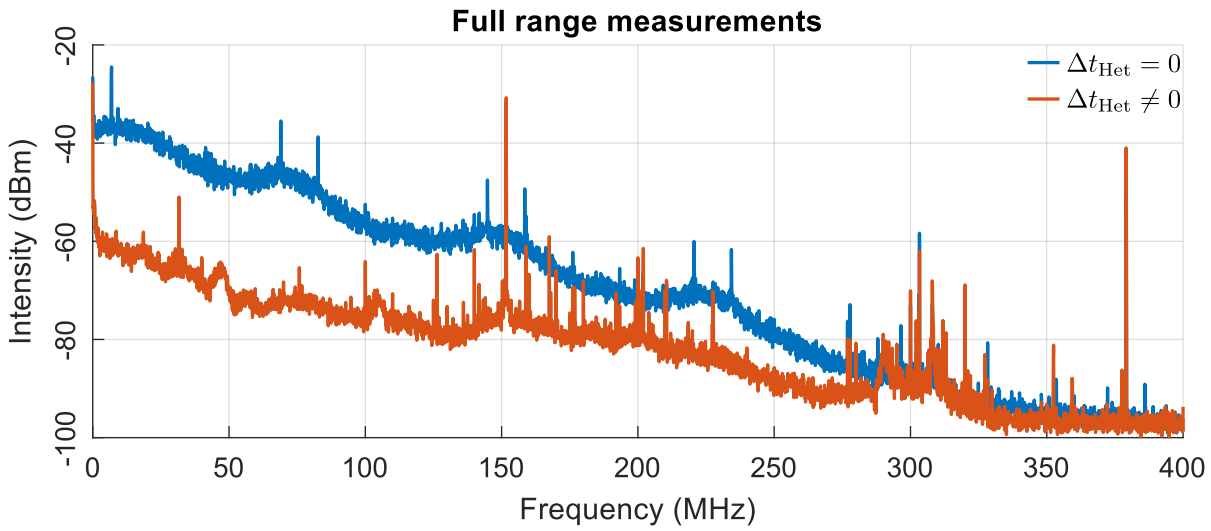

Figure 4.15: Full measurements of the heterodyne beat between the Mid-IR SHG and the Tm:fiber comb, showing both lasers repetition rate signals. This was measured both with and without temporal overlap occuring, similar to Figure 4.12. The RBW is 10 kHz for both scans.

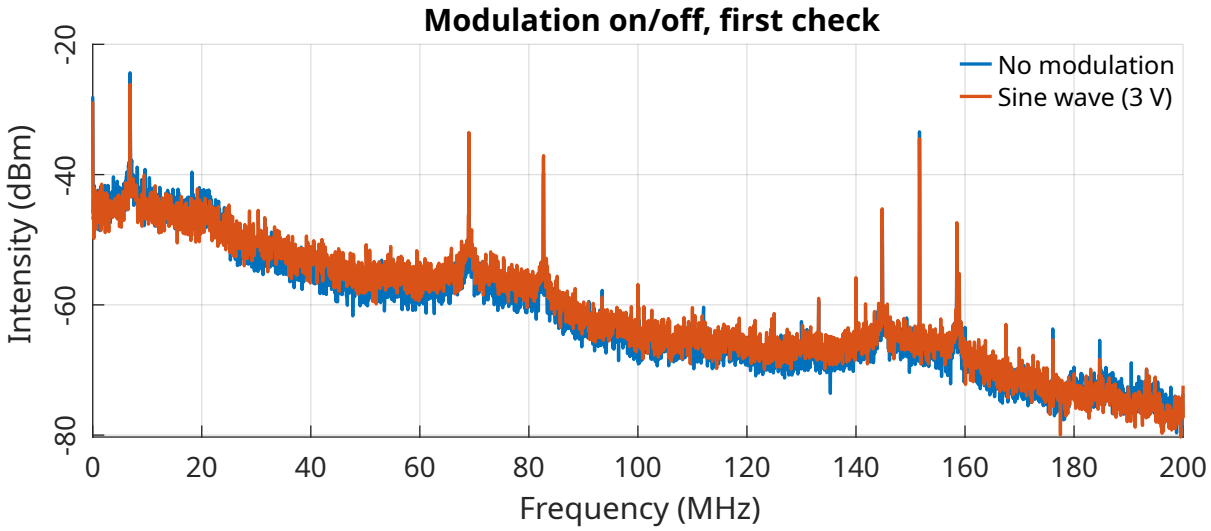

Figure 4.16: Comparison of 2 µm beat notes for an unmodulated and a strongly modulated (3 V peak-to-peak) pump-signal delay in the Mid-IR source. On this scale, no difference between measurements is visible.

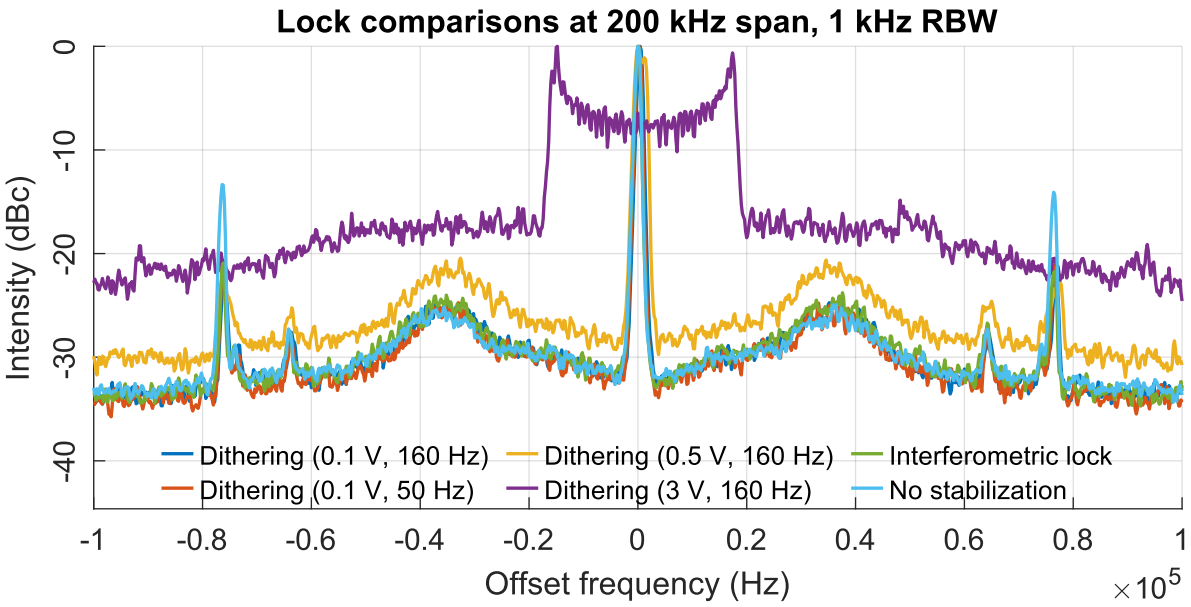

Figure 4.17: Measurement of the 6.841 MHz beat note with the three different locking mechanisms used. For the dithering, four different settings with three different amplitudes (3, 0.5 and 0.1 V) and two frequencies (160 and 50 Hz) are shown. All measurements have been normalized to the maximum signal amplitude. At this 200 kHz span, only the strongest dithering amplitude results in a significant sideband generation.

of 200 Hz with 1 Hz RBW, beat notes are measured for six different stabilization and modulation settings. These include the free-running and the interferometrically stabilized pump/seed delay, together with three modulation amplitudes of $U_{\mathrm{Mod}} = 3,\ 0.5$ and 0.1 V at a modulation frequency $f_{\mathrm{Mod}} = 160$ Hz. The lowest one, which represents the typical dithering amplitude when engaging this stabilization method, was additionally tested at a different frequency $f_{\mathrm{Mod}} = 50$ Hz. The following measurements are averaged over 50 scans of the RF analyzer, and the resulting plots are normalized to the maximum value of each measurement.

At the highest span of 200 kHz at an RBW of 1 kHz shown in Figure 4.17 the only measurement significantly deviating from the ensemble is the one at the highest dithering amplitude of 3 V. This curve shows strongly modulated sidebands with most amplitude in the beat note shifted towards offset frequencies of ±16 kHz. As shown in Section 2.3.4, the constant dithering of the pump/seed delay stage in the Mid-IR source imprints a phase modulation onto the pump beam due to the Doppler effect, which transfers to the output of the Mid-IR source (conserving strength and width) and subsequently its SHG, where the width of the modulation doubles. This modulation transfer is shown in Figure 2.15 on page 27.

Following the formalism shown in Section 2.3.4, the measured signal at $U_{\mathrm{Mod}} = 3$ V and $f_{\mathrm{Mod}} = 160$ Hz is compatible with an imprinted phase modulation of $KU_{\mathrm{Mod}} \approx 33.8\pi$

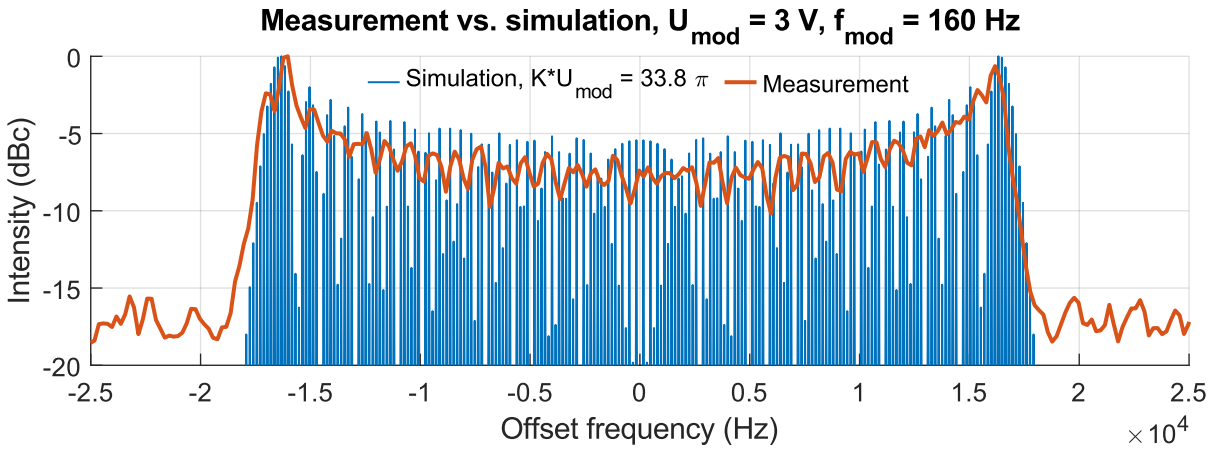

Figure 4.18: Comparison of the modulated beat note spectra for $U_{\mathrm{Mod}} = 3\,\mathrm{V}$ and $f_{\mathrm{Mod}} = 160\,\mathrm{Hz}$. In blue, a simulated phase modulation with a $KU_{\mathrm{Mod}} = 33.8\pi$ is shown, in red, the measured data from Figure 4.17 for this case is overlaid.

for the resulting Mid-IR SHG. In Figure 4.18, a comparison between the measured data for this case and a simulation with these parameters is shown, showing good agreement between the phase modulation model and the measurements for the general shape of the resulting spectrum. The other measurements exhibit a clear coherent peak with an SNR of about 30 dB, surrounded by small servo bumps at about ±35 kHz and resonances between 70 to 80 kHz, stemming from referencing the two combs to the NPRO reference laser. For a comparison with the phase noise of the stabilized f_{Beat} frequencies, see Figure 3.6 on page 40 and Figure 4.7 on page 62.

At a span of 10 kHz and 100 Hz RBW shown in Figure 4.19, the lower dithering amplitudes of $U_{\mathrm{Mod}} = 0.5$ and 0.1 V at the same modulation frequency are visibly deviating from the rest of the curves as well. The measurement with $U_{\mathrm{Mod}} = 0.1\,\mathrm{V}$ and $f_{\mathrm{Mod}} = 50\,\mathrm{Hz}$ on the other hand is not distinguishable from the free-running and interferometrically locked state. However, from the measured data it is difficult to extract quantifiable information as the used RF analyzer produced artifacts in the form of an apparent saw-tooth function imprinted on the measured signals with a period of around 1 kHz. As such, no simulations to compare the measured signals against were performed here.

At the next lower span of 2 kHz and an RBW of 10 Hz, shown in Figure 4.20, the sideband structure for all the measurements with a dithered pump/seed delay becomes visible, both for the three measurements at $f_{\mathrm{Mod}} = 160\,\mathrm{Hz}$ and for the one at $f_{\mathrm{Mod}} = 50\,\mathrm{Hz}$. At the lowest amplitude of 0.1 V, the comparison between the two different modulation frequencies shows that with lower frequency less sidebands are introduced, showing three visible sidebands per side at offset frequencies ±160, 320 and 480 Hz for $f_{\mathrm{Mod}} = 160\,\mathrm{Hz}$ and only two at offsets of ±50 and 100 Hz for $f_{\mathrm{Mod}} = 50\,\mathrm{Hz}$. According to Equation (2.34) on page 28, the modulation frequency should have no influence on the amplitude of the side bands. It is therefore possible that the modulation index K becomes a function of

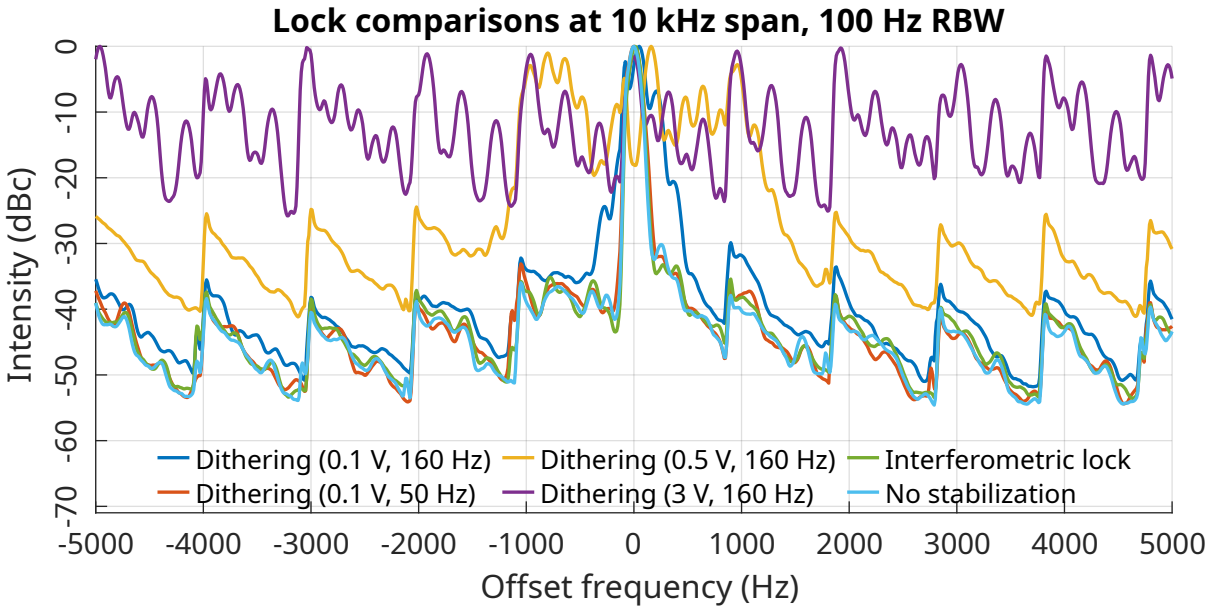

Figure 4.19: At 10 kHz, the two other dither amplitudes at 160 Hz are visibly discernible from the dither-free curves and the 0.1 V/50 Hz. The apparent saw-tooth structure is most likely a measurement artifact.

the frequency f_{Mod} for the used delay stage. Most importantly, the shape of the central beat note becomes visible in these measurements. It stays constant between the different stabilization schemes and modulation settings with no apparent changes aside from its SNR between measurements due to the differing modulation strengths. This shows that while the dithering method introduces significant sidebands to the signal, the optical line shape of the Mid-IR frequency comb relative to the reference comb itself is not affected. Again, the imprinted saw-tooth function makes quantitative analysis difficult for these measurements.

At the last measured span of 200 Hz with an RBW of 1 Hz shown in Figure 4.21, only the central 1.92 µm heterodyne beat note between the Mid-IR SHG and the Tm:fiber frequency combs is shown for nearly all measurements due to the low span. The single scan at $f_{\mathrm{Mod}} = 50$ Hz includes sidebands which appear as lower amplitude copies of the central peak. At this scale, nearly identical line shapes are measurable for all modulation or stabilization settings, and the measured FWHM line widths are below 2 Hz at the same order of magnitude as the RBW. This indicates relative line widths between both combs of about 1 Hz, but likely not significantly smaller than that. Importantly, the comparison between the free-running state and the interferometrically locked DFG setup does not show a significant difference in this measurement. For this reason, further investigations of the heterodyne beat between both combs are based on its phase noise PSD, measured using the SSA instead of the RF analyzer.

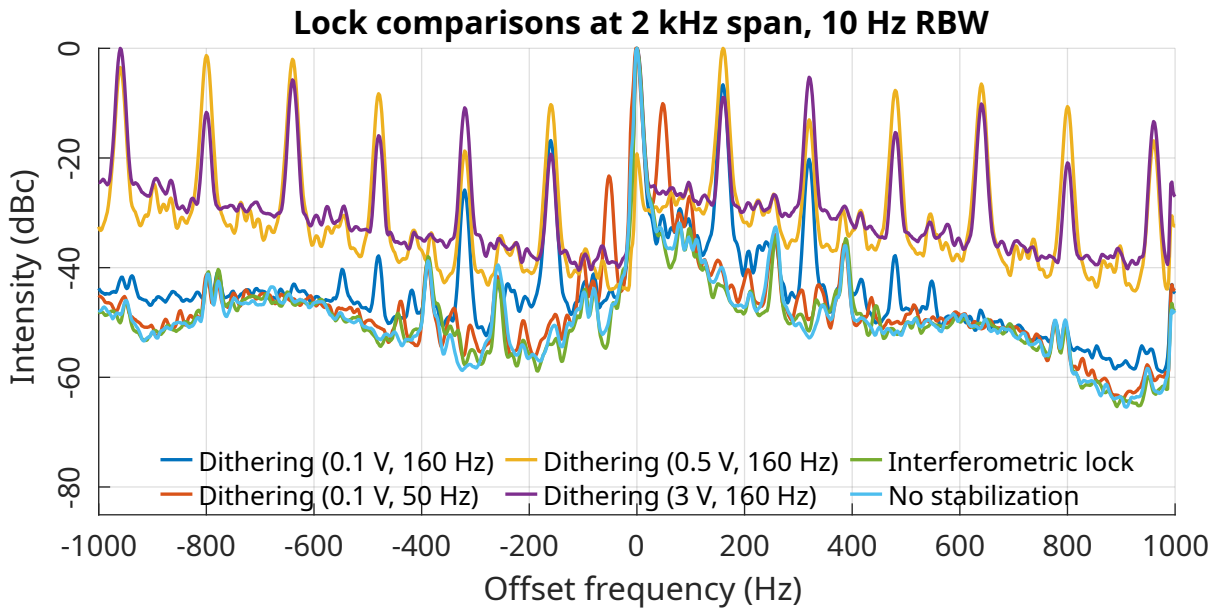

Figure 4.20: At 2 kHz and 10 Hz RBW, the sideband separation by the used f_{Mod} becomes visible. This measurement shows that the line shape of the central beat note does not change between the different locking mechanisms. Like in Figure 4.19 the apparent saw-tooth structure is most likely stemming from the RF analyzer.

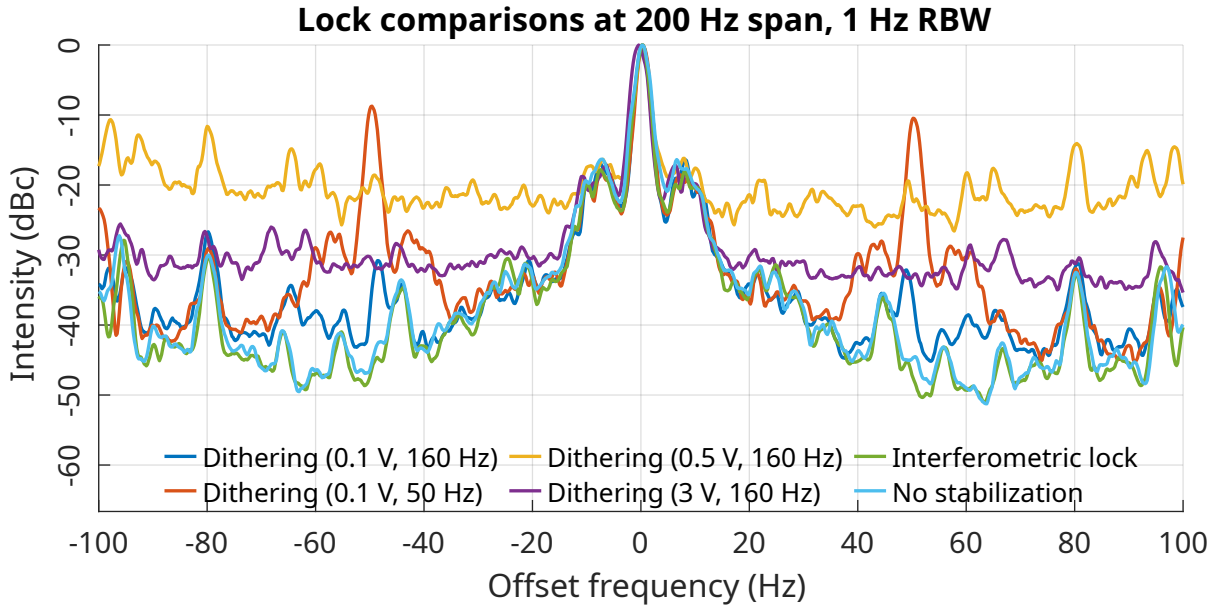

Figure 4.21: At 200 Hz and 1 Hz RBW, the structure of the central beat note becomes clearly visible. This shows even clearer that the form of the central peak does not change between the different locking methods. At high modulation strengths, its amplitude decreases due to the sideband generation, leading to increased noise background in this normalized depiction. In this view, no significant difference between interferometrically stabilized and unstabilized cases can be observed.

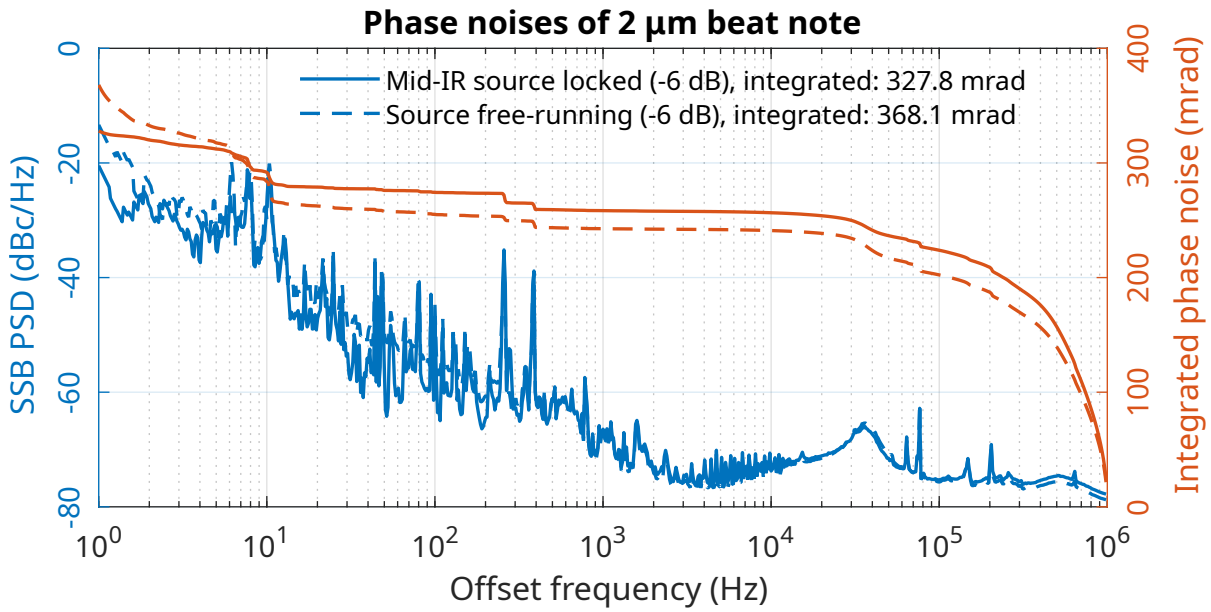

Figure 4.22: Plot of the phase noises of the 2 µm beat notes between the Mid-IR sources SHG and the Tm:fiber laser, similar to Figures 3.6 and 4.7. 6 dB were subtracted from the PSD to correct for the SHG. The Mid-IR source is running both interferometrically stabilized and free-running, and the data shows a similar noise performance for both states, with a possible small advantage for the locked state at frequencies below the delay stages resonances at 258 and 388 Hz.

4.4.4 Phase noise measurements of the 2 µm beat note

In Figure 4.22, the measured phase noises for the 1.92 µm heterodyne beat between the Mid-IR comb and the Tm:fiber frequency comb are shown. On the left, blue axis the measured single-sideband power spectral density (SSB PSD) for the phase noise is shown, while the right, red axis shows the phase noise integrated from 1 MHz to 10 Hz. This is the same scale as used for Figure 3.6 on page 40 and Figure 4.7 on page 62 to ease comparisons. For these measurements, the beat note close to 220.66 MHz was selected due to the SSAs capabilities and filter availability. This beat note was isolated using a tunable bandpass filter (Telonic Berkeley TTF250-5-5EE) before being fed into the SSA. In both SSB PSD curves, 6 dB are subtracted to acquire the phase noise for the Mid-IR comb itself without the influence of the SHG, halving the integrated phase noise in the process, analogue to reference [89]. In solid lines, the results for the interferometrically stabilized Mid-IR source, and in dashed lines the ones for the free-running state are shown. In the SSB PSD plot, the results show very high agreement from high frequencies down to around 255 and 388 Hz. Below these frequencies, the interferometric lock gains a small advantage, leading to a slightly reduced integrated phase noise of 327.8 mrad compared to the free-running state with 368.1 mrad.

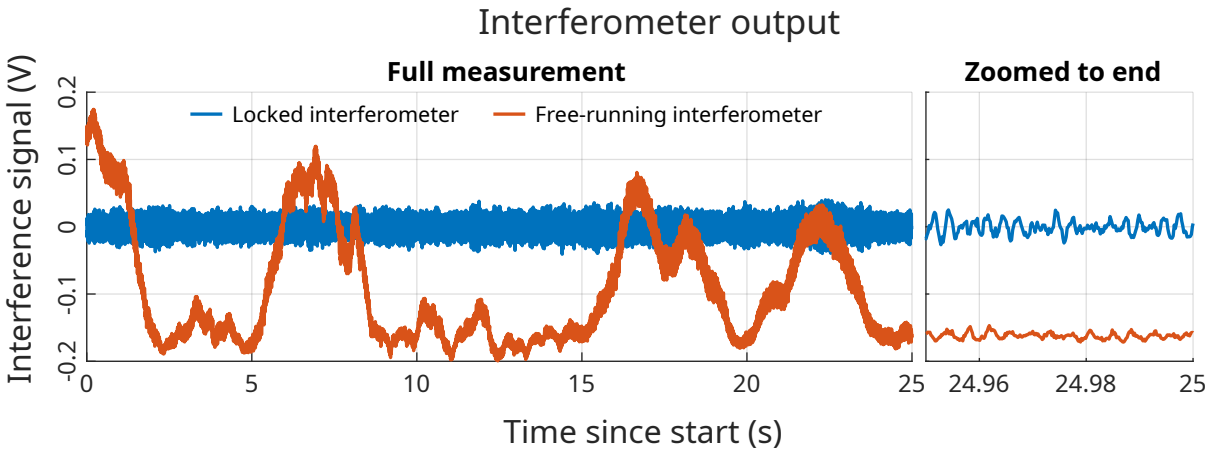

Figure 4.23: Interferometer outputs measured over a short time for both an interferometrically locked and unstabilized pump/signal delay stage. The outputs will be Fourier transformed to compare their spectra with the measured phase noise in Figure 4.22. On the right, a zoom to the last 50 ms of the measurements is shown.

Correlations in phase noise and interferometer output

While measuring the phase noise for both states, the locking interferometers output was logged in order to find correlations in its electric spectrum with the phase noise PSD, similar to what was shown at the end of Section 3.2.3. The measured scans are shown in Figure 4.23 with the locked interferometer in blue and the unlocked interferometer in red. On the right side of the plot a zoom to the last 50 ms of the measurement shows how both signals are dominated by oscillations. In Figure 4.24 the fast Fourier transform (FFT) of the unlocked interferometers output is shown on a linear scale in blue on the left axis and compared with the measured SSB PSD for this state in red on the right axis. The resulting FFT of the interferometers output shows two distinct peaks near 250 and 400 Hz which coincide very well with the 255 and 388 Hz resonances in the measured phase noise data. Only very few peaks at other frequencies exist in this data set, and it is dominated by low-frequency noise.

By contrast, the locked interferometers output's FFT shown in Figure 4.25 consists of significantly more resonant peaks with the low frequency noise from the unlocked interferometer absent. Of those resonances only the same ones as in the unlocked case near 250 and 400 Hz have a matching resonance in the phase noise. Others such as the ones near 300 and 450 Hz only appear in the interferometer's output, but are absent in the phase noise, likely being caused by electric interference in the stabilization electronics.

In Figure 4.26, the $f_{\mathrm{Beat},1/2}$ phase noise PSDs of the two driving lasers (shown earlier in Figure 3.6 on page 40 and Figure 4.7 on page 62) and the ones of the 1.92 µm heterodyne beats (shown in Figure 4.22 on the preceding page) are compared. The top plot containing the measured SSB PSD for all cases shows good agreement between the phase noise of the

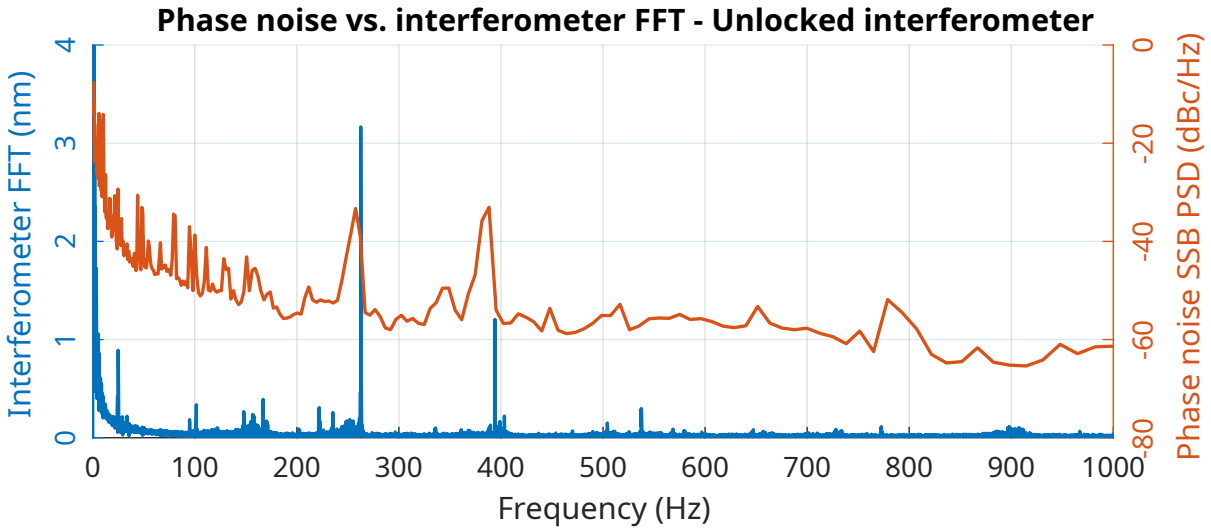

Figure 4.24: Spectrum of the unlocked interferometers output from Figure 4.23 compared to the corresponding phase noise from Figure 4.22. The frequency axis is shown on a linear scale up to 1 kHz, and two dominant peaks around 260 and 388 Hz emerge in both the interferometers output and the measured phase noise of the 2 µm heterodyne beat.

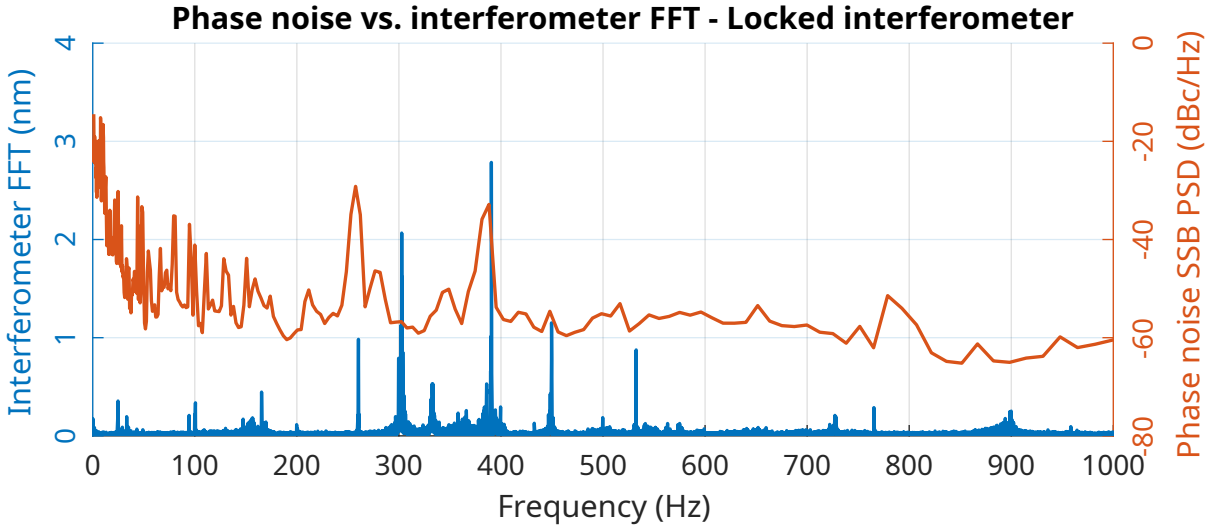

Figure 4.25: Spectrum of the locked interferometers output Figure 4.23 compared to the corresponding phase noise from Figure 4.22. The scaling is kept from Figure 4.24. In addition to the peaks in the previous Figure, additional peaks emerge in the interferometers output which not neccessarily find clear equivalents in the heterodyne beats phase noise.

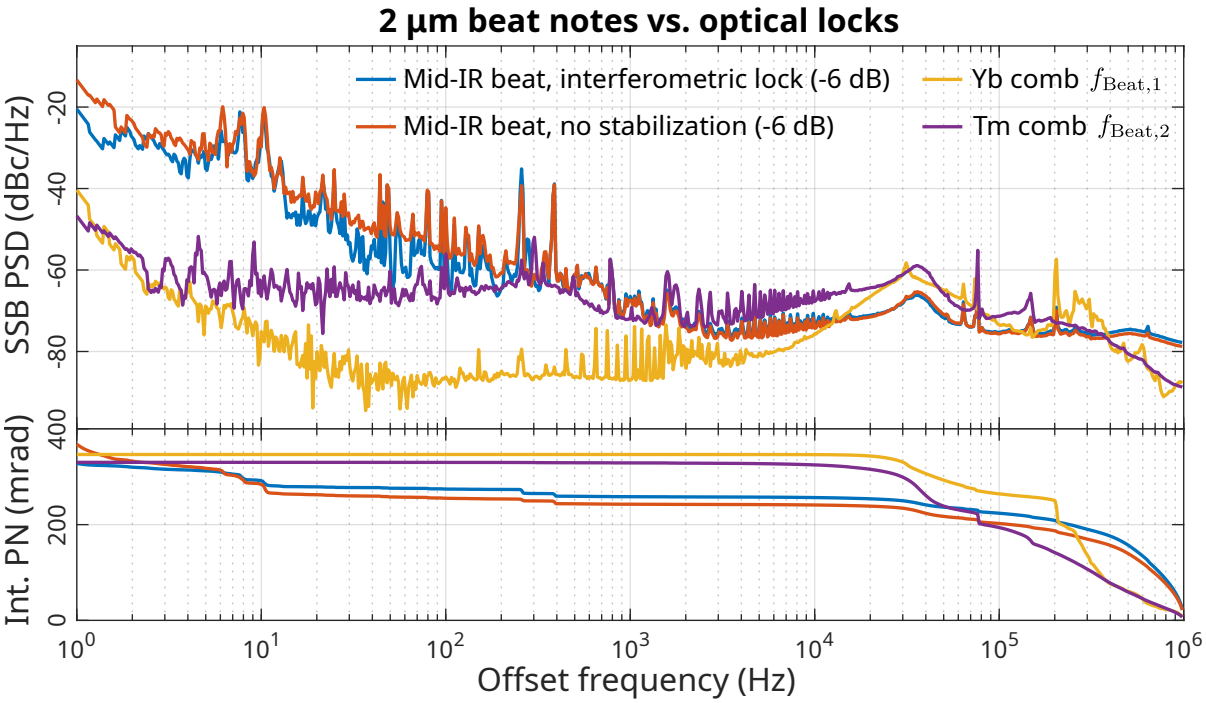

Figure 4.26: Measured phase noises for the two lasers locked $f_{\mathrm{Beat},1/2}$ signals (same data as in Figures 3.6 and 4.7) and the heterodyne beat at 2 µm between them (taken from Figure 4.22). In the upper plot, the single-sideband power spectral densities are shown, the lower plot contains the integrated phase noises. The data shows good agreement above 1 kHz, below that the heterodyne beats phase noise is dominated by acoustic noise compared to the $f_{\mathrm{Beat},1/2}$ signals.

Tm:fiber lasers optical stabilization and the two combs' heterodyne beat at frequencies above 1 kHz. In this range, the Tm:fiber laser limits the heterodyne beats phase noise. At frequencies below 1 kHz, the two combs' heterodyne phase noise PSD is dominated by acoustic noise in both locked and unlocked cases, while the $f_{\mathrm{Beat},1/2}$ stabilizations suppress this noise effectively in their PSDs. This discrepancy is caused by the long beam paths between both combs' outputs and the heterodyne beat setup which includes long optical fibers and in the case of the Mid-IRs SHG a significant amount of various free-space optics and nonlinear processes.

The integrated phase noises are shown in the lower plot in Figure 4.26, showing them to lie in the same order of magnitude over the full integration range. Following Equation (2.25) on page 25 defining the line width of the beat notes, in both the interferometrically locked and the free-running Mid-IR source the measured integrated phase noises (1 Hz to 1 MHz) of 327.8 and 368.1 mrad, respectively, are below 1 rad for the entire integration range. As such, the measured phase noise for both cases translates to sub-Hz relative line widths between the Tm:fiber frequency comb and the Mid-IR source.

To summarize this chapter, employing the second frequency comb enabled a measurement of the Mid-IR frequency comb's coherence via measuring the phase noise PSD of their heterodyne beat. In this experiment, it was shown that the Mid-IR frequency conversion

resulted in a line broadening on a sub-Hz level relative to the reference comb and in turn the driving Near-IR frequency comb. Both combs are optically referenced to an NPRO Nd:YAG laser with an optical line width of approximately 1 kHz via PLLs with similar phase noise performance to the 2 µm beat notes as shown above. As such, the optical broadening of the Mid-IR comb becomes nearly inconsequential and its optical line shape would be well-defined by the line shape of the reference. Replacing this reference with a system with a lower line width should thus yield lower optical line widths in the Mid-IR comb as well, down to a sub-Hz level. Only in this regime the acoustic noise introduced by vibrations of the optics in the Mid-IR conversion setup dominates the phase noise of the Mid-IR comb and would pose the lowest limit of the Mid-IR combs' absolute line width. An additional limit to the resolution of the entire comb spectroscopy setup arises from the used HeNe reference/calibration laser in the FTIR spectrometer. This laser has an optical line width of about 1 MHz which is orders of magnitude higher than the one of the combs' optical reference. As such, a spectroscopic measurement would only show features with widths down to this level and higher resolutions down to the Hz or kHz levels would require an improved FTIR reference laser with matching line widths.

Additionally, the measurements show the effect of periodic modulations akin to the dither lock method used previously for RIN suppression of the DFG setup on the Mid-IR frequency comb's optical spectrum. These modulations introduce sidebands to the frequency comb, leading to line broadening negatively affecting spectroscopic applications of the Mid-IR comb. Compared to that, the free-running state of the DFG setup and also the novel interferometric RIN suppression method, specifically developed to combat these sidebands, do not exhibit such an effect. Together with the results from last chapter, these results show that the presented Mid-IR comb would be capable of spectroscopy at a high resolution, running long-term stable as enabled by the interferometric RIN stabilization method developed for this work. However, while the long-term stability of the comb (over typical spectroscopy measurement durations) has been shown in this work, a proof of the usability of the setup for comb spectroscopy with resolutions below previous measurements (as shown in [47]) is still pending.

The next, final, chapter serves to summarize the entire thesis in a few pages, and to provide an outlook into two exciting spectroscopic experiments that are planned for the future of the setup.

5 Conclusion and outlook

To summarize this work, we proved that the DFG approach to Mid-IR frequency comb generation based on Raman SSFS is able to generate narrow comb lines on a sub-Hz level relative to the comb's optical reference for high-resolution spectroscopy. In the past, this was already shown for Raman SSFS itself [35], however this work is the first time this property was shown for a DFG comb using this mechanism for seed generation.

This Mid-IR comb is based on an Yb:fiber frequency comb operating at a repetition rate of 151.65 MHz and a central wavelength of 1060 nm with output powers of 1.5 W which is split in pump and seed beams. The seed beam is coupled into a HNLF for the Raman SSFS to provide the lower frequency photons for the DFG process to generate Mid-IR radiation tunable between 3 to 5 µm with output powers of up to 20 mW. The pump beam passes a voltage-controlled delay stage for setting the pump and seed beams temporal overlap. This overlap is established and stabilized using an interferometric method developed during this thesis to a narrow region in the relative pump/seed delay around perfect overlap with significantly suppressed RIN in the Mid-IR output compared to surrounding regions. This method replaces a dither locking method implemented previously at this setup which uses a modulation of the pump/seed delay and lock-in amplification to stabilize the delay to this minimum [46, 47]. While this method provides long-term stable and effective RIN suppression, analyzing spectroscopic measurements using this method revealed an unexpected broadening of the Mid-IR comb's line width [47]. This led to further numerical investigation of the used modulation. It is shown that this modulation does introduce sidebands to the optical frequency comb at the modulations frequency, which could have lead to a lowered effective resolution in the measured spectra. It is also shown that the new interferometric and modulation-free method achieves a similar level of long-term RIN suppression as the dither lock by comparing spectral measurements taken with both methods over typical long-term experiment durations.

To investigate the line width of the Mid-IR frequency comb, a heterodyne beat between the second harmonic of the Mid-IR comb set to about 4 µm and a Tm:fiber frequency comb at about 2 µm with a repetition rate of 379.125 MHz is performed. Both frequency comb lasers are referenced to the same CW NPRO reference laser at 1064 nm with an optical line width of about 1 kHz to measure the relative line width between both combs. This setup can be used to characterize comb line broadening caused by the DFG setup in addition to the sidebands caused by the dither lock. For the Tm:fiber comb, additional spectral broadening of the comb and subsequent frequency doubling is needed to achieve spectral overlap with the reference laser. A ratio of 2.5 between the two combs' repetition

rates ensures regular interference between both combs' output pulses, resulting in a stable heterodyne beat signal.

This experiment proves that by dithering the temporal pump/seed overlap sidebands are introduced to the frequency comb lines in agreement with numerical simulations modelling this behaviour. Most importantly, it was found that the Mid-IR frequency comb exhibits a narrow line width, as characterized by the low phase noise of the measured heterodyne beat between its second harmonic and the Tm:fiber comb. The integrated phase noise for frequencies between 1 Hz and 1 MHz has been measured to be 368.1 mrad for the free-running, unlocked DFG setup, and 327.8 mrad for the interferometrically locked source. Both of these results show a sub-Hz line width relative to the Tm:fiber reference comb and thus to the common NPRO reference laser. To the knowledge of the author, this is the first time a relative line width at this low level has been measured for DFG sources using Raman SSFS in HNLFs for seed pulse generation. The resulting frequency comb for this source thus shows similar results than reported for DFG sources based on generating the pump beam from the seed via blue-shifting [32–34] and significantly more complex OPOs [25–30].

5.1 Outlook

While the achieved optical line widths with this Mid-IR frequency comb and the novel interferometric locking scheme are excellent results, some aspects about this Mid-IR frequency comb could still be improved for future experiments, leading to better sensitivity or more flexibility of the frequency comb.

One aspect that might become important for future experiments is its beam quality. In this work, an M^2 value between 3 and 3.5 was measured for the Mid-IR beam. While the source provides high output powers near 20 mW, this high value required spacial filtering of the beam to achieve high-quality Mid-IR spectral measurements using the FTIR, losing some of this optical power. However, planned future experiments require either focusing down the light into a small cavity or long-distance transfer through gas cells to acquire enough absorption for measurements, where a beam with a high M^2 might cause issues with either recollimation of the beam or its transport through the cell.

Another aspect which could enhance the usability of the frequency comb is an upgraded control system similar to the laser system reported by fellow group members in [90, 91]. This system provides external control of the comb stabilization frequencies based on FPGAs and the PyRPL library [92]. Implementing this system together with the Distributed Object Oriented Control System (DOOCS) developed DESY-internally [93] and an upgrade to the spectrometers DAQ, this could allow for a highly automatized and integrated

measurement system. This system could run unattended for long-term duration experiments and could be fully scripted externally to run pre-defined measurement programs for example at different repetition rates for sub-nominal resolution.

Over the course of this work, two different follow-up experiments using the capabilities of the Mid-IR frequency comb setup have been planned for possible future implementation. One experiment follows up on the groundwork laid down in references [14, 48, 94]. In these works, the hyperfine structure line lists of both ammonia (NH_3) and water (H_2O) were calculated theoretically, in addition to room-temperature measurements of NH_3 absorption spectra near 4 µm with pressures down to 10 mbar. These two molecules are interesting cases for applying a high-resolution frequency comb as both show two isomers differing in the nuclear spin of the hydrogen nuclei surrounding the central nitrogen or oxygen atoms. These *para* and *ortho* isomers exhibit slightly different properties in their vibrational energy levels and their chemistry [95, 96], but transitions between para and ortho states are forbidden due to the nuclear spin dynamics of the molecules. This results in the corresponding line intensities to become orders of magnitude less pronounced than for transitions conserving the nuclear spins of the hydrogen atoms, but they are predicted to still be within detection range for high-resolution, high-sensitivity Mid-IR frequency combs. In order to perform these measurements the implementation of a liquid nitrogen-cooled cryostat coolable down to 77 K is planned to gradually lower the temperature and pressure of NH_3 molecules [48]. This reduces the influence of both Doppler and pressure line broadenings significantly in order to separate adjacent transitions easier, in addition to a higher population of the vibration ground states for higher absorption. Furthermore, the cryostat housing allows for the implementation of three-pass and later Herriott-type multipass cells to significantly increase the interaction length of the Mid-IR comb with the molecules to up to 10 m, increasing the absorption of relevant transitions even further. The cryostat for this setup has already been designed, and the setup is estimated to allow measurements of absorption line intensities down to 10×10^{-28} cm per molecule.

A different experiment further in the process of implementation is the measurement of hybrid light-matter states. In this project, a molecule is brought inside a tunable optical high-finesse cavity with its fundamental mode close to an absorption line within this molecule [97]. By illuminating the filled cavity, the two quantum-mechanical systems become strongly coupled to each other, leading to a constant energy exchange between excited molecules and photons in the cavity. This exchanges causes new hybridized states between cavity and molecule to form which are called polaritons with new energy levels depending on the cavity detuning relative to the molecular absorption [98–100]. To the knowledge of the author such polaritonic systems have only been measured using low-coherence thermal light sources, allowing for low-finesse cavities only. Using a coherent frequency comb instead allows the use of highly-reflective mirrors for these cavities, increasing their finesse and the achievable coupling between the two states significantly.

For the planned experiment, carbon disulfide (CS_2, a liquid at room-temperature and -pressure) will be used inside such a cavity, which exhibits a strong and isolated vibrational mode suitable for this type of experiment near 6.7 µm [101]. As the used PPLN crystal for the Mid-IR comb becomes intransparent near 5.5 µm, a cadmium silicon phosphide ($CdSiP_2$) (CSP) crystal will be used instead, which is commonly used for frequency conversion to the longer Mid-IR wavelengths [102]. This project has been funded in 2020 as a PIER Seed Project [97] and was supported in 2022 by DESY summer student Yanqiu "Kate" Zhao from the University of Stuttgart. Her task during this project was to set up the cavity and test it in a conventional thermal FTIR setup guided by the author. These experiments were highly useful in determining further improvements to the cavity itself before implementing it in the Mid-IR frequency comb for the high-resolution experiments.

In the end, the presented Mid-IR frequency comb was shown to be an excellent tool with high potential for high-precision spectroscopy as the given experimental ideas show. We showed for the first time that a Raman SSFS-based DFG setup can generate narrow comb lines on a similar level as its driving laser system, being as capable as OPOs and blue-shift based DFG setups. While doing so, our chosen approach is significantly simpler to implement than both of these schemes, which both require further mechanisms for their setup and operation. In addition to this, the interferometric stabilization scheme developed for this Mid-IR frequency comb can easily be adapted for other setups where temporal overlap between two beam paths is critical and interference is available.

Appendices

A Tm:fiber comb red-shifting, HNLF length optimization

Here, the separate spectra for the HNLF fiber length optimization is shown that is earlier referenced in Section 4.2.1. The up to 1.5 W in output power from amplifier 2 of the Tm:fiber laser comb are first coupled into a 1 cm long piece of SMF-28 fiber using a lens with $f = 11$ mm focal length and a 3D stage (Thorlabs Nanomax series). This fiber has a larger core diameter than the actual HNLF (Sumitomo HNDS1614A-10-4-3) for easier coupling. To reduce back reflections, the input is cleaved at an angle of 8°. Both fibers are spliced together using a field splicer (Fujikura 70S), the resulting splice has around 13 % loss. Over the course of this measurement series, the fiber is cleaved repeatedly to shorten its length. The output of the fiber then shines onto the input of a Near-IR spectrometer (OceanOptics NIRQuest 512, range of 1890 to 2145 nm). In between measurements, the fiber output and spectrometer were not set exactly the same as before, so the changes between spectra only show a qualitative change, mainly the solitons center wavelengths. At 13 cm the spectrometer was also changed in height, decreasing the interference fringes and changing the relative amplitude between different wavelengths. Before this change, the long wavelength solitons show to significantly stronger signal than the central 1950 nm peaks, while following this the central peak were stronger. For compensation, the exposure time has been changed accordingly. The measurements are shown in Figures A.1 to A.7.

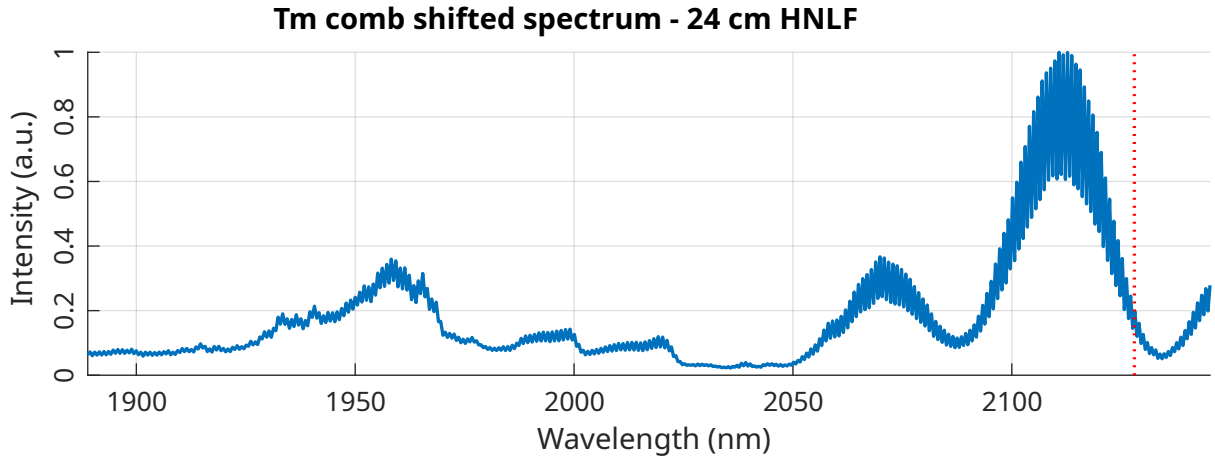

Figure A.1: Optical spectrum after coupling the output of amplifier 2 of the Tm:fiber comb into a highly nonlinear fiber (Sumitomo HNDS1614A-10-4-3) of 24 cm length. A line at 2128 nm shows the target wavelength required for the SHG at 1064 nm required for beating with the NPRO reference.

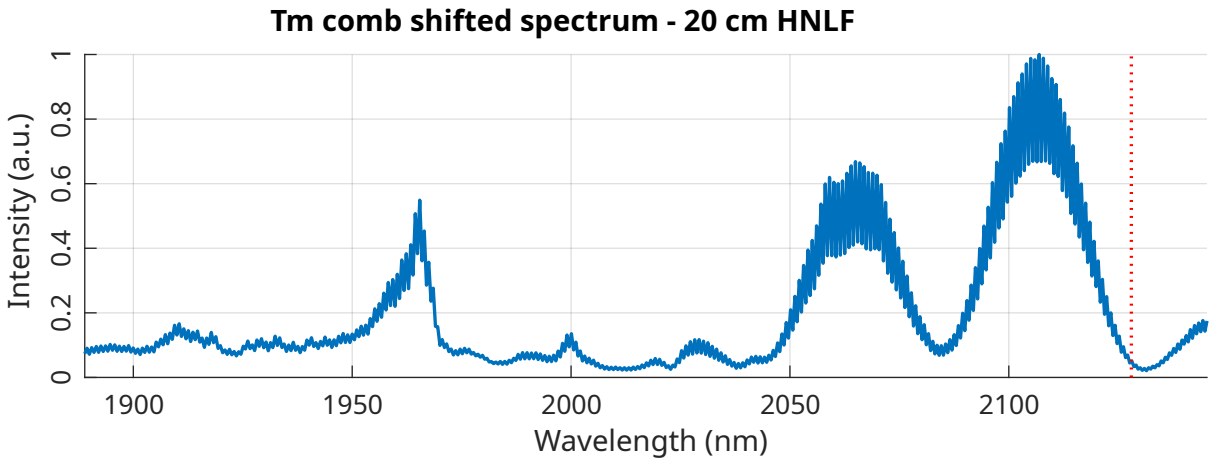

Figure A.2: Optical spectrum after cutting down the HNLF to 20 cm length.

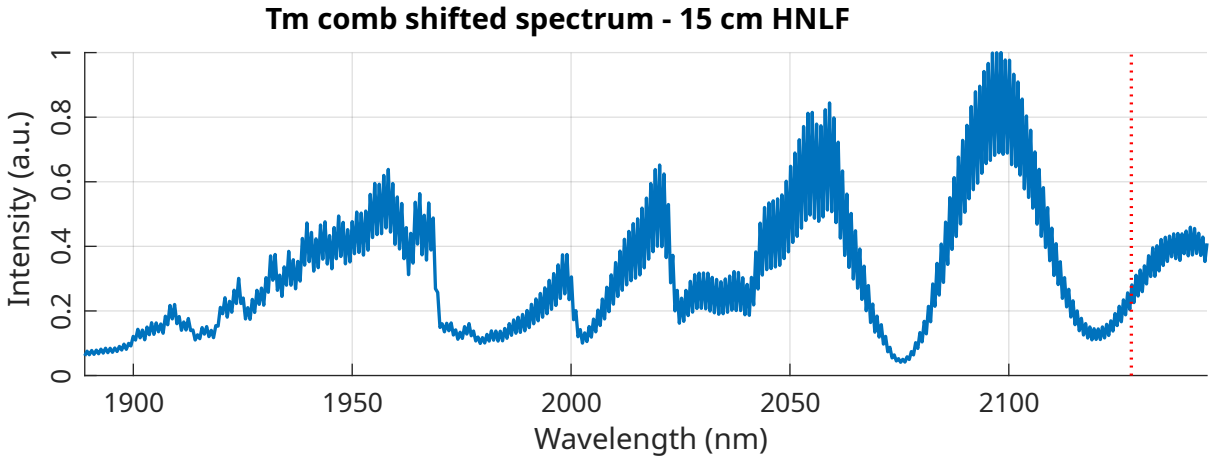

Figure A.3: Optical spectrum after cutting down the HNLF to 15 cm length.

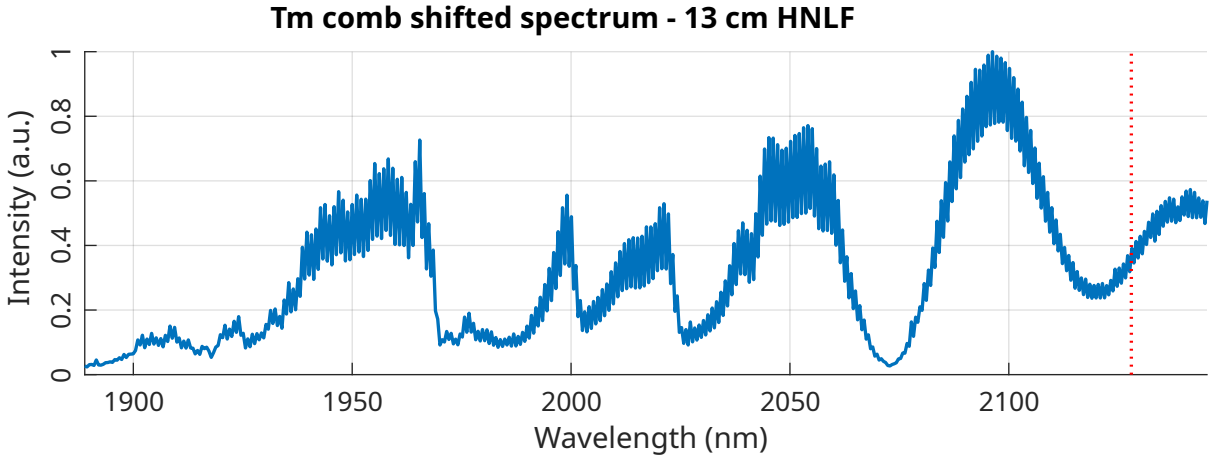

Figure A.4: Optical spectrum after cutting down the HNLF to 13 cm length.

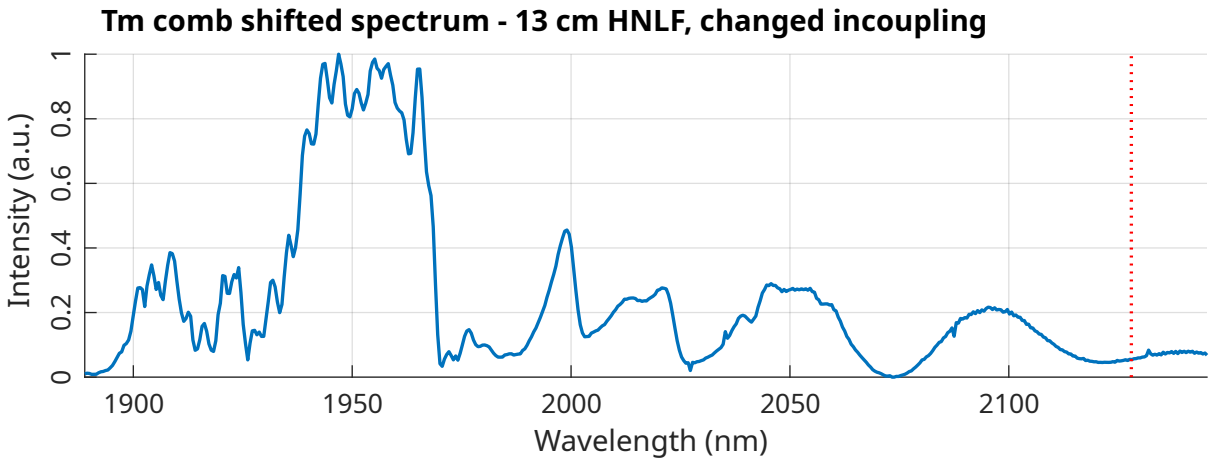

Figure A.5: Optical spectrum after cutting down the HNLF to 13 cm length, and after changing the height of the spectrometer.

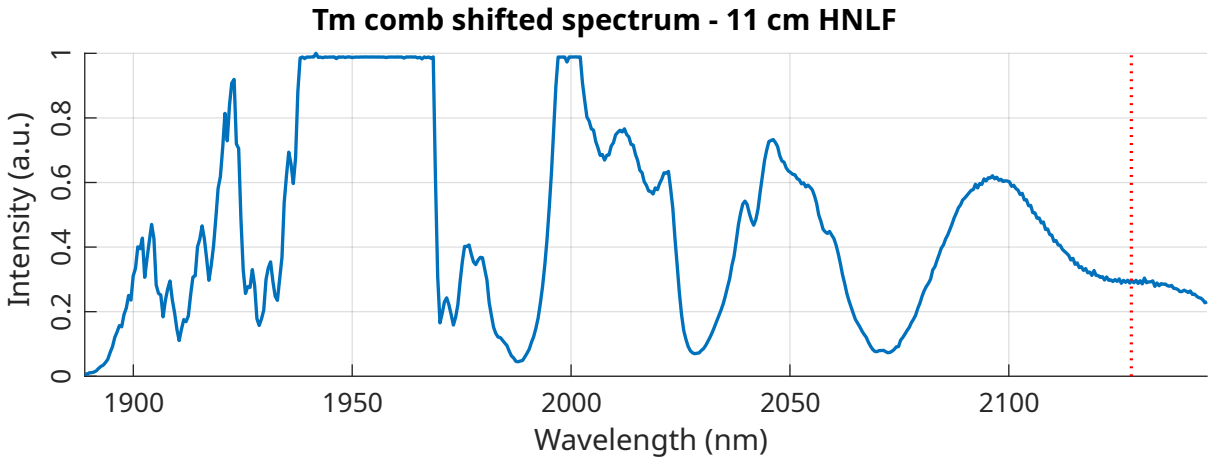

Figure A.6: Optical spectrum after cutting down the HNLF to 11 cm length. This fiber length has been selected for continuing with the generation of the second harmonic and later referencing to the NPRO.

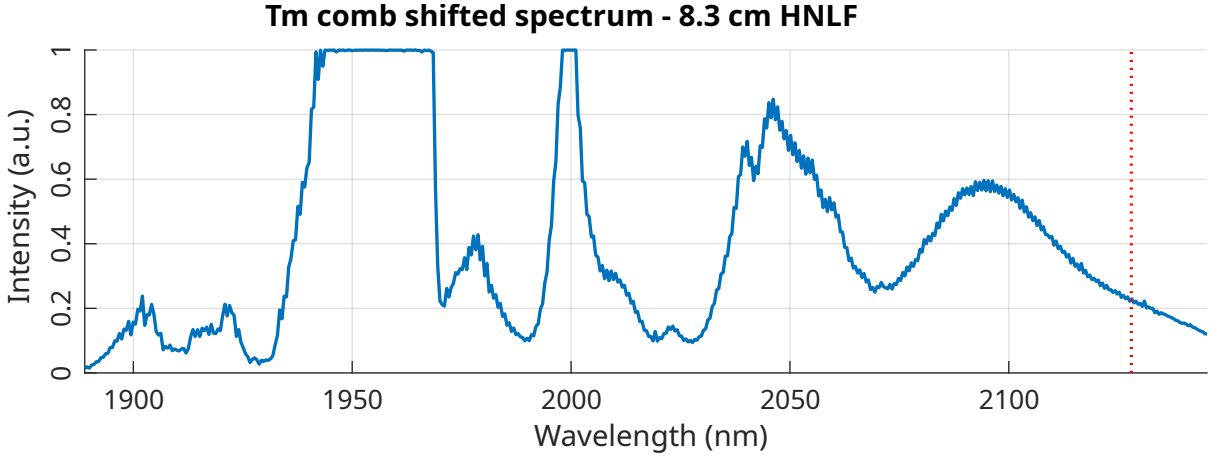

Figure A.7: Optical spectrum after cutting down the HNLF to 8.3 cm length.

B Lists

B.1 References

[1] T. W. Hänsch. "Nobel Lecture: Passion for precision". In: *Rev. Mod. Phys.* 78 (4 Nov. 2006), pp. 1297–1309. DOI: 10.1103/RevModPhys.78.1297. URL: https://link.aps.org/doi/10.1103/RevModPhys.78.1297.

[2] N. Picqué and T. W. Hänsch. "Frequency comb spectroscopy". In: *Nature Photonics* 13.3 (Mar. 2019), pp. 146–157. ISSN: 1749-4893. DOI: 10.1038/s41566-018-0347-5. URL: https://doi.org/10.1038/s41566-018-0347-5.

[3] H. Schnatz et al. "First Phase-Coherent Frequency Measurement of Visible Radiation". In: *Phys. Rev. Lett.* 76 (1 Jan. 1996), pp. 18–21. DOI: 10.1103/PhysRevLett.76.18. URL: https://link.aps.org/doi/10.1103/PhysRevLett.76.18.

[4] S. A. Diddams, K. Vahala, and T. Udem. "Optical frequency combs: Coherently uniting the electromagnetic spectrum". In: *Science* 369.6501 (2020), eaay3676. DOI: 10.1126/science.aay3676. eprint: https://www.science.org/doi/pdf/10.1126/science.aay3676. URL: https://www.science.org/doi/abs/10.1126/science.aay3676.

[5] J. Ye and S. Cundiff. *Femtosecond Optical Frequency Comb: Principle, Operation and Applications*. Springer US, 2006. ISBN: 9780387237916. URL: https://books.google.de/books?id=Myd2VdEUm-0C.

[6] S. A. Diddams. "The evolving optical frequency comb (Invited)". In: *J. Opt. Soc. Am. B* 27.11 (Nov. 2010), B51–B62. DOI: 10.1364/JOSAB.27.000B51. URL: https://opg.optica.org/josab/abstract.cfm?URI=josab-27-11-B51.

[7] M.-G. Suh and K. J. Vahala. "Soliton microcomb range measurement". In: *Science* 359.6378 (2018), pp. 884–887. DOI: 10.1126/science.aao1968. eprint: https://www.science.org/doi/pdf/10.1126/science.aao1968. URL: https://www.science.org/doi/abs/10.1126/science.aao1968.

[8] P. Trocha et al. "Ultrafast optical ranging using microresonator soliton frequency combs". In: *Science* 359.6378 (2018), pp. 887–891. DOI: 10.1126/science.aao3924. eprint: https://www.science.org/doi/pdf/10.1126/science.aao3924. URL: https://www.science.org/doi/abs/10.1126/science.aao3924.

[9] S. Bize et al. "Testing the Stability of Fundamental Constants with the $^{199}Hg^{+}$ Single-Ion Optical Clock". In: *Phys. Rev. Lett.* 90 (15 Apr. 2003), p. 150802. DOI: 10.1103/PhysRevLett.90.150802. URL: https://link.aps.org/doi/10.1103/PhysRevLett.90.150802.

[10] M. Fischer et al. “New Limits on the Drift of Fundamental Constants from Laboratory Measurements”. In: *Phys. Rev. Lett.* 92 (23 June 2004), p. 230802. DOI: 10.1103/PhysRevLett.92.230802. URL: https://link.aps.org/doi/10.1103/PhysRevLett.92.230802.

[11] T. M. Fortier et al. “Precision Atomic Spectroscopy for Improved Limits on Variation of the Fine Structure Constant and Local Position Invariance”. In: *Phys. Rev. Lett.* 98 (7 Feb. 2007), p. 070801. DOI: 10.1103/PhysRevLett.98.070801. URL: https://link.aps.org/doi/10.1103/PhysRevLett.98.070801.

[12] A. Schliesser, N. Picqué, and T. W. Hänsch. “Mid-infrared frequency combs”. In: *Nature Photonics* 6.7 (July 2012), pp. 440–449. ISSN: 1749-4893. DOI: 10.1038/nphoton.2012.142. URL: https://doi.org/10.1038/nphoton.2012.142.

[13] K. C. Cossel et al. “Gas-phase broadband spectroscopy using active sources: progress, status, and applications (Invited)”. In: *J. Opt. Soc. Am. B* 34.1 (Jan. 2017), pp. 104–129. DOI: 10.1364/JOSAB.34.000104. URL: https://opg.optica.org/josab/abstract.cfm?URI=josab-34-1-104.

[14] G. Yang et al. “Self-broadening and self-shift in the $3\nu 2$ band of ammonia from mid-infrared-frequency-comb spectroscopy”. In: *Journal of Molecular Spectroscopy* (2023), p. 111744. ISSN: 0022-2852. DOI: https://doi.org/10.1016/j.jms.2023.111744. URL: https://www.sciencedirect.com/science/article/pii/S0022285223000097.

[15] A. Foltynowicz et al. “Cavity-enhanced optical frequency comb spectroscopy in the mid-infrared application to trace detection of hydrogen peroxide”. In: *Applied Physics B* 110.2 (Feb. 2013), pp. 163–175. ISSN: 1432-0649. DOI: 10.1007/s00340-012-5024-7. URL: https://doi.org/10.1007/s00340-012-5024-7.

[16] Q. Liang et al. “Ultrasensitive multispecies spectroscopic breath analysis for real-time health monitoring and diagnostics”. In: *Proceedings of the National Academy of Sciences* 118.40 (2021), e2105063118. DOI: 10.1073/pnas.2105063118. eprint: https://www.pnas.org/doi/pdf/10.1073/pnas.2105063118. URL: https://www.pnas.org/doi/abs/10.1073/pnas.2105063118.

[17] Q. Liang et al. “Breath analysis by ultra-sensitive broadband laser spectroscopy detects SARS-CoV-2 infection”. In: *Journal of Breath Research* 17.3 (Apr. 2023), p. 036001. DOI: 10.1088/1752-7163/acc6e4. URL: https://dx.doi.org/10.1088/1752-7163/acc6e4.

[18] J. Ma et al. “Review of mid-infrared mode-locked laser sources in the 2.0 µm–3.5 µm spectral region”. In: *Applied Physics Reviews* 6.2 (June 2019), p. 021317. ISSN: 1931-9401. DOI: 10.1063/1.5037274. eprint: https://pubs.aip.org/aip/apr/article-pdf/doi/10.1063/1.5037274/14578088/021317_1_online.pdf. URL: https://doi.org/10.1063/1.5037274.

[19] B. Bernhardt et al. "Mid-infrared dual-comb spectroscopy with 2.4 μm Cr2+:ZnSe femtosecond lasers". In: *Applied Physics B* 100.1 (July 2010), pp. 3–8. ISSN: 1432-0649. DOI: 10.1007/s00340-010-4080-0. URL: https://doi.org/10.1007/s00340-010-4080-0.

[20] S. Vasilyev et al. "Middle-IR frequency comb based on Cr:ZnS laser". In: *Opt. Express* 27.24 (Nov. 2019), pp. 35079–35087. DOI: 10.1364/OE.27.035079. URL: https://opg.optica.org/oe/abstract.cfm?URI=oe-27-24-35079.

[21] S. Vasilyev et al. "Ultrafast Nonlinear Optics and Mid-IR Frequency Comb Generation With Mode-Locked Cr:ZnS lasers". In: *Conference on Lasers and Electro-Optics*. Optica Publishing Group, 2022, SM2O.3. DOI: 10.1364/CLEO_SI.2022.SM2O.3. URL: https://opg.optica.org/abstract.cfm?URI=CLEO_SI-2022-SM2O.3.

[22] S. Vasilyev et al. "Dual Frequency-Comb Spectroscopy with Cr:ZnS Lasers". In: *Laser Congress 2021 (ASSL,LAC)*. Optica Publishing Group, 2021, ATu3A.2. DOI: 10.1364/ASSL.2021.ATu3A.2. URL: https://opg.optica.org/abstract.cfm?URI=ASSL-2021-ATu3A.2.

[23] A. V. Pushkin et al. "Femtosecond graphene mode-locked Fe:ZnSe laser at 4.4 µm". In: *Opt. Lett.* 45.3 (Feb. 2020), pp. 738–741. DOI: 10.1364/OL.384300. URL: https://opg.optica.org/ol/abstract.cfm?URI=ol-45-3-738.

[24] Z. Chang et al. "Intense infrared lasers for strong-field science". In: *Adv. Opt. Photon.* 14.4 (Dec. 2022), pp. 652–782. DOI: 10.1364/AOP.454797. URL: https://opg.optica.org/aop/abstract.cfm?URI=aop-14-4-652.

[25] F. Adler et al. "Phase-stabilized, 1.5 W frequency comb at 2.8–4.8 μm". In: *Opt. Lett.* 34.9 (May 2009), pp. 1330–1332. DOI: 10.1364/OL.34.001330. URL: https://opg.optica.org/ol/abstract.cfm?URI=ol-34-9-1330.

[26] N. Leindecker et al. "Broadband degenerate OPO for mid-infrared frequency comb generation". In: *Opt. Express* 19.7 (Mar. 2011), pp. 6296–6302. DOI: 10.1364/OE.19.006296. URL: https://opg.optica.org/oe/abstract.cfm?URI=oe-19-7-6296.

[27] A. Marandi et al. "Coherence properties of a broadband femtosecond mid-IR optical parametric oscillator operating at degeneracy". In: *Opt. Express* 20.7 (Mar. 2012), pp. 7255–7262. DOI: 10.1364/OE.20.007255. URL: https://opg.optica.org/oe/abstract.cfm?URI=oe-20-7-7255.

[28] K. F. Lee et al. "Mid-IR Frequency Comb with Sub-Hertz Residual Linewidth From a Doubly-Resonant OPGaAs OPO". In: *2013 Conference on Lasers and Electro-Optics Pacific Rim*. Optica Publishing Group, 2013, TuC1_4. URL: https://opg.optica.org/abstract.cfm?URI=CLEOPR-2013-TuC1_4.

[29] K. F. Lee et al. “Carrier envelope offset frequency of a doubly resonant, nondegenerate, mid-infrared GaAs optical parametric oscillator”. In: *Opt. Lett.* 38.8 (Apr. 2013), pp. 1191–1193. DOI: 10.1364/OL.38.001191. URL: https://opg.optica.org/ol/abstract.cfm?URI=ol-38-8-1191.

[30] K. F. Lee et al. “Midinfrared frequency comb from self-stable degenerate GaAs optical parametric oscillator”. In: *Opt. Express* 23.20 (Oct. 2015), pp. 26596–26603. DOI: 10.1364/OE.23.026596. URL: https://opg.optica.org/oe/abstract.cfm?URI=oe-23-20-26596.

[31] M. Zimmermann et al. “Optical clockwork with an offset-free difference-frequency comb: accuracy of sum- and difference-frequency generation”. In: *Opt. Lett.* 29.3 (Feb. 2004), pp. 310–312. DOI: 10.1364/OL.29.000310. URL: https://opg.optica.org/ol/abstract.cfm?URI=ol-29-3-310.

[32] F. C. Cruz et al. “Mid-infrared optical frequency combs based on difference frequency generation for molecular spectroscopy”. In: *Opt. Express* 23.20 (Oct. 2015), pp. 26814–26824. DOI: 10.1364/OE.23.026814. URL: https://opg.optica.org/oe/abstract.cfm?URI=oe-23-20-26814.

[33] D. L. Maser et al. “Coherent frequency combs for spectroscopy across the 3–5 µm region”. In: *Applied Physics B* 123.5 (Apr. 2017), p. 142. ISSN: 1432-0649. DOI: 10.1007/s00340-017-6714-y. URL: https://doi.org/10.1007/s00340-017-6714-y.

[34] C. Cleft et al. “Mid-IR DFG frequency combs with high mode power and 1.5 Hz linewidth using femtosecond fiber laser systems”. In: *Conference on Lasers and Electro-Optics*. Optica Publishing Group, 2020, SF2G.1. DOI: 10.1364/CLEO_SI.2020.SF2G.1. URL: https://opg.optica.org/abstract.cfm?URI=CLEO_SI-2020-SF2G.1.

[35] A. Ruehl et al. “Ultrabroadband coherent supercontinuum frequency comb”. In: *Phys. Rev. A* 84 (1 July 2011), p. 011806. DOI: 10.1103/PhysRevA.84.011806. URL: https://link.aps.org/doi/10.1103/PhysRevA.84.011806.

[36] A. M. Heidt et al. “Coherent octave spanning near-infrared and visible supercontinuum generation in all-normal dispersion photonic crystal fibers”. In: *Opt. Express* 19.4 (Feb. 2011), pp. 3775–3787. DOI: 10.1364/OE.19.003775. URL: https://opg.optica.org/oe/abstract.cfm?URI=oe-19-4-3775.

[37] A. Ruehl et al. “Widely-tunable mid-infrared frequency comb source based on difference frequency generation”. In: *Opt. Lett.* 37.12 (June 2012), pp. 2232–2234. DOI: 10.1364/OL.37.002232. URL: https://opg.optica.org/ol/abstract.cfm?URI=ol-37-12-2232.

[38] M. Seidel et al. “Multi-watt, multi-octave, mid-infrared femtosecond source”. In: *Science Advances* 4.4 (2018), eaaq1526. DOI: 10.1126/sciadv.aaq1526. eprint: https://www.science.org/doi/pdf/10.1126/sciadv.aaq1526. URL: https://www.science.org/doi/abs/10.1126/sciadv.aaq1526.

[39] J. Zhang et al. “Multi-mW, few-cycle mid-infrared continuum spanning from 500 to 2250 1/cm”. In: *Light: Science & Applications* 7.2 (Feb. 2018), pp. 17180–17180. ISSN: 2047-7538. DOI: 10.1038/lsa.2017.180. URL: https://doi.org/10.1038/lsa.2017.180.

[40] K. Krzempek et al. “Stabilized all-fiber source for generation of tunable broadband fCEO-free mid-IR frequency comb in the 7 – 9 µm range”. In: *Opt. Express* 27.26 (Dec. 2019), pp. 37435–37445. DOI: 10.1364/OE.27.037435. URL: https://opg.optica.org/oe/abstract.cfm?URI=oe-27-26-37435.

[41] A. Hjältén et al. “Optical frequency comb Fourier transform spectroscopy of 14N216O at 7.8 μm”. In: *Journal of Quantitative Spectroscopy and Radiative Transfer* 271 (2021), p. 107734. ISSN: 0022-4073. DOI: https://doi.org/10.1016/j.jqsrt.2021.107734. URL: https://www.sciencedirect.com/science/article/pii/S0022407321002272.

[42] T. W. Neely, T. A. Johnson, and S. A. Diddams. “High-power broadband laser source tunable from 3.0 μm to 4.4 μm based on a femtosecond Yb:fiber oscillator”. In: *Opt. Lett.* 36.20 (Oct. 2011), pp. 4020–4022. DOI: 10.1364/OL.36.004020. URL: https://opg.optica.org/ol/abstract.cfm?URI=ol-36-20-4020.

[43] L. Jin et al. “3.1–5.2 μm Coherent MIR Frequency Comb Based on Yb-Doped Fiber Laser”. In: *IEEE Journal of Selected Topics in Quantum Electronics* 24.3 (2018), pp. 1–7. DOI: 10.1109/JSTQE.2017.2759258.

[44] G. Soboń et al. “High-power frequency comb source tunable from 2.7 to 4.2 μm based on difference frequency generation pumped by an Yb-doped fiber laser”. In: *Opt. Lett.* 42.9 (May 2017), pp. 1748–1751. DOI: 10.1364/OL.42.001748. URL: https://opg.optica.org/ol/abstract.cfm?URI=ol-42-9-1748.

[45] A. Gambetta et al. “Direct phase-locking of a 8.6 μm quantum cascade laser to a mid-IR optical frequency comb: application to precision spectroscopy of N_2O”. In: *Opt. Lett.* 40.3 (Feb. 2015), pp. 304–307. DOI: 10.1364/OL.40.000304. URL: https://opg.optica.org/ol/abstract.cfm?URI=ol-40-3-304.

[46] V. S. de Oliveira et al. “Intensity noise optimization of a mid-infrared frequency comb difference-frequency generation source”. In: *Opt. Lett.* 45.7 (Apr. 2020), pp. 1914–1917. DOI: 10.1364/OL.391195. URL: https://opg.optica.org/ol/abstract.cfm?URI=ol-45-7-1914.

[47] V. S. de Oliveira. “Direct frequency comb spectroscopy of carbon monoxide in the mid-infrared”. PhD thesis. University of Hamburg, 2018.

[48] G. Yang. “Theoretical and experimental investigation of nuclear spin dynamics in water and ammonia”. PhD thesis. University of Hamburg, 2022.

[49] U. Keller. *Ultrafast Lasers: A Comprehensive Introduction to Fundamental Principles with Practical Applications*. Graduate Texts in Physics. Springer International Publishing, 2022. ISBN: 9783030825317. URL: https://books.google.de/books?id=jjuEzgEACAAJ.

[50] A. Weiner. *Ultrafast Optics*. Wiley Series in Pure and Applied Optics. Wiley, 2011. ISBN: 9781118211472. URL: https://books.google.de/books?id=fhohaV7wJbYC.

[51] N. R. Newbury and W. C. Swann. “Low-noise fiber-laser frequency combs (Invited)”. In: *J. Opt. Soc. Am. B* 24.8 (Aug. 2007), pp. 1756–1770. DOI: 10.1364/JOSAB.24.001756. URL: https://opg.optica.org/josab/abstract.cfm?URI=josab-24-8-1756.

[52] R. Boyd. *Nonlinear Optics*. Elsevier Science, 2020. ISBN: 9780128110027. URL: https://books.google.de/books?id=ynzZDwAAQBAJ.

[53] D. Eimerl et al. “Optical, mechanical, and thermal properties of barium borate”. In: *Journal of Applied Physics* 62.5 (Sept. 1987), pp. 1968–1983. ISSN: 0021-8979. DOI: 10.1063/1.339536. eprint: https://pubs.aip.org/aip/jap/article-pdf/62/5/1968/10571657/1968_1_online.pdf. URL: https://doi.org/10.1063/1.339536.

[54] J. M. Dudley, G. Genty, and S. Coen. “Supercontinuum generation in photonic crystal fiber”. In: *Rev. Mod. Phys.* 78 (4 Oct. 2006), pp. 1135–1184. DOI: 10.1103/RevModPhys.78.1135. URL: https://link.aps.org/doi/10.1103/RevModPhys.78.1135.

[55] F. M. Mitschke and L. F. Mollenauer. “Discovery of the soliton self-frequency shift”. In: *Opt. Lett.* 11.10 (Oct. 1986), pp. 659–661. DOI: 10.1364/OL.11.000659. URL: https://opg.optica.org/ol/abstract.cfm?URI=ol-11-10-659.

[56] J. P. Gordon. “Theory of the soliton self-frequency shift”. In: *Opt. Lett.* 11.10 (Oct. 1986), pp. 662–664. DOI: 10.1364/OL.11.000662. URL: https://opg.optica.org/ol/abstract.cfm?URI=ol-11-10-662.

[57] N. Newbury and B. Washburn. “Theory of the frequency comb output from a femtosecond fiber laser”. In: *IEEE Journal of Quantum Electronics* 41.11 (2005), pp. 1388–1402. DOI: 10.1109/JQE.2005.857657.

[58] W. Lewandowski, J. Azoubib, and W. Klepczynski. “GPS: primary tool for time transfer”. In: *Proceedings of the IEEE* 87.1 (1999), pp. 163–172. DOI: 10.1109/5.736348.

[59] P. Zhang et al. “Combining GPS, BeiDou, and Galileo Satellite Systems for Time and Frequency Transfer Based on Carrier Phase Observations”. In: *Remote Sensing* 10.2 (2018). ISSN: 2072-4292. DOI: 10.3390/rs10020324. URL: https://www.mdpi.com/2072-4292/10/2/324.

[60] M. Germann et al. “A methane line list with sub-MHz accuracy in the 1250 to 1380 cm^{-1} range from optical frequency comb Fourier transform spectroscopy”. In: *Journal of Quantitative Spectroscopy and Radiative Transfer* 288 (2022), p. 108252. ISSN: 0022-4073. DOI: https://doi.org/10.1016/j.jqsrt.2022.108252. URL: https://www.sciencedirect.com/science/article/pii/S002240732200187X.

[61] I. Sadiek et al. “Line positions and intensities of the ν4 band of methyl iodide using mid-infrared optical frequency comb Fourier transform spectroscopy”. In: *Journal of Quantitative Spectroscopy and Radiative Transfer* 255 (2020), p. 107263. ISSN: 0022-4073. DOI: https://doi.org/10.1016/j.jqsrt.2020.107263. URL: https://www.sciencedirect.com/science/article/pii/S0022407320305318.

[62] A. Hjältén, A. Foltynowicz, and I. Sadiek. “Line positions and intensities of the ν1 band of 12CH3I using mid-infrared optical frequency comb Fourier transform spectroscopy”. In: *Journal of Quantitative Spectroscopy and Radiative Transfer* 306 (2023), p. 108646. ISSN: 0022-4073. DOI: https://doi.org/10.1016/j.jqsrt.2023.108646. URL: https://www.sciencedirect.com/science/article/pii/S0022407323001644.

[63] R. Paschotta. “Noise of mode-locked lasers (Part I): numerical model”. In: *Applied Physics B* 79.2 (July 2004), pp. 153–162. ISSN: 1432-0649. DOI: 10.1007/s00340-004-1547-x. URL: https://doi.org/10.1007/s00340-004-1547-x.

[64] H. Haus and A. Mecozzi. “Noise of mode-locked lasers”. In: *IEEE Journal of Quantum Electronics* 29.3 (1993), pp. 983–996. DOI: 10.1109/3.206583.

[65] R. Scott, C. Langrock, and B. Kolner. “High-dynamic-range laser amplitude and phase noise measurement techniques”. In: *IEEE Journal of Selected Topics in Quantum Electronics* 7.4 (2001), pp. 641–655. DOI: 10.1109/2944.974236.

[66] J. Hall and M. Zhu. “An introduction to phase-stable optical sources”. In: vol. CXVIII. JILA Pub. 4738. North-Holland, 1993.

[67] P. Hamm, R. A. Kaindl, and J. Stenger. “Noise suppression in femtosecond mid-infrared light sources”. In: *Opt. Lett.* 25.24 (Dec. 2000), pp. 1798–1800. DOI: 10.1364/OL.25.001798. URL: https://opg.optica.org/ol/abstract.cfm?URI=ol-25-24-1798.

[68] H. E. Ives. “The Doppler Effect from Moving Mirrors”. In: *J. Opt. Soc. Am.* 30.6 (June 1940), pp. 255–257. DOI: 10.1364/JOSA.30.000255. URL: https://opg.optica.org/abstract.cfm?URI=josa-30-6-255.

[69] A. Parriaux, K. Hammani, and G. Millot. "Electro-optic frequency combs". In: *Adv. Opt. Photon.* 12.1 (Mar. 2020), pp. 223–287. DOI: 10.1364/AOP.382052. URL: https://opg.optica.org/aop/abstract.cfm?URI=aop-12-1-223.

[70] D. Laumer et al. "Sub-Hz relative linewidths from an interferometrically stabilized mid-infrared frequency comb". In: *Opt. Lett.* 48.11 (June 2023), pp. 3055–3058. DOI: 10.1364/OL.491684. URL: https://opg.optica.org/ol/abstract.cfm?URI=ol-48-11-3055.

[71] J. A. D. H. Peter Griffiths. *Fourier Transform Infrared Spectrometry*. 2nd ed. Chemical Analysis: A Series of Monographs on Analytical Chemistry and Its Applications. Wiley-Interscience, 2007. ISBN: 0471194042; 9780471194040. URL: libgen.li/file.php?md5=be35761c8faeb68054ab0b5bb6cc067a.

[72] P. Maslowski et al. "Surpassing the path-limited resolution of Fourier-transform spectrometry with frequency combs". In: *Phys. Rev. A* 93 (2 Feb. 2016), p. 021802. DOI: 10.1103/PhysRevA.93.021802. URL: https://link.aps.org/doi/10.1103/PhysRevA.93.021802.

[73] L. Rutkowski et al. "Optical frequency comb Fourier transform spectroscopy with sub-nominal resolution and precision beyond the Voigt profile". In: *Journal of Quantitative Spectroscopy and Radiative Transfer* 204 (2018), pp. 63–73. ISSN: 0022-4073. DOI: https://doi.org/10.1016/j.jqsrt.2017.09.001. URL: https://www.sciencedirect.com/science/article/pii/S0022407317300201.

[74] U. Hassan and M. S. Anwar. "Reducing noise by repetition: introduction to signal averaging". In: *European Journal of Physics* 31.3 (Mar. 2010), p. 453. DOI: 10.1088/0143-0807/31/3/003. URL: https://dx.doi.org/10.1088/0143-0807/31/3/003.

[75] C. Wan. "Low Noise Frequency Comb Sources Based on Synchronously Pumped Doubly Resonant Optical Parametric Oscillators". PhD thesis. University of Dayton, 2017.

[76] R. Trebino. *Frequency-Resolved Optical Gating: The Measurement of Ultrashort Laser Pulses: The Measurement of Ultrashort Laser Pulses*. Springer US, 2000. ISBN: 9781402070662. URL: https://books.google.de/books?id=yfLIg6E69D8C.

[77] R. Trebino et al. "Measuring ultrashort laser pulses in the time-frequency domain using frequency-resolved optical gating". In: *Review of Scientific Instruments* 68.9 (Sept. 1997), pp. 3277–3295. ISSN: 0034-6748. DOI: 10.1063/1.1148286. eprint: https://pubs.aip.org/aip/rsi/article-pdf/68/9/3277/8811505/3277_1_online.pdf. URL: https://doi.org/10.1063/1.1148286.

[78] S. Suzuki et al. "Highly ytterbium-doped silica fibers with low photo-darkening". In: *Opt. Express* 17.12 (June 2009), pp. 9924–9932. DOI: 10.1364/OE.17.009924. URL: https://opg.optica.org/oe/abstract.cfm?URI=oe-17-12-9924.

[79] T. C. Briles et al. “Simple piezoelectric-actuated mirror with 180 kHz servo bandwidth”. In: *Opt. Express* 18.10 (May 2010), pp. 9739–9746. DOI: 10.1364/OE.18.009739. URL: https://opg.optica.org/oe/abstract.cfm?URI=oe-18-10-9739.

[80] H. R. Telle et al. “Carrier-envelope offset phase control: A novel concept for absolute optical frequency measurement and ultrashort pulse generation”. In: *Applied Physics B* 69.4 (Oct. 1999), pp. 327–332. ISSN: 1432-0649. DOI: 10.1007/s003400050813. URL: https://doi.org/10.1007/s003400050813.

[81] L. Dong, B. K. Thomas, and L. Fu. “Highly nonlinear silica suspended core fibers”. In: *Opt. Express* 16.21 (Oct. 2008), pp. 16423–16430. DOI: 10.1364/OE.16.016423. URL: https://opg.optica.org/oe/abstract.cfm?URI=oe-16-21-16423.

[82] H. W. Icenogle, B. C. Platt, and W. L. Wolfe. “Refractive indexes and temperature coefficients of germanium and silicon”. In: *Appl. Opt.* 15.10 (Oct. 1976), pp. 2348–2351. DOI: 10.1364/AO.15.002348. URL: https://opg.optica.org/ao/abstract.cfm?URI=ao-15-10-2348.

[83] J. H. Scofield. “Frequency-domain description of a lock-in amplifier”. In: *American Journal of Physics* 62.2 (Feb. 1994), pp. 129–133. ISSN: 0002-9505. DOI: 10.1119/1.17629. eprint: https://pubs.aip.org/aapt/ajp/article-pdf/62/2/129/11441741/129_1_online.pdf. URL: https://doi.org/10.1119/1.17629.

[84] F. Herzog et al. “Optical Phase Locking by Local Oscillator Phase Dithering”. In: *IEEE Journal of Quantum Electronics* 42.10 (2006), pp. 973–985. DOI: 10.1109/JQE.2006.881413.

[85] J. Ye et al. “Hyperfine structure and absolute frequency of the 87Rb 5P3/2 state”. In: *Opt. Lett.* 21.16 (Aug. 1996), pp. 1280–1282. DOI: 10.1364/OL.21.001280. URL: https://opg.optica.org/ol/abstract.cfm?URI=ol-21-16-1280.

[86] W. Swann et al. “Fiber-laser frequency combs with subhertz relative linewidths”. In: *Optics Letters* 31 (Nov. 2006), pp. 3046–8. DOI: 10.1364/OL.31.003046.

[87] C.-C. Lee et al. “Frequency comb stabilization with bandwidth beyond the limit of gain lifetime by an intracavity graphene electro-optic modulator”. In: *Opt. Lett.* 37.15 (Aug. 2012), pp. 3084–3086. DOI: 10.1364/OL.37.003084. URL: https://opg.optica.org/ol/abstract.cfm?URI=ol-37-15-3084.

[88] J. Jiang et al. “500 MHz, 58 fs highly coherent Tm fiber soliton laser”. In: *Conference on Lasers and Electro-Optics 2012*. Optica Publishing Group, 2012, CTh5D.7. DOI: 10.1364/CLEO_SI.2012.CTh5D.7. URL: https://opg.optica.org/abstract.cfm?URI=CLEO_SI-2012-CTh5D.7.

[89] M. Delehaye et al. “Residual Phase Noise Measurement of Optical Second Harmonic Generation in PPLN Waveguides”. In: *IEEE Photonics Technology Letters* 29.19 (2017), pp. 1639–1642. DOI: 10.1109/LPT.2017.2741667.

[90] S. Salman et al. “Smart and agile 84 W fs Yb-fiber laser for spectroscopy”. In: *Conference on Lasers and Electro-Optics*. Optica Publishing Group, 2022, SF2M.1. DOI: 10.1364/CLEO_SI.2022.SF2M.1. URL: https://opg.optica.org/abstract.cfm?URI=CLEO_SI-2022-SF2M.1.

[91] Salman, Sarper et al. “Smart and agile 88 W Yb-fiber frequency comb laser”. In: *EPJ Web Conf.* 267 (2022), p. 01057. DOI: 10.1051/epjconf/202226701057. URL: https://doi.org/10.1051/epjconf/202226701057.

[92] L. Neuhaus et al. “PyRPL (Python Red Pitaya Lockbox) — An open-source software package for FPGA-controlled quantum optics experiments”. In: *2017 Conference on Lasers and Electro-Optics Europe & European Quantum Electronics Conference (CLEO/Europe-EQEC)*. 2017, pp. 1–1. DOI: 10.1109/CLEOE-EQEC.2017.8087380.

[93] O. Hensler and K. Rehlich. “DOOCS: A distributed object oriented control system”. In: *15th Conference on Charged Particle Accelerators*. 1996, pp. 308–315.

[94] A. Yachmenev et al. “The nuclear-spin-forbidden rovibrational transitions of water from first principles”. In: *The Journal of Chemical Physics* 156.20 (May 2022), p. 204307. ISSN: 0021-9606. DOI: 10.1063/5.0090771. eprint: https://pubs.aip.org/aip/jcp/article-pdf/doi/10.1063/5.0090771/16544008/204307_1_online.pdf. URL: https://doi.org/10.1063/5.0090771.

[95] A. Kilaj et al. “Observation of different reactivities of para and ortho-water towards trapped diazenylium ions”. In: *Nature Communications* 9.1 (May 2018), p. 2096. ISSN: 2041-1723. DOI: 10.1038/s41467-018-04483-3. URL: https://doi.org/10.1038/s41467-018-04483-3.

[96] A. Faure et al. “Ortho-para selection rules in the gas-phase chemistry of interstellar ammonia”. In: *The Astrophysical Journal Letters* 770.1 (May 2013), p. L2. DOI: 10.1088/2041-8205/770/1/L2. URL: https://dx.doi.org/10.1088/2041-8205/770/1/L2.

[97] M. Seidel. “Mid-infrared Frequency Comb Spectroscopy of Hybrid Light-Matter States”. Accepted proposal for PIER Seed Projects 2020.

[98] J. D. Erwin, M. Smotzer, and J. V. Coe. “Effect of Strongly Coupled Vibration–Cavity Polaritons on the Bulk Vibrational States within a Wavelength-Scale Cavity”. In: *The Journal of Physical Chemistry B* 123.6 (Feb. 2019), pp. 1302–1306. ISSN: 1520-6106. DOI: 10.1021/acs.jpcb.8b09913. URL: https://doi.org/10.1021/acs.jpcb.8b09913.

[99] T. Chervy et al. “Vibro-Polaritonic IR Emission in the Strong Coupling Regime”. In: *ACS Photonics* 5.1 (Jan. 2018), pp. 217–224. DOI: 10.1021/acsphotonics.7b00677. URL: https://doi.org/10.1021/acsphotonics.7b00677.

[100] M. Seidel et al. “Correction to Vibro-Polaritonic IR Emission in the Strong Coupling Regime”. In: *ACS Photonics* 6.7 (July 2019), pp. 1823–1825. DOI: 10.1021/acsphotonics.8b01756. URL: https://doi.org/10.1021/acsphotonics.8b01756.

[101] J. George et al. “Multiple Rabi Splittings under Ultrastrong Vibrational Coupling”. In: *Phys. Rev. Lett.* 117 (15 Oct. 2016), p. 153601. DOI: 10.1103/PhysRevLett.117.153601. URL: https://link.aps.org/doi/10.1103/PhysRevLett.117.153601.

[102] S. C. Kumar et al. “High-power femtosecond mid-infrared optical parametric oscillator at 7 µm based on CdSiP2”. In: *Opt. Lett.* 40.7 (Apr. 2015), pp. 1398–1401. DOI: 10.1364/OL.40.001398. URL: https://opg.optica.org/ol/abstract.cfm?URI=ol-40-7-1398.

B.2 List of Figures

B.3 List of Tables

B.4 List of Abbreviations

ADC analogue-to-digital conversion 52

APD avalanche photodiode 37, 51, 61

BBO β-barium borate (β-BaB_2O_4) 11, 37

BPD balanced photodiode 36, 38, 44, 46, 51, 57, 58, 63

CEO carrier-envelope phase offset 1, 2, 6, 7, 16, 18, 19, 34, 35, 38, 39

CEP carrier-envelope phase 6, 15, 25

CSP cadmium silicon phosphide ($CdSiP_2$) 84

CW countinuous wave 1, 15, 25, 27, 34, 57, 58, 61, 67, 81

DAQ data acquisition and control system 51, 52, 83

DC direct current 17, 21, 45

DCF double-cladding fiber 36, 37

DFG difference frequency generation 2, 3, 10–12, 14, 18, 19, 26–28, 31–33, 37, 40, 41, 44, 46, 49, 51, 56, 64, 67, 69, 74, 79, 81, 82, 84

DLA demodulating logarithmic amplifier 44, 45

DM dichroic mirror 37, 41, 42, 45, 46

DOOCS Distributed Object Oriented Control System 83

FBG fiber Bragg grating 35, 38

FFT fast Fourier transform 43, 49, 52, 77

FPGA field-programmable gate array 35, 82

FROG frequency resolved optical gating 33, 37, 67

FTIR Fourier transform infrared 5, 20, 29–33, 43, 44, 50–53, 56, 64, 79, 82, 84

FWHM full-width at half-maximum 25, 32, 33, 67, 74

GPS Global Positioning System 18

HNLF highly nonlinear fiber 14, 37, 40–42, 46, 60, 62, 63, 67, 81, 82, III

HWP half-wave plate 37, 41, 42, 62

ILS instrument line shape 30, 50

LIDAR light detection and ranging 1

LPS laser protection system 34, 35

MMPC multi-mode pump combiner 36, 37

NPRO Non-planar ring oscillator 27, 36, 38, 58, 61–63, 65, 66, 72, 78, 81, 82

OPD optical path difference 30, 45–47, 49–51, 54, 56, 57

OPO optical parametric oscillation 2, 3, 82, 84

PBS polarizing beam splitter 41, 60

PID proportional-integral-derivative 17, 27, 38, 45–47

PLL phase-locked loop 17, 18, 24, 37–39, 45, 78

PPLN periodically poled magnesium-oxide doped lithium niobate ($MgO:LiNbO_3$) 42, 46, 56, 60, 62, 64, 84

PSD power spectral density 19–22, 24–26, 39, 74, 76–78

QPM quasi-phase matching 12, 42

QWP quarter-wave plate 35

RAID redundant array of independent disks 52

RBW resolution bandwidth 69, 71, 72, 74

RF radio frequency 1, 7, 15, 17, 21, 24, 32, 39, 58, 59, 66, 69, 71, 72, 74

RIN relative intensity noise 3, 21, 22, 25, 27, 32, 33, 41, 44, 45, 56, 57, 79, 81

RMS root-mean-square 21, 25, 39, 49, 56

SAM saturable absorber mirror 35, 59, 60

SFG sum frequency generation 10, 28

SHG second harmonic generation 9–12, 16, 28, 44, 58, 63, 64, 71, 74, 75, 78

SI International System of Units/Système International 18

SNR signal-to-noise ratio 30–32, 45, 51, 53, 54, 66, 67, 69, 72

SPM self-phase modulation 13, 14, 16

SSA signal source analyzer 24, 25, 39, 58, 74, 75

SSB PSD single-sideband power spectral density 25, 26, 39, 75, 77

SSFS soliton self-frequency shift 3, 13, 14, 18, 40, 41, 44, 56, 58, 60, 81, 82, 84

TODCF third-order dispersion compensation fiber 36, 60, 67

WDM wavelength division multiplexer 35

ZGP zinc germanium phosphide ($ZnGeP_2$) 58, 64

C Acknowledgements

To the reader, I would like to thank you for taking the time to get here. Hopefully this work might be able to help you in your quest to create some beautiful new science, at least I know that the work of everyone before me did help me.

In one way or another so many different people took part in the creation process of this thesis, and to this near-infinite amount of truly great people I am very grateful. First I of course would like to thank both Dr. Ingmar Hartl and Prof. Dr. Jochen Küpper for the opportunity to take part in this amazing project and their supervision over its duration. To Ingmar I would also like to extend my gratitude for allowing me to do my research in his FS-LA group at DESY. In his group I found an amazing workplace with highly knowledgeable and fun colleagues (both former and current) who always were eager and happy to help me in my endeavours. Of those, my gratitude goes to Dr. Yuxuan Ma, Dr. Christoph M. Heyl and Dr. Marcus Seidel who took over some of the supervision duties from Ingmar and with whom I had lots of fruitful discussions and meetings about the current state and future of the project. Additionally, I would like to thank my colleagues Sarper Salman, Dr. Christoph Mahnke, Arthur Schönberg, Yannick Schrödel, Nikolas Rupp, Henrik Schygulla and Dr. Victor Hariton for many lunch and coffee sessions which were often very helpful and fun. I also would like to thank Sarper for our time in the lab together fixing the two frequency combs when they were not cooperating. His input and help with these lasers especially was crucial in bringing this work to an end.

To my office and lab mates Dr. Henrik Tünnermann, Dr. Yi Hua, Dr. Mingqi Fan, Dr. Hongwen Xuan and Prannay Balla I am also thankful for discussions and the help I received from them. I also kindly acknowledge Arthur, Yannick and Dr. Samuel Hartwell, who were very kind for offering to proofread my thesis, providing many helpful comments to improve its quality in addition to the ones from both Marcus and Ingmar. To my 2022 summer student Yanqiu "Kate" Zhao I am very thankful for helping me out with setting up the cavity planned for the hybrid light-matter states for the first time and providing some helpful experience there, in addition to the fun time we had together. I also would like to thank the FS-LA-LAE for their great support with all electronics and software in the laser lab, especially for their help with the laser protection system of the Yb:fiber comb. From the group of Prof. Küpper I would like to thank Dr. Guang Yang for the great work on the ammonia project together and for always offering his help in the lab. To end this section, I would like to thank Deutsches Elektronen-Synchrotron DESY in general for providing me with a great place to work at and the

funding for this work, and the PIER Helmholtz Graduate School for accepting me into their PhD programme with many great opportunities to learn from.

Over the years I met countless people at probably hundreds of concerts in and around Hamburg and music festivals around Germany mainly centered around all the beautiful extremes in Metal and Hardcore music. Many of them became great friends to me or even band mates with whom I was or still am able to create some weird stuff together. Similarly, I met many other great people at the University of Hamburg over the course of my studies and my thesis. Trying to name or even count all of them would be impossible, so some representatives will need to suffice. To Stella, Esther, Tim, Tom, Toby, Isabelle, Lars, John, Stephan, Felix, Christoph, thank you all for the great times.

Getting to the end, I would like to deeply thank Dr. Frederik Bartelmann, Jannis Neuhaus-Steinmetz, Malte Hagemann, Dr. Razvan Krause and Freya Berggötz, who were all helping me greatly with my mental health after some devastating personal blows which were difficult to process. To Freya, I am especially thankful for the time we spent together and for her help with finding professional counselling, and I am truly sorry for how things went south between us.

My last thanks goes out to my family with my parents Kirsten and Andreas Laumer and my brothers Sebastian (with his wife Jayne) and Benedict (with his girlfriend Stefhany) who were always supporting me well in all different manners over the course of my life.

D Eidesstattliche Versicherung

Hiermit versichere ich an Eides statt, die vorliegende Dissertationsschrift selbst verfasst und keine anderen als die angegebenen Hilfsmittel und Quellen benutzt zu haben.

Hamburg, den _____ ,

_____

Dominic Laumer